Atmospheric Delay Modeling for Satellite Laser Altimetry

by

Katherine J. Quinn

Submitted to the Department of Earth, Atmospheric, and Planetary Sciences in partial fulfillment of the requirements for the degree of

Doctor of Philosophy

at the

MASSACHUSETTS INSTITUTE OF TECHNOLOGY

May 2002

Author .....
Department of Earth, Atmospheric, and Planetary Sciences
May 3, 2002

Certified by ... .
Thomas A. Herring
Thesis Supervisor

Accepted by .....
Ronald G. Prinn
Department Head

Abstract

NASA's Ice, Cloud, and Land Elevation Satellite (ICESat) is a laser altimetry mission with the primary purpose of measuring the mass balance of the ice sheets of Greenland and Antarctica. It will provide 5 years of topography measurements of the ice, as well as land and ocean topography. In order to accurate topography measurements the laser altimeter ranges must be corrected for certain biases. Atmospheric delay is one such bias. As the laser pulse travels through the atmosphere it will be refracted, introducing a delay into the travel time. This delay must be estimated to correct the ranges and the delay estimations need to be validated. Of particular concern are errors in the delay estimates that have the same characteristics as the expected mass balance variations. The main focus of this dissertation is to formulate algorithms for calculating the ICESat atmospheric delay and estimate the expected delay values and errors.

Our atmospheric delay algorithm uses numerical weather model data to estimate delay values. We have validated these algorithms using Automatic Weather Stations (AWS) in the polar regions and GPS data over the globe. The GPS data validation was also augmented by in-situ meteorology measurements at some the stations. The GPS validation process additionally allowed us to investigate the estimation of precipitable water vapor using GPS data. The validation studies have shown that our atmospheric delay algorithm errors are well within the ICESat error budget of 20 mm. The overall global delay errors are estimated to be approximately 5.4 mm and the polar delay errors are 12.2 mm. There are no discernible biases in the error and the seasonal variations in error magnitudes are well characterized.

Acknowledgments

First and foremost I'd like to thank my adviser Tom Herring for his guidance and patience. We've both waited a long time for this. I would also like to thank my committee members Reginald Newell, Brad Hager, and Bob Schutz for their thoughtful critiques, and thanks to Maria Zuber for her comments. I'm grateful to Simon McClusky and Bob King for answering all my computer questions over the years.

Thanks to my friends at MIT for discussions academic and otherwise: Bonnie Souter (who gave me my first place to live), Clint Conrad (office mate for five years and still friends), Rebecca Morss, John Olson, the new kids Brendan Meade and Eric Hetland, Liz Hearn, and my current office mate An Nguyen. I'm grateful to other friends I've met along the way who have helped to keep my faith in science going strong: my ICESat mates Helen Fricker and Claudia Carabajal, and my FMARS buddy Steve Braham and the rest of the gang in Crew 2.

Many thanks to my closest friends through the fun times and the not so fun times: Sheri White, Meghan Hanawalt, Ali and Wil Pollock, and especially my best friend Hershey Hirschkop, who was my first friend at MIT and is now a mate for life. For giving me an outlet for my frustrations and good friends to play with, I'd like to thank all the folks on the MIT women's rugby football team, the Boston Women's Rugby Football Team, the Lava flag football team, and the Copacetics softball team. A special thanks goes to Eleanor Roffman for being my thesis doula. I'd particularly like to thank my newest friend and more, Carol Matsuzaki, who met me during the worst part of my thesis struggle and managed to make things feel better.

Finally, I give all thanks and love to my family: to my big sister Joanne for doing for her sisterly duty of loving me even when she was annoyed with me., to my brother-in-law Chris Owens for doing his husbandly duty of loving Jo, to the McLaren and Quinn clans back home in Australia, to my "Uncles" Ben Mittman and Jimmy Ferra, and to my beautiful cat Kimba, who was family to me. I'd especially like to pay tribute to my parents, Kay and Patrick Quinn. They are the foundation of my life and a source of never ending source of support and love. Always there during the tough times to help me through, I would have never finished without them. I dedicate this dissertation to them.

Table of Contents

Chapter 1

Introduction

The ice sheets of Greenland and Antarctica contain enough ice that if they completely melted they would raise sea level by 80 meters. This melting is not imminent, however we know that there are dynamic changes occuring to these ice sheets. Sea level is currently rising at 2 mm/yr [*Nerem et al.*, 1997], the question is how much are ice sheet mass changes contributing to changes in sea level. At this time we do not know whether the mass balance of the polar ice sheets is positive or negative. This is the largest uncertainty in our understanding of sea level rise and our ability to predict future rates of sea level rise [*IPCC*, 1992].

Our present understanding of mass balance is largely based on comparing total snow accumulation with total ice loss, the associated errors are large. Surface elevation changes may also be measured using satellite radar altimeters and aircraft laser altimeters. However, the spatial coverage of these altimeters is limited. The GLAS Science Requirements document [*GLAS Science Team*, 1997] provides an a compilation of mass balance studies. More recent studies include Davis et al [1998], Wingham et al [1998], Krabill et al [2000], and Davis et al [2001]. Taken as a whole, these studies indicate that the interior of Antarctica is stable within approximatey 5 mm/yr, whereas the West Antarctic icestreams show changes on the order of 10 centimeters per year, and up to a couple of meters per year. The interior of Greenland appear to be stable within approximately 1 cm/yr. The margins and southeast portions of Greenland may be thinning at up to 1 m/yr. These estimates are all secular trends. The seasonal and interannual variations in surface elevation are largely driven by snow accumulation patterns in the interiors and melting rates and iceberg calving rates at the margins. Accumulation rates are spatially and temporally highly variable, however they tend to be highest in the winter months. The knowledge of precipitation rates over the polar ice sheets is very poor.

The Ice, Cloud, and Land Elevation Satellite (ICESat) is due to be launched in late 2002. It is designed to have a 3 year lifetime with a 5 year goal. The mission's primary objective is to measure ice sheet topography and the associated temporal changes. The Geoscience Laser Altim-

eter System (GLAS) is a nadir pointed pulsed laser altimeter that will provide the topography measurements by measuring the range from the satellite to the ground. Coupled with knowledge of the satellite orbit position, which is primarily determined by GPS recievers and star trackers on ICESat, the topography height may be determined. The nominal precision of this measurement is designed to be better than 10 cm with a 70 m spot size on the ground. GLAS is a Nd:YAG laser with a 40 Hz pulse rate and approximately 0.1 mrad beam divergence. ICESat's orbit altitude is about 600 km with an inclination of 94°. The operational orbit ground track will have an 183 day repeat pattern with a 25 day sub-repeat cycle. The cross track spacing is 15 km at the equator and the along track spot spacing is 170 m. The satellite will cover up to 86° latitude, there is off-nadir pointing capability that will allow the hole at the poles to be filled in.

The primary GLAS science goal for the cryosphere is to measure the long-term changes in mass balance of the Greenland and Antarctic ice sheets to assess their contribution to global sea-level. This additionally requires that we measure the seasonal and interannual variations in ice sheet topography in order to distinguish the true long-term trends from natural climate variability. Details of the science goals and requirements are given in the GLAS Science Requirements document [*GLAS Science Team*, 1997]. Based on our knowledge of present day ice sheet height variations and in conjuction with the mission parameters, a single shot error budget has been compiled. A summary of the error budget is given in Table 1.1. The atmospheric delay component, which is the focus of this thesis, is budgeted to be less than 2 cm.

Table 1.1: Single Shot Error Budget

Error Source	Contribution
Instrument precision	10 cm
Radial orbit determination	5 cm
Pointing determination	7.5 cm
Atmospheric delay	2 cm
Atmospheric forward scattering	2 cm
Other	< 1 cm
RSS total	**13.8 cm**

Chapter 2 of this dissertation will describe the ICESat atmospheric delay model we have

created. The atmospheric delay estimates are a function of surface pressure and precipitable water vapor. For the ICESat mission we will be using the global numerical weather model analysis from the National Centers for Environmental Prediction (NCEP) to estimate pressure and precipitable water vapor at the laser footprint locations.

Validation of the atmospheric delay estimates will center around validating our surface pressure and precipitable water vapor estimates. Chapter 3 is a surface pressure validation study in Antarctica using Automatic Weather Station (AWS) data. We will discuss Antarctic weather patterns and how they might effect the ICESat measurements, and we perform surface pressure comparisons to estimate the atmospheric delay error in Antarctica. Chapter 4 is a precipitable water vapor validation study. We will be using GPS estimated tropospheric delay values combined with our estimated surface pressure values to obtain precipitable water vapor estimates. These estimates may then be compared to the NCEP value that will be used in the operational ICESat data processing. This method of using GPS data to estimate precipitable water vapor is commonly known as GPS meteorology. For numerical weather models water vapor is one of the most difficult variables to estimate, due to its highly variable and unmixed distribution. GPS meteorology is a valuable method for increasing our knowledge of water vapor in the atmosphere. In Chapter 4 we also look at whether using NCEP derived surface pressure can provide accurate measures of water vapor, as opposed to using an in-situ pressure sensor.

References

IPCC, Climate Change 1992: The Supplementary Report to the Intergovernmental Panel on Climate Change Scientific Assessment, Houghton, J.T., B.A. Callander, and S.K. Varney (eds.), *Cambridge University Press, Cambridge,* 1992.

Davis, C. H., C.A. Kluever, and B.J. Haines, Elevation change of the southern Greenland Ice Sheet, *Science, 279,* 2086-2088, 1998.

Wingham, D., A.J. Ridout, R. Scharroo, R.J. Arthern, and C.K. Shum, Antarctic elevation change from 1992 to 1996, *Science, 282,* 456-458, 1998.

Krabill, W., W. Abdalati, E. Frederick, S. Manizade, C. Martin, J. Sonntag, R. Swift, R. Thomas, W. Wright, and J. Yungel, Greenland Ice Sheet: high-elevation balance and peripheral thinning, *Science, 289,* 428-430, 2000.

Davis, C. H., R. G. Belu, and G. Feng, Elevation change measurement of the East Antarctic Ice Sheet, 1978 to 1988, from Satellite Radar Altimeter, *IEEE Trans. Geo. & Rem. Sen., 39(3),* 635-644, 2001.

Chapter 2

Estimating ICESat Laser Altimeter Atmospheric Delays

2.1 Introduction

This chapter will establish the fundamental atmospheric delay algorithms and how we apply these algorithms to estimate the ICESat atmospheric delay. The atmospheric delay depends on the integral of the refractive index along the path that the laser pulse travels through the atmosphere. The refractive index of air at optical wavelengths is a function of density and molecular composition. For ray paths near zenith and closed form equations for the refractivity, the atmospheric delay can be shown to be directly related to surface pressure and total column precipitable water vapor. For ray paths off zenith a mapping function relates the delay to the zenith delay. The closed form equations for refractivity recommended by the International Union of Geodesy and Geophysics (IUGG) are optimized for ground based geodesy techniques and in the next section we will consider whether these equations are suitable for satellite laser altimetry.

To estimate surface pressure and precipitable water vapor, numerical weather models are appealing because they are internally consistent and provide spatially uniform coverage. Values for surface pressure and precipitable water vapor will be calculated from global atmospheric analyses. The National Center for Environmental Prediction (NCEP) global numerical weather analyses will be used. As of January 2000, these analyses have been produced on a 1 by 1 degree grid every 6 hours. Fields included are temperature, geopotential height, and relative humidity at standard upper atmospheric pressure levels. These atmospheric fields will be interpolated to the location and time tag of the laser footprints. The NCEP provides a surface pressure field, this field is commonly used for calculating atmospheric delay for radar altimetry missions. However, errors in this field make it unsuitable for the level of accuracy we desire, especially over rapidly changing topography. Surface pressure will be calculated by integrating the upper atmospheric field down to the surface height as given by the initial laser footprint location. Appendix A describes this procedure in detail.

There is one contribution to the atmospheric delay that will not be explored in this thesis, which is the delay due to thin cloud and aerosol forward scattering. Photons that are scattered through an angle small enough such that they are still within the reciever field of view will have travelled an extra distance, thus adding to the total delay. The gaussian ICESat laser pulse will be stretched, leading to an offset from the true range. The forward scattering issue was first addressed by the GLAS atmospheric data products team [*Palm et al,* 1999] and has been expanded upon in later studies [*Duda et al*, 2001; *Marhesh et al*, 2001]. The forward scattering delay depends on cloud height, cloud optical depth, particle size, particle shape, and reciever field of view. Low level clouds produce the greatest delay. If the return laser pulse is modelled using multiple gaussion peaks, the forward scattering error may be on the order of 10 cm, in the worst case. Further work must be done on the forward scattering issue. It is hoped that the atmospheric channel on the GLAS instrument may be used to mitigate this error, or at least flag the returns where the error is large. Other satellite data, such as MODIS (Moderate Resolution Imaging Spectrometer), may also be able to provide the require cloud data [King et al, 1992].

The GLAS single shot error budget assumes less than 20 mm rms error in the atmospheric delay [*GLAS Science Team*, 1997]. All the steps in the atmospheric delay algorithm require an estimate of the associated error. Unfortunately, NCEP does not provide formal error estimates for its numerical weather models. The atmospheric delay algorithm will be validated using Automatic Weather Station data in polar regions, in-situ meteorological data at GPS stations (where available), and the estimated delay values from global GPS data. The validation studies performed so far predict less than 12 mm rms error in delay.

Note that all units in this chapter are SI unless otherwise stated.

2.2 Modeling Atmospheric Delay

2.2.1 Group Refractivity Models

Pulsed satellite laser altimeter systems use the round trip pulse travel time to estimate the distance to the Earth's surface. Atmospheric refraction increases the propagation time and this delay may be corrected for by integrating the refractive index along the ray path through the atmosphere. The one-way correction to the GLAS range measurement, ΔL, due the refractive effects of the Earth's atmosphere is given by

$$\Delta L = \int_{S_{ATM}} n(s)ds - \int_{S_{VAC}} ds \tag{2.1}$$

where $n(s)$ is the group refractive index of the atmosphere along the ray path, S_{ATM} is the curved path followed by the laser pulse from the space craft to the ground, and S_{VAC} is the straight line path from the space craft to the ground. Evaluation of the second integral only requires the space craft and laser footprint coordinates. Evaluation of the first integral also requires knowledge of the refractive index along the curved ray path and is most accurately calculated using ray tracing or numerical integration methods. However, this is not practical for large amounts of data. Models that relate the total delay to the zenith delay by a mapping function are commonly used such that [*Davis, et al.,* 1985]

$$\Delta L = m(\varepsilon, \boldsymbol{P}) \int_{Z}^{\infty} (n(z) - 1)dz \tag{2.2}$$

where $m(\varepsilon, \boldsymbol{P})$ is a mapping function that depends on elevation angle (ε) and a parameter vector ($\boldsymbol{P}$). The integral is evaluated along a zenith path from the ground height Z to the space craft to give the zenith delay. The mapping function will be investigated in a following section.

The argument of the integral $(n - 1)$ is the refractivity and is normally given in parts-per-million i.e., $(n - 1) = 10^{-6}N$. Refractivity varies in the atmosphere primarily as a function of pressure, temperature, and composition. Precision geodetic surveying requires an accurate knowledge of the group refractive index of air. The first comprehensive set of equations was given by Eldén (1953), and until recently these equations were the standard recommended by the International Union of Geodesy and Geophysics (IUGG) for optical wavelengths until [*IUGG,* 1963]. Other formulations have been used as new empirical measurements of refractivity have demonstrated errors in the original Eldén equations [*Eldén,* 1966; *Owens,* 1967; *Peck and Reeder,* 1972; *Birch and Downs,* 1994]. A working group of the IUGG updated their recommendations for the refractive index of air at optical frequencies [*IUGG,* 1999], with two solutions recommended. One is a simple closed formula with an accuracy of no better than one part per million. The other is a more complicated algorithm, used when better that one part per million accuracy is required.

The more accurate algorithm is documented in Ciddor [1996] and Ciddor and Hill [1999]. The Ciddor formulas incorporate the latest moist air refractivity data. They match the measure-

ments within experimental accuracy and are expected to be accurate over a wide range of atmospheric parameters to a few parts in 10^8. The density equations used are valid over ranges of at least -40 to 100 °C, 800 to 1200 hPa, and 0 to 100% relative humidity. However, the algorithm requires a number of steps and as such is unsuitable for practical integration through the atmosphere. It may be used as baseline measurement to compare closed form approximations of refractivity.

The simple closed formula recommended by IUGG is the same as the formula recommended in 1963, amended for an increased CO_2 value of 375 ppm from 300 ppm. This value of carbon dioxide is expected to be valid in 2004 based on estimations of rate of increase and is recommended as the standard value to be used in all formulas. The formula for refractivity is

$$\begin{aligned} N &= N_S \frac{273.15}{1013.25}\left(\frac{P}{T}\right) - 11.27\left(\frac{P_w}{T}\right) \\ N_S &= 287.6155 + \frac{4.88660}{\lambda^2} + \frac{0.06800}{\lambda^4} \end{aligned} \tag{2.3a}$$

where N is group refractivity, T is temperature (K), P is total pressure (hPa), P_w is water vapor partial pressure (hPa), N_S is standard air refractivity with 375 ppm CO_2, T = 273.15 K, P = 1013.25 hPa, P_w = 0 hPa, λ is wavelength (μm). For the GLAS wavelength of 1.064 μm, and converting pressure units to Pa from hPa, Equation 2.3a becomes

$$N = (0.7871275\ \text{K/Pa})\frac{P}{T} - (0.1127\ \text{K/Pa})\frac{P_w}{T} \tag{2.3b}$$

The IUGG closed formula was discussed by Rüeger [1996], where he noted that the humidity term is not very accurate and may have other systematic errors. Rüeger strongly recommended that the equations in Owens [1967] be used for higher precision measurements. For optical frequencies, the group refractivity is given by

$$N = k_1(\lambda)\frac{P_d}{T}Z_d^{-1} + k_2(\lambda)\frac{P_w}{T}Z_w^{-1}$$

$$\begin{aligned} k_1(\lambda) &= 164.63860\frac{(238.0185 + \lambda^{-2})}{(238.0185 - \lambda^{-2})^2} + 4.77299\frac{(57.362 + \lambda^{-2})}{(57.362 - \lambda^{-2})^2} \\ k_2(\lambda) &= 0.648731 + 0.0174174\lambda^{-2} + 3.55750\times10^{-4}\lambda^{-4} + 6.1957\times10^{-5}\lambda^{-6} \end{aligned} \tag{2.4a}$$

where $k_1(\lambda)$ and $k_2(\lambda)$ are experimentally determined functions of the laser wavelength (K/Pa), λ is

wavelength (μm), P_d and P_w are the partial pressures of dry-air and water vapor (Pa), T is temperature (K), and Z_d and Z_w are the compressibilities of dry-air and water vapor. The Owens equations are based on 300 ppm CO_2. By modifying equation (2) from Ciddor [1996], a correction factor for dry air refractivity based on carbon dioxide concentration may be calculated such that

$$F_C = \frac{N_2}{N_1} = 1 + \frac{(c_2 - c_1)}{(c_1 + 1.8722\times10^6)} \tag{2.5}$$

where c_1 and c_2 are carbon dioxide concentrations in ppm for the respective dry air refractivity values. For our application, c_1 is 300 ppm and c_2 is 375 ppm, giving a correction factor of $F_C = 1.000040053$. Note that this is only applied to the first term in Equation 2.4a. For the GLAS wavelength of 1.064 μm, $k_1 = 0.7866070$ K/Pa and $k_2 = 0.6644364$ K/Pa. By also applying the correction for carbon dioxide concentration, Equation 2.4a becomes

$$N = (0.7866385 \text{ K/Pa})\frac{P_d}{T}Z_d^{-1} + (0.6644364 \text{ K/Pa})\frac{P_w}{T}Z_w^{-1} \tag{2.4b}$$

To approximately compare equation 2.3b to equation 2.4b, we will ignore the compressibility factors. Equation 2.4b then needs to be re-written in terms of $P_d = P - P_w$, and becomes approximately $N = (0.7866385 \text{ K/Pa})P/T - (0.1222021 \text{ K/Pa})P_w/T$. It can be seen that the two equations are very similar. Percentage wise, the constant preceeding the water vapor term differs the most. However, the water vapor partial pressure is generally much smaller than the total pressure. The following describes a more quantitative comparison of the two refractivity equations over a range of atmospheric conditions.

The IUGG precision algorithm (Ciddor99) was used as a baseline to compare the IUGG closed formula (IUGG99) to the modified Owens formula (Owens375). All comparisons were carried out at a wavelength of 1.064 μm, which is appropriate for the GLAS laser altimeter. Setting pressure to 1000 hPa, refractivity was compared over a wide range of temperature and relative humidity, the results are shown in Figure 2.1. The IUGG99 model performed best for temperatures above 0 °C and high humidities. This is not unexpected since the driving application for the IUGG recommendations is ground based laser geodetic surveying. The modified Owens model performed consistently better for lower temperatures, suggesting that Owens375 is the better model for integration through the atmosphere as the temperature drops through the troposphere.

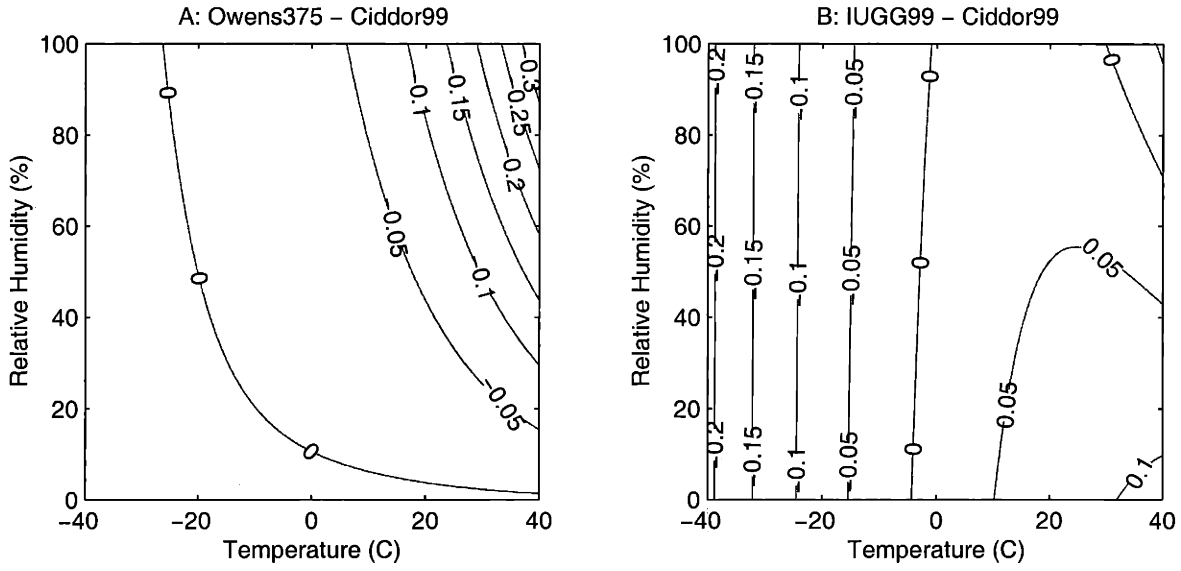

Figure 2.1. Comparison between closed form models of refractivity and Ciddor99 model, for a constant pressure of 1000 hPa, λ = 1.064 μm.

An assessment of the performance of the two closed form models for satellite laser altimetry requires integration of the differences through the atmosphere. As a point of comparison, we used standard atmospheric profiles for temperature and pressure [*NOAA,* 1976] and varied the relative humidity. The profiles of refractivity were numerically integrated as per Equation 2.2, setting the mapping function to one to give zenith delays.

Most of the water vapor in the atmosphere resides in the lower troposphere. Approximately half of the total water vapor is found below 1.5 km altitude. Less that 1 % is found above 11 km, i.e. the stratosphere and above [*Kley et al,* 2000]. There is very little water vapor transfer between the troposphere and the stratosphere, most stratospheric water vapor comes from methane oxidation. Relative humidity values in the stratosphere and above are so low that we shall assume they are zero for our comparison.

Figure 2.2 shows profiles for three different values of tropospheric relative humidity. For zero percent relative humidity the modified Owens model is clearly preferable. However, it becomes less obvious which model is better for higher relative humidities. The integrated difference has been calculated over the whole range of relative humidities, Figure 2.3 compares the absolute value of these delay differences. The Owen375 delay error is less than 0.2 mm, whereas

the IUGG99 delay error is greater than 0.5 mm. The modified Owens model is clearly the better model for this comparison. While the true atmospheric profile will vary from the standard atmosphere and relative humidity is almost certainly not constant along the profile, for satellite altimetry applications the preferred model appears to be Owens375 and thus will be used for the ICESat mission. Based on the comparison in Figure 2.3, inaccuracies in the refractivity model are expected to contribute less than 0.2 mm to the total atmospheric delay error. It should be noted here that satellite laser ranging (SLR) stations commonly use a refractivity model that is the same form as IUGG99, combined with specialized mapping functions [*Marini and Murray,* 1973]. This is the International Earth Rotation Service standard model. We suggest that the standards should be updated to account for the fact that the current models are best suited for ground based observations.

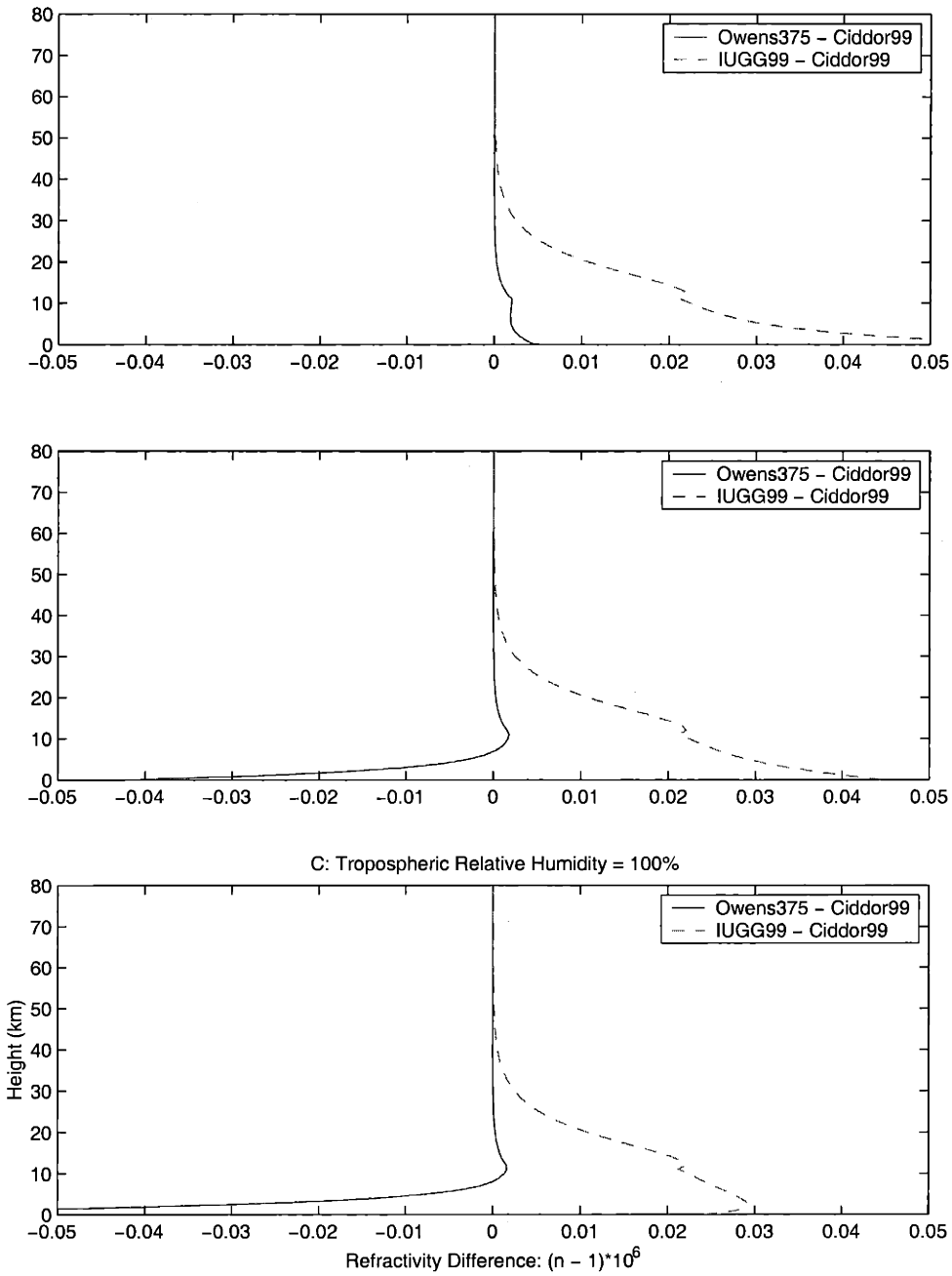

Figure 2.2. Comparison between closed form models of refractivity and Ciddor99 model, for standard atmosphere profiles of temperature and pressure and varying tropospheric relative humidity, $\lambda = 1.064$ μm.

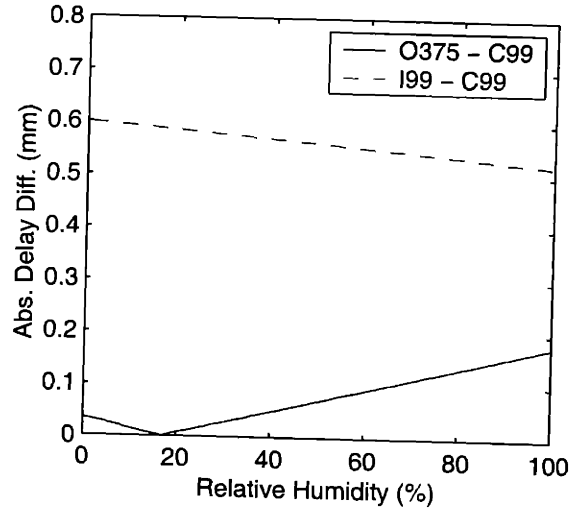

Figure 2.3. Absolute integrated delay differences between closed form refractivity models and Ciddor99 model, for standard atmosphere profiles of temperature and pressure, $\lambda = 1.064$ μm.

2.2.2 Zenith Delay Equations

The modified Owens refractivity equations use compressibilities to account for non-ideal gas behavior such that

$$\rho_i = \frac{P_i M_i}{T R} Z_i^{-1} \tag{2.6}$$

where ρ_i is the density of gas i (dry air or water vapor in the case of the atmosphere) with molecular weight M_i and compressibility Z_i, at pressure P_i and temperature T; and R is the Universal gas constant. For reasons that will become clear shortly, Equation 2.4 is often combined with Equation 2.6 and written such that the total density of gas $\rho = \rho_d + \rho_w$. In this form Equation 2.4 becomes

$$N = F_c k_1 \frac{R}{M_d} \rho + \left(k_2 - F_c k_1 \frac{M_w}{M_d} \right) \frac{R}{M_w} \rho_w \tag{2.7}$$

where the dependence of k_1 and k_2 on wavelength has been eliminated for simplicity, and the dry air refractivity correction factor for carbon dioxide is F_c as given in Equation 2.5. With the assumption that the atmosphere is in hydrostatic equilibrium, the integral in Equation 2.2 for the range correction can be solved exactly. The assumption of hydrostatic equilibrium is violated only under extreme weather conditions, such as thunderstorms and heavy turbulence, where there are significant vertical accelerations [*Fleagle and Businger,* 1980]. These accelerations can reach

1% of gravity, corresponding to a delay error of approximately 20 mm [*Davis et al.,* 1985], however these extreme conditions are rare and the GLAS laser altimeter will not range through thunderstorms.

We use the hydrostatic equation

$$\frac{dP}{dz} = -\rho(z)g(z) \tag{2.8}$$

where z is height through the atmospheric column and $g(z)$ is the gravitational acceleration. Substituting Equation 2.8 into the first term of Equation 2.7 and then substituting into Equation 2.2 yields the "hydrostatic" component of the zenith range correction, ΔL_H, which can be written as

$$\Delta L_H = 10^{-6} F_c k_1 \frac{R}{M_d} g_m^{-1} \int_Z^\infty \frac{dP}{dz} dz \tag{2.9}$$

where g_m is the mean value of gravity in the column of the atmosphere. Since gravity decreases slowly with height and can be closely approximated as a simple function of latitude, this value can be expressed accurately in terms of the height, Z, and latitude, ϕ, of the ground point to which the altimeter measurement is made [*Saastamoinen,* 1972]

$$g_m = 9.8062(1 - 0.00265\cos(2\phi) - 3.1\times10^{-7}(0.9Z + 7300)) \text{ ms}^{-2} \tag{2.10}$$

Equation 2.9 can be further reduced because the integral is simply the surface pressure at height Z, and therefore the largest part of the atmospheric range correction in the zenith direction is given by

$$\Delta L_H = 10^{-6} F_c k_1 \frac{R}{M_d} g_m^{-1} P_S \tag{2.11}$$

where P_s is the surface pressure.

The remaining part of the zenith atmospheric range correction is due to the residual part of the water vapor not included in the hydrostatic term, commonly called the "wet" component, ΔL_W. Substituting the second term of Equation 2.7 into Equation 2.2 gives

$$\Delta L_W = 10^{-6} k_2' \frac{R}{M_w} \int_Z^\infty \rho_w dz \tag{2.12}$$

where $k_2' = k_2 - F_c k_1 \frac{M_w}{M_d}$. The integral is simply the total column precipitable water vapor, *PW*, an atmospheric variable often reported in atmospheric models. The zenith wet delay can now be written as

$$\Delta L_W = 10^{-6} k_2' \frac{R}{M_w} PW \tag{2.13}$$

The empirical functions in the refractivity equation given in Owens [1967] must be evaluated for the GLAS laser altimeter operational wavelength of 1.064 μm. The resulting values are $k_1 = 0.7866070\text{K/Pa}$ and $k_2 = 0.6644364\text{K/Pa}$. Dry air with a carbon dioxide concentration of 375 ppm has a molecular weight of $M_d = 28.9632$ kg.kmol^{-1} [*Ciddor,* 1996], and water has a molecular weight of $M_w = 18.0152$ kg.kmol^{-1}. Using these values and the previously calculated value for the carbon dioxide correction factor of 1.000040053, $k_2' = 0.1751448\text{K/Pa}$. Substituting these values and the Universal gas constant value of $R = 8314.510$ J.kmol^{-1}.K^{-1} into Equations 2.11 and 2.13 gives the final zenith delay equations

$$\Delta L_Z = \Delta L_H + \Delta L_W \tag{2.14}$$

$$\Delta L_H = (2.2582\text{m}^2\text{s}^2/\text{Pa}) g_m^{-1} P_S \tag{2.15}$$

$$\Delta L_W = (8.0834\times10^{-5}\text{m/mm}) PW \tag{2.16}$$

For a typical surface pressure value of 1000 hPa and an approximate value of 9.8 ms^{-2} for the mean gravity, the zenith hydrostatic delay is approximately 2.3 m. This is the major component of total delay. Zenith wet delay is much more variable. With typical precipitable water vapor values of less than 10 mm in the polar regions to 50 mm in the tropics, it varies from 1 to 4 mm.

2.2.3 Off-Nadir Pointing Corrections

The mapping function relates the total atmospheric delay at an arbitrary elevation angle to the zenith delay such that

$$\Delta L = m(\varepsilon, \boldsymbol{P}) \Delta L_Z \tag{2.17}$$

where ε is the elevation angle and **P** is a vector that commonly consists of various climatological parameters. The mapping function assumes azimuthal symmetry of the atmosphere about the ground point. This is a very good assumption for the near-nadir pointing ICESat mission,

although horizontal gradients are a significant error source for low elevation angle satellite laser ranging.

When it is assumed that the refractivity of the troposphere is azimuthally and spherically symmetric, Marini [1972] showed that the continued fraction form of the mapping function is

$$m(\varepsilon) = \cfrac{1}{\sin\varepsilon + \cfrac{a}{\sin\varepsilon + \cfrac{b}{\sin\varepsilon + \cfrac{c}{\sin\varepsilon + \ldots}}}} \tag{2.18}$$

where a, b, c, etc., are parameters that may be approximated using climatic data. The very simplest form of this equation is

$$m(\varepsilon) = \frac{1}{\sin\varepsilon} \tag{2.19}$$

which works best at elevation angles near zenith since that parameters a, b, c, etc., are all significantly less than one. A number of different forms of the mapping function have been published. To test the accuracy of Equation 2.19 we have compared it to two different but widely used mapping functions. One is by Davis, et al. [1985], named CfA-2.2, which depends on surface pressure and surface temperature. The other is by Niell [1996], which depends on latitude and day of year. The different climatic variables used result from the different climatologies and functional forms of the parameters used. We compared the simple mapping function to the test functions by subtracting the test function from the simple mapping function and multiplying by 2.3 m, which is an approximate estimate for zenith delay. This gives estimates of how much the total delay will change by. Figures 2.4 and 2.5 show these comparisons over a range of climatological conditions.

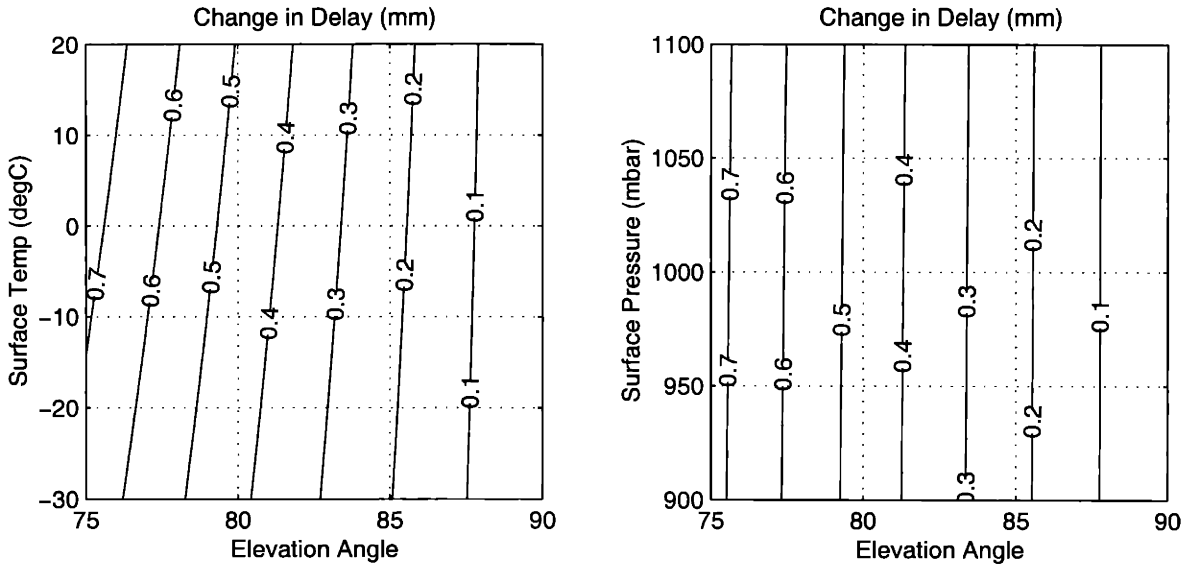

Figure 2.4. Change in delay of the simple mapping function compared to CfA-2.2 mapping function. Left plot is for P_0 = 1000 mbar, right plot is for T_0 = 0°C.

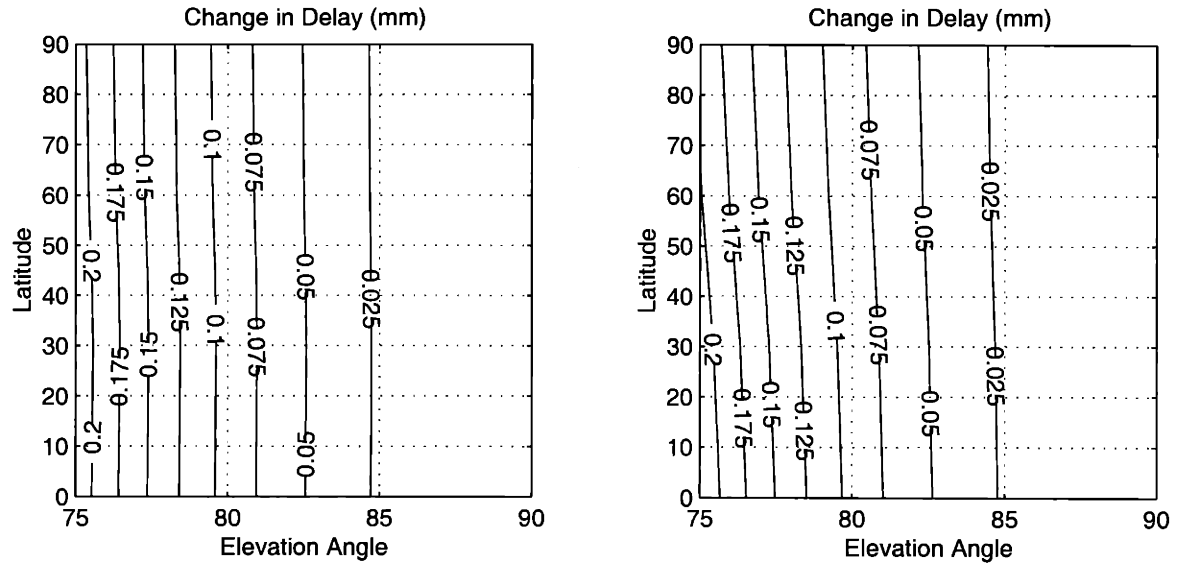

Figure 2.5. Change in delay of the simple function compared to Niell mapping function. Left plot is for maximum day of year phase, right plot is for minimum day of year phase.

For both comparisons, the simple form of the mapping function approximates the other forms very closely. We don't expect that the GLAS space craft will point beyond 10° off nadir. The differences in this region are less than 0.5 mm for CfA-2.2 and 0.1 mm for Niell. It should be noted that these other mapping functions are optimized for low elevation angles. In fact, we expect the Niell mapping function to work better at higher elevation angles due to its functional

form. Given the small delay error associated with using the simple mapping function we will use this mapping function for the GLAS mission. The error associated with the mapping function is expected to be less than 0.5 mm for pointing angles of less than 10°. The error decreases to zero for nadir pointing.

Another concern for off-nadir pointing of the space craft is the change in expected footprint location due to bending of the ray in the atmosphere. This effect will not significantly change the atmospheric delay calculation but should be considered for spacecraft pointing calibrations where the location of the laser footprint is directly measured at the ground.

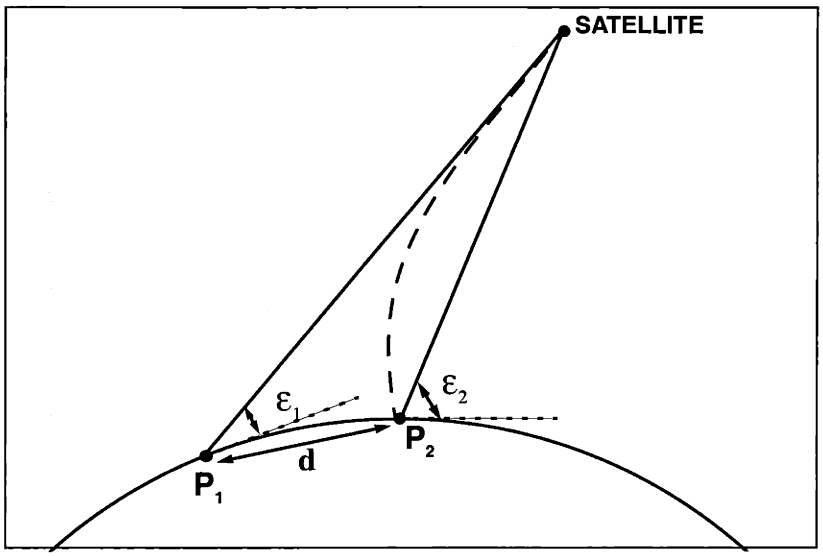

Figure 2.6. Geometry of laser ray path.

The real curved path is shown by the dashed line in Figure 2.6. $\mathbf{P}_1$ is the expected ground location of the laser footprint for the satellite position and pointing angle, $\alpha_1 = 90^o - \varepsilon_1$, as measured at the satellite. $\mathbf{P}_2$ is the real ground location of the laser footprint after following the refracted path through the atmosphere, which is shifted by a distance d towards the sub-satellite point. If the satellite position and real footprint location were used to calculate the apparent satellite pointing angle, $\alpha_2 = 90^o - \varepsilon_2$, this would result in an error such that $\alpha_1 = \alpha_2 - \delta\alpha$. The correction can be approximated by a simple expression for pointing angles of less than 75° [*Astronomical Almanac,* 1999] such that

$$\delta\alpha = 0.00452^\circ P \tan\alpha_2 / (273 + T) \qquad (2.20)$$

where T is the temperature (°C) and P is the pressure (hPa) at the surface. Using standard surface values of 15°C and 1013 hPa, this gives an approximate value of

$$\begin{aligned} \delta\alpha &= 0.016^\circ \tan\alpha_2 \\ &= 57'' \tan\alpha_2 \end{aligned} \tag{2.21}$$

At an altitude of 600 km and pointing angle of 10 degrees, the pointing error will be approximately 10 arcseconds and the distance the laser footprint is shifted by will be 30 m.

As an aside, this correction equation may also be used to estimate whether horizontal gradients in the pressure fields will substantially affect the path of the laser pulse. A typical upper value of the synoptic pressure gradient is 10 mbar per 100 km. Near the surface the derivative of pressure with respect to height is approximately 0.1 hPa/m. This means that a typical slope to the pressure field is 2 arcseconds. Assuming that this gradient is constant through the atmosphere (actually, it should decrease exponentially) we can insert this angle into Equation 2.21 to determine how much the path will deviate. For a 2 arcsecond slope the deviation is 6×10^{-4} arcseconds, which is negligible.

2.2.4 NCEP Global Analyses

The zenith delay formulas given in a previous section are directly dependent on surface pressure and total precipitable water vapor. We require a data set that will allow us to calculate values for surface pressure and total precipitable water vapor at the laser footprint locations. Numerical weather models are appealing because they are internally consistent and provide spatially uniform coverage. We will use the global analyses and forecasts produced by the National Oceanic and Atmospheric Administration (NOAA) National Center for Environmental Prediction (NCEP), the data products are from the Global Data Assimilation System (GDAS) [*Kanamitsu,* 1989; *Kanamitsu et. al.,* 1991].

The NCEP GDAS uses a spectral model based on the primitive atmospheric equations. Observational data is assimilated using a spectral statistical-interpolation (SSI) analysis [*Parrish and Derber,* 1992]. Data sources used to create the NCEP global analyses include ground stations, radiosondes, satellites, and buoys. They are produced on a 1 degree uniform latitude and longitude grid every 6 hours, starting at 0 GMT. These analyses and forecasts consist of a number of meteorological fields for a standard set of levels from the surface to the stratosphere. The fields

that we use for our surface pressure model are temperature, geopotential height, and relative humidity for the tropospheric pressure levels between 1000 mbar and 300 mbar. The total precipitable water vapor is given as a single field integrated through the entire atmospheric column and may also be calculated by integrating relative humidity through the tropospheric levels.

The NCEP analyses report a surface pressure field, however this is not suitable for our purposes. The topography field it is produced on has large errors, and the spectral interpolation used creates spurious waves in the field near areas of rapid change in elevation, as would be encountered at the edges of ice sheets. It is essential to perform this integration rather than use the NCEP surface pressure field so that the correct height of the laser footprint is used. We have compared the NCEP surface pressure field with ground station data in Antarctica and found it to be biased by as much as 40 mbar. An atmospheric model of pressure with respect to height is required to reduce the upper level NCEP fields to a surface pressure value. A hydrostatic equilibrium model of the atmosphere is integrated from an upper atmospheric level to the estimated height of the laser footprint in order to calculate surface pressure. This process is described in greater detail in Appendix A. The NCEP global analyses give total column precipitable water vapor as a single field evaluated at the surface. We will use this field without modification as input into the zenith wet delay equation. For optical wavelengths, the difference between using the NCEP direct precipitable water vapor versus the integrated value is less than 0.1 mm of delay for 95% of the orbit. The least difference occurs where water vapor values are small, as in the polar regions. The precipitable water vapor contribution to total delay is small but highly variable, both spatially and temporally, and should be monitored throughout the ICESat mission.

The NCEP global analyses can be downloaded near real time from an anonymous NOAA ftp site (ftpprd.ncep.noaa.gov). It should be noted that this ftp site is not an archive and the products only remain available for approximately 24 hours. Throughout the mission the ICESat team will download and archive the NCEP fields that are required to calculate atmospheric delay.

There are two different runs of the GDAS we can use: (a) the final run (FNL); and (b) the aviation run (AVN). The final run produces the best analysis, as it is delayed to allow for late arriving data. The analysis and a 6 hour forecast are posted to the ftp site approximately 6 to 10 hours after the analysis time. The 00Z and 12Z analyses take longer than the 06Z and 18Z analyses because there are more ground station data taken on 12 hour intervals. The aviation run uses exactly the same model as the final analysis except that it is run at an earlier time and therefore

has less data included. The AVN analysis is posted to the ftp site approximately 3.5 hours after the analysis time. The forecasts are provided every 6 hours out to 84 hours and take an additional 5 minutes to be posted for each forecast. All forecasts are posted to the ftp site approximately 5.5 hours after the analysis time. Table 2.1 is a summary of approximate NCEP delivery times.

Over 95% of the time the final analysis is available for use. However, sometimes this run is not performed by NCEP due to time constraints. Our next best choice is the aviation analysis, which is almost always available. If the analyses are not available we can use the forecasts, with the order of preference being the FNL 6 hour forecast, and then the AVN forecasts in ascending time. The atmospheric delay estimates should be flagged according to the data used, in order to assess the quality of the estimate. The forecasts need to be archived until it is certain we can obtain the better analyses.

Table 2.1: NCEP Delivery Times as of March 29, 2000

Model	0000Z	0600Z	1200Z	1800Z
FNL				
analysis	0730Z	1030Z	2130Z	2300Z
6 hr forecast	0735Z	1035Z	2135Z	2305Z
AVN				
analysis	0315Z	0920Z	1515Z	2115Z
6 hr forecast	0325Z	0930Z	1525Z	2125Z
84 hr forecast	0405Z	1010Z	1605Z	2205Z

The NCEP products are stored in GRIB format (GRIdded Binary). This format is widely used in the meteorological community and is the World Meteorological Organization standard for exchanging gridded binary data. It is described by NCEP Office Note 388 [*Stackpole,* 1994]. NCEP has codes for reading GRIB format that we have incorporated into our atmospheric delay software package.

Unfortunately, there are no formal error estimates provided for the atmospheric fields produced by the NCEP GDAS. Studies have compared analyses produced by different forecasting centers, most notably the European Center for Medium-Range Weather Forecasting (ECMWF). However, these competing analyses use similar sets of input data and physical models, and as

such do not provide a quantitative error estimate [*Trenbreth & Olsen*, 1988; *Boer et al.*, 1992]. Validation studies have been performed for the surface pressure and precipitable water vapor estimates to address this shortfall, and these are described in following chapters.

2.2.5 Delay Correction with Respect to Height

The previous sections have demonstrated that calculating surface pressure, and therefore delay, requires a knowledge of the height of the laser footprint location. The atmospheric delay correction will be estimated early in the GLAS processing and there may be later adjustments to the spacecraft orbit and footprint location height. A simple correction function is required that is accurate for height changes in the range of ±100 m.

Given that pressure varies approximately exponentially with height, we expect the correction to be of the form

$$P' = Pe^{(-A(H' - H))} \tag{2.22}$$

where P' and H' are the corrected pressure and geopotential height, P and H are the original pressure and geopotential height, and A is the correction parameter.

Neglecting water vapor, the hydrostatic equation becomes

$$\frac{dP}{dH} = \frac{-g_0 Z_d^{-1} P M_d}{RT} \tag{2.23}$$

where g_0 = 9.80665 m^2/s^2.m' [NOAA, 1976]. Assuming that temperature and inverse compressibility are a constant with respect to height allows us to solve Equation 2.23 for the correction factor such that

$$A = \frac{g_0 Z_d^{-1} M_d}{RT} \tag{2.24}$$

where P, T, and Z_d^{-1} are calculated at the original height. If we substitute a typical surface temperature value of 273.15 K into Equation 2.24, and neglect the compressibility factor, $A = 1.25 \times 10^{-4}$ m^{-1}. This correction factor is defined for geopotential meters, and may be converted to geometric meters using mean sea level gravity instead of g_0. Since atmospheric delay is directly proportional to surface pressure, again neglecting water vapor, this same correction factor may be applied such that

$$\Delta L' = \Delta L e^{(-A(H' - H))} \tag{2.25}$$

2.2.6 Spatial Interpolation

We require a spatial interpolation method that will solve the problem of constructing a smooth function over the entire globe. There are a number of valid interpolation methods we could use, and choosing one is largely driven by the properties of the data set to be interpolated. Given the NCEP global analyses data set structure, i.e. the number of data points, the distribution over the globe and the range of values, we can examine various interpolation methods and their properties to see which one might be most suitable.

When we first began to study this issue in 1996, the NCEP global analyses were being produced on a 2.5 by 2.5 degree grid, a total of 10,512 points with pole repeats. The points are uniform in latitude and longitude but spatially the density changes dramatically over the sphere. Near the poles the points are clustered on circles of latitude much like track data. Fortunately, the upper atmospheric fields we must interpolate are quite smooth compared to surface fields, which will greatly reduce the interpolation errors. Interpolation techniques solve the basic problem of constructing a smooth function defined on a domain when from set of discrete values, possibly located at non-uniform points in the domain. In our interpolation the domain is the surface of a sphere and the discrete values are the NCEP gridded fields.

The problem of bivariate interpolation on a plane of arbitrarily distributed points has been extensively studied. Many of these methods were reviewed and compared by Franke [1982]. If the points on the sphere were only sampled in a small region they could be mapped onto a plane and one of these planar methods could be used on the transformed data. However, our data is distributed over the entire sphere and there is no differentiable mapping function that will map the entire sphere onto a bounded planar region.

Interpolation over a sphere has been addressed by comparatively few authors. Spline and a thin plate spline methods have been presented by Wahba [1981, 1984], but these methods are only efficient up to several hundred data points. Nielson and Ramaraj [1987] and Pottmann [1992] described minimum norm network methods. Lawson [1984] described a spherical triangulation method as did Renka [1984], however Renka's algorithm proved to be more efficient and accurate. Foley [1990] and Pottmann and Eck [1990] presented different modified multiquadric methods. A map and blend method presented by Foley [1992] takes two different mappings of the sphere onto a planar domain and forms a smooth spherical interpolation by blending the two planar interpolations. Any planar interpolation method could be used. Foley used a planar multi-

quadric method as this method performed exceptionally well in tests by Franke [1982] and is simple to implement compared to other methods.

Franke's review [1982] indicated that the multiquadric method (MQ) and related reciprocal multiquadric method (RMQ) were both superior for a range of different test surfaces and data point densities. Included in the review were the planar forms of the thin plate spline and triangulation methods. Franke also noted that the multiquadric method always produced visually smooth surfaces. This is not surprising considering that the multiquadric method has C^{∞} continuity, i.e. all orders of partial derivatives are continuous. The modified MQ and RMQ method by Foley [1990] has C^2 continuity. One of the methods by Pottmann and Eck [1990] that was based on Foley's modified method may have up to C^{∞} continuity, whereas the methods by Lawson [1984], Renka [1984], Nielson and Ramaraj [1987], and Wahba [1981, 1984] all have only C^1 continuity. Any planar interpolation mapped onto an entire sphere can only have C^0 continuity, i.e. will not be continuously differentiable, as there is no C^1 mapping function for this transformation.

Taking into account the continuity properties, comparative accuracy, ability to efficiently handle large numbers of data points, ease of implementation, and adaptability, we decided to use a combination of the modified multiquadric method that was first presented by Foley [1990] and the partitioning method by Pottmann and Eck [1990] for the NCEP grids that had 2.5 by 2.5 degree resolution. Multiquadric interpolation was first introduced by Hardy [1971], the method is often referred to as Hardy's multiquadric. Over the years this method has been shown to perform exceptionally well in experimental applications and comparative tests. For a while it appeared there was no mathematical basis to explain it's efficiency, and this produced a certain amount of skepticism about the method. It was eventually shown by Hardy and Nelson [1986] that the multiquadric and reciprocal multiquadric methods are a type of biharmonic analysis, physically related to disturbing potential fields. An exhaustive review of all the significant papers on this method was provided by Hardy [1990], including applications in numerous fields and mathematical theory and support.

The partitioning regions can be chosen based on the data point distribution such that each region has approximately the same number of points included. After evaluating a number of different configurations we decided to use a set of 20 regions, distributed to best equalize the number of data points included in each region, for the 2.5 by 2.5 degree NCEP grids. Two of the regions

are at each pole, and the other 18 are in three staggered rows of 6, one row centered on the equator and the other two at higher latitudes in each hemisphere. In order to obtain approximately 800 data points in each region, the radii of the spherical caps which define the regions become smaller nearer to the poles. When choosing the number of regions to use we attempted to use the least number possible and still have less than 1000 points each of the regions. If the number of points in a region is much higher than 1000 the matrix inversion that is required as part of the multiquadric method will take too much time to run.

This interpolation method has two main user defined parameters, i.e., whether to use multiquadric (MQ) or reciprocal multiquadric (RMQ) method and the value of R^2. While the multiquadric method has performed very well with theoretical and real problems, the choice of the parameter R^2 has remained largely ad hoc [*Carlson and Foley,* 1991]. A series of tests on the NCEP global analyses were run to find the best user parameters for our data. The full 2.5° by 2.5° grid was decimated to a 5° by 5° grid. We then used the 5° by 5° grid to interpolate to a 2.5° by 2.5° grid and compared this to the true grid. This was done many times for both MQ and RMQ methods and a range of R^2 values from 10^{-8} to 1000. The fields needed for calculating surface pressure are geopotential height, temperature and relative humidity. Examples of these fields, with their data values scaled to between zero and one, were used to run the tests. Different values for R^2 were compared by calculating a root mean square (rms) error for each interpolation. For each of the three data types the lowest rms error was for $R^2 = 0.01$ with the MQ method, except for one example where the RMQ method provided a marginally lower rms error. The total rms error for the geopotential height field at the 1000 hPa level was 4.65 meters from an example field January 1, 0 GMT, 1996. If we assume an approximate 0.125 hPa to 1 meter correspondence between surface pressure errors and geopotential height errors, and 2.3 mm to 1 hPa correspondence between delay errors and surface pressure errors, there is approximately 0.29 mm of delay error per 1 meter of geopotential height error. Therefore we have approximately 1.4 mm of delay error due to spatial interpolation (averaged over the whole globe), which is much less than the 20 mm total error budget.

Since 1996, the horizontal resolution of the NCEP global analyses has increased from 2.5 by 2.5 degrees to 1 by 1 degrees, for a total of 65,160 points, a factor of six increase. When we attempted to apply the multiquadric interpolation method to this more densely spaced grid we

encountered problems. The MQ method requires that the globe be divided into a number of overlapping regions with less than approximately 1000 points. Any more than that and the matrix inversion used in the interpolation becomes inefficient. Due to the spacing and density of the grid points we would have to separate the globe into over 600 regions, a substantial increase from the 20 regions for the 2.5 by 2.5 degree grid. This large number of regions would negate much of the advantage achieved in using a more complex interpolation method. The memory requirements to implement this method on the 1 by 1 degree grid also became too onerous. We therefore decided to use the simpler method of bilinear interpolation. We reasoned that this should be sufficient given the density of the data and the relatively smooth nature of the upper atmospheric fields.

Bilinear interpolation has the form

$$\begin{aligned} f(\phi, \lambda) &= a + bX + cY + dXY \\ a &= f(\phi_1, \lambda_1) \\ b &= f(\phi_1, \lambda_2) - f(\phi_1, \lambda_1) \\ c &= f(\phi_2, \lambda_1) - f(\phi_1, \lambda_1) \\ d &= f(\phi_1, \lambda_1) + f(\phi_2, \lambda_2) - f(\phi_1, \lambda_2) - f(\phi_2, \lambda_1) \\ X &= (\lambda - \lambda_1)/(\lambda_2 - \lambda_1) \\ Y &= (\phi - \phi_1)/(\phi_2 - \phi_1) \end{aligned} \tag{2.26}$$

where f is the field value, ϕ is latitude, and λ is longitude. The subscripts 1 and 2 refer to south and north latitudes, and the west and east longitudes, of the four known grid points directly surrounding the unknown point.

Any errors that arise from using bilinear interpolation will be included in the errors estimated in our validation studies. To estimate errors that arise purely from the bilinear interpolation, we decimated the 1 by 1 degree grid to 2 by 2 degrees, then interpolated back to the original grid. The interpolated values are then differenced from the original 1 by 1 degree grid values. This gives an upper bound on the interpolation errors, as we are using the coarser grid to interpolate. The field we used for testing is the 1000 hPa geopotential height field (GPH). This is the most appropriate field to use, since the surface pressure algorithm integrates from an interpolated upper atmospheric GPH fields down to the surface. Average global surface pressure is approximately 1013 hPa, therefore the 1000 hPa GPH field is the one most likely to be used in the surface pressure algorithm. The error in the GPH field can then be approximately converted to delay error using the 0.29 mm of delay to 1 meter height change correspondence, as discussed in the multi-

quadratic interpolation error assessment.

We examined four different GPH fields over a 24 hour period for January 1, 1999. Figure 2.7 shows the results for one of these fields, at 0 GMT. The top plot is the original 1 by 1 degree GPH field, and the bottom plot is the interpolated field minus the original field. It can be seen that the greatest amount of interpolation error occurs where the GPH field has the highest gradients, for example over the Tibetan Plateau, the Andes, and parts of Antarctica. Although the total range of GPH differences are generally ±50 m, 95% of the differences are in the range of ±5 m, i.e. approximately ±1.5 mm of delay. For the field shown in Figure 2.7, the total global average GPH rms error is 2.5 m, or 0.7 mm rms delay error.

Figure 2.8 shows the rms error in zonal averages of 5 degree latitude bands. All four 6 hour time steps for January 1, 1999 are shown to illustrate of the short time scale variability in interpolation error. There is no much variation between time steps, therefore we may assume that the errors for these example fields are typical of the general errors. The peaks in the plot around 80°S and 35°N correspond to the increased errors generally seen over the Tibetan Plateau and parts of Antarctica. However, the zonal rms GPH errors are all less than 7 m, corresponding to 2 mm delay error, which is only a fraction of the 20 mm total error budget for atmospheric delay. This is an upper bound on the interpolation error since we are using 2 by 2 degree fields to interpolate. Interpolation errors will be part of any errors estimated by validation studies using ground station meteorological observations.

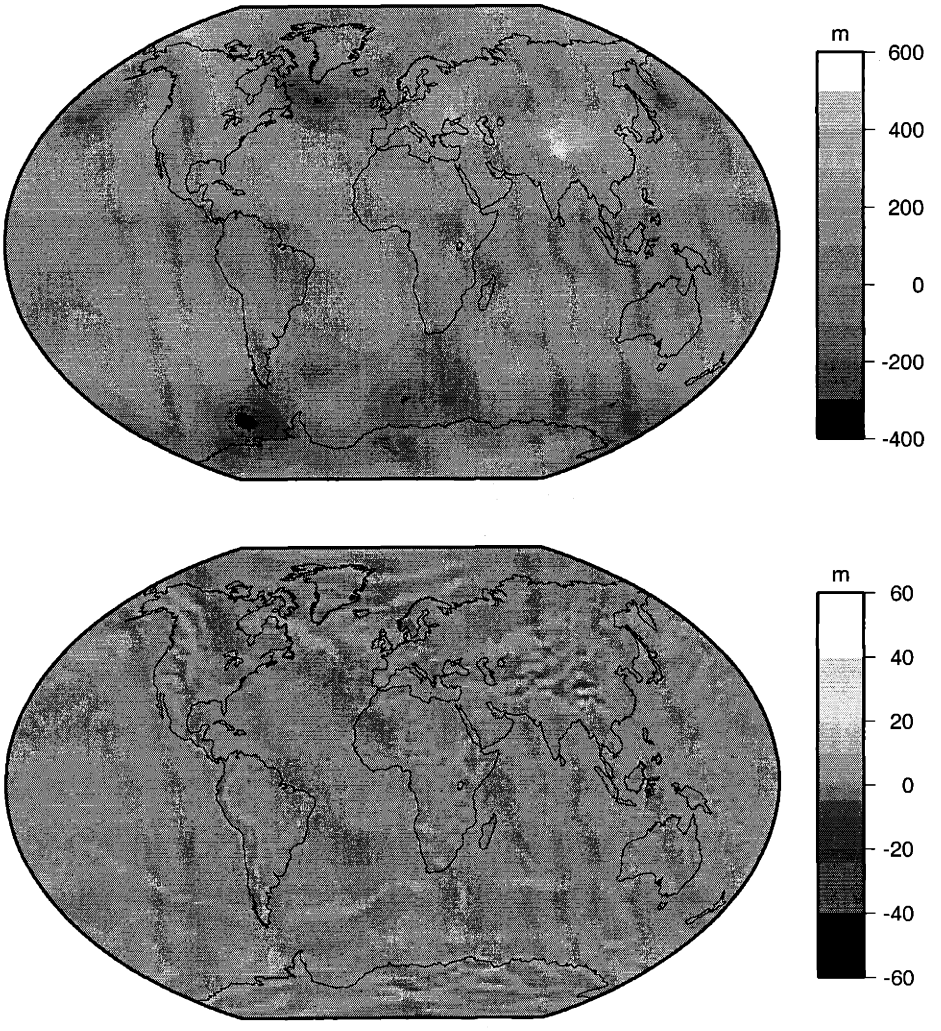

Figure 2.7. Top plot is the 1 by 1 degree 1000 hPa geopotential height field for 0 GMT, January 1, 1999. Bottom plot is the 2 by 2 degree to 1 by 1 degree interpolated field minus the original 1 by 1 degree field.

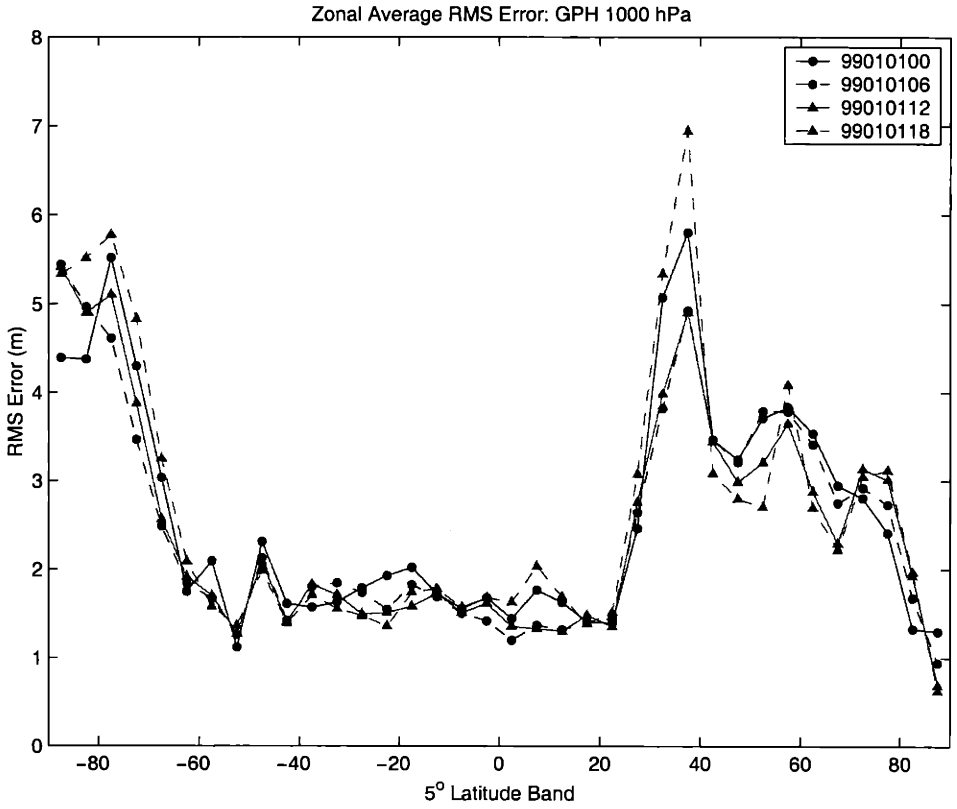

Figure 2.8. Zonal average 1000 hPa geopotential height field rms errors, 5° latitude bands, for January 1, 1999.

2.2.7 Temporal Interpolation

The NCEP fields used to model atmospheric delay are only produced every 6 hours. To estimate delay values at the times of the laser pulses we will need to temporally interpolate between the NCEP output times. Since surface pressure is the major contributor to atmospheric delay, we can look at the temporal behavior of surface pressure to guide our temporal interpolation scheme. Spectral plots of surface pressure are used to characterize the statistical properties of the time series. For example, if a log-log plot of power spectral density versus frequency has a slope of -2 then the time series can be described as a random walk process. For these processes, the maximum likelihood interpolator is simply a linear interpolation between adjacent points.

Figure 2.9 shows power spectral density plots for four automatic weather stations (AWS) in Antarctica that have 2 years of largely uninterrupted surface pressure time series, for 1998 and

1999. The AWS has a sampling period of 10 minutes, short gaps in the data were bridged using linear interpolation. Analysis of the power spectra showed that log-log plots of these spectra fall off at high frequencies with an approximate slope of -2.5, if some of the white noise tail is ignored. This slope is close to -2, and therefore consistent with a random walk stochastic process. When we take the NCEP surface pressure data and linearly interpolate to 10 minutes, the errors with respect to the AWS data are generally small compared to the overall variability of the surface pressure. Two examples for Theresa station during the winter when surface pressure variability is the greatest are given in Figure 2.10. Figure 2.10a is a five day segment of data that shows one of the best examples of the applicability of linear interpolation. The variability between 6 hourly NCEP data points is very small and the NCEP data follow all the surface pressure variations. Figure 2.10b is an example of where linear interpolation does not work well. It should be noted that there is an NCEP data point missing here. In general, the errors arise as a result of the NCEP data not following the gross pressure variations, rather than the linear interpolation being inaccurate.

The power spectral density plots for the AWS data may be used to estimate how much variance in surface pressure is missed by using the coarser temporal resolution NCEP fields. The additional variance is the power integrated under the power spectral density plots for frequencies higher than the NCEP Nyquist frequency. The current NCEP global analyses are produced every 6 hours, therefore the Nyquist frequency is 2 cyc/day. This frequency is indicated by a vertical line on the plots in Figure 2.9. The additional integrated power was approximately 0.01 hPa for Theresa and Nico stations, 0.02 hPa for Manuela, and 0.1 hPa for Marilyn. This corresponds to a delay error of no more than 0.3 mm due to the temporal resolution of the NCEP fields, which is negligible compared to the 20 mm error budget and other error sources.

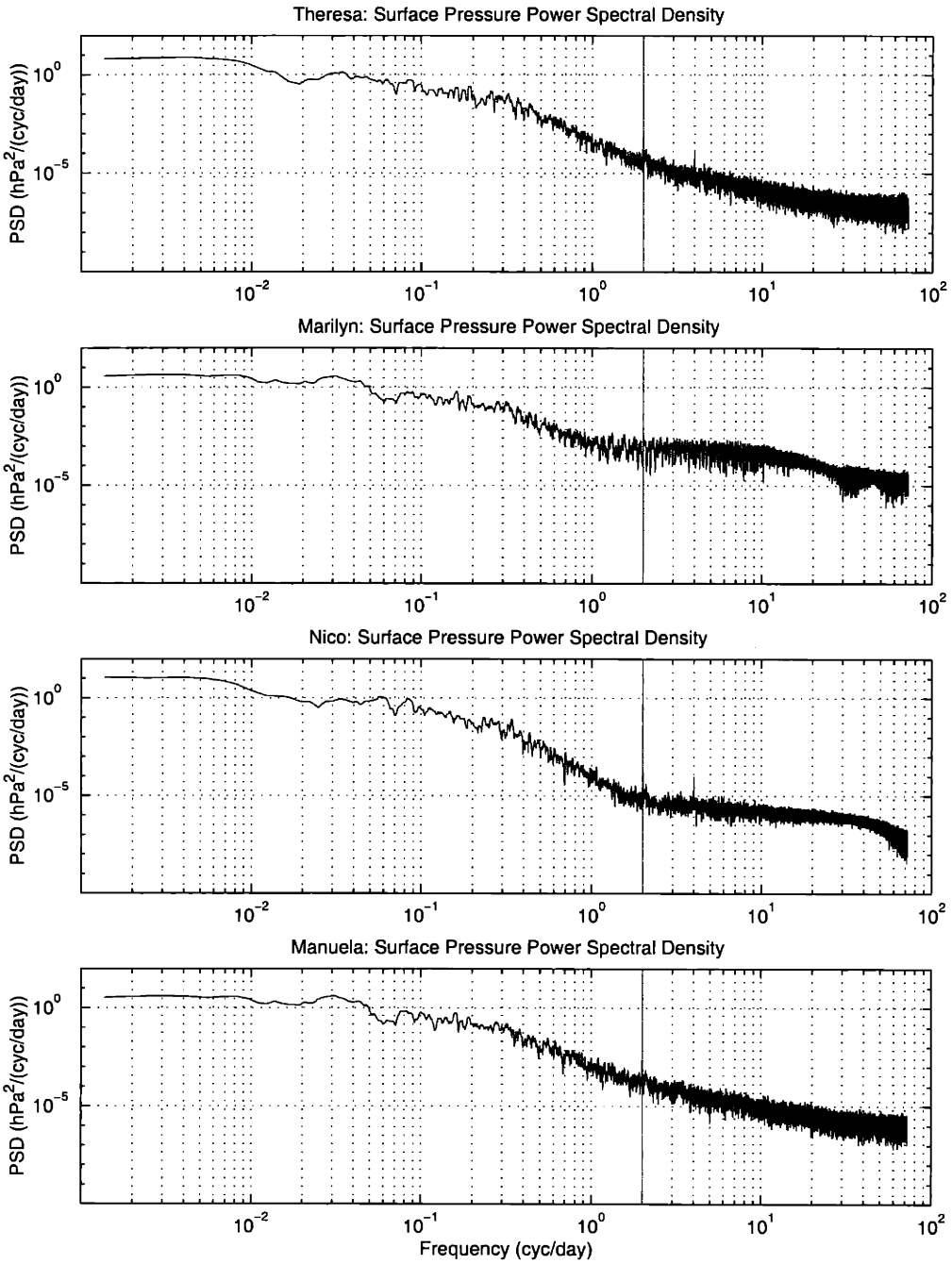

Figure 2.9. Surface pressure power spectral density plots for four automatic weather stations in Antarctica for 2 years of data, 1998 and 1999. Sampling interval is 10 minutes. Vertical line shows the nyquist frequency for the 6 hour sampling interval NCEP data.

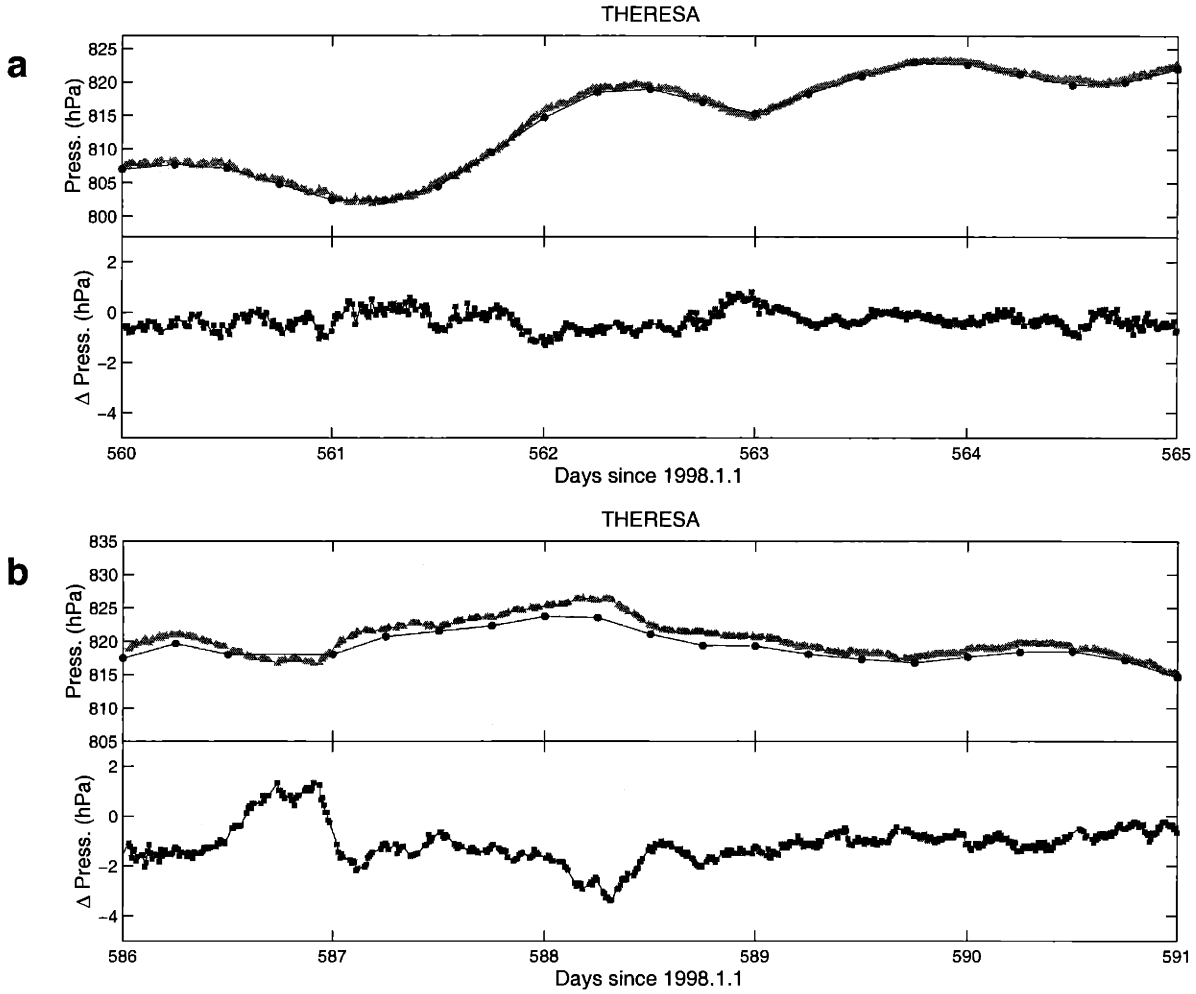

Figure 2.10. Comparison of 6 hour linearly interpolated NCEP surface pressure data to 10 minute AWS measurements for Theresa AWS unit. Upper plots show NCEP surface pressure values (squares) and AWS values (triangles). Lower plots are surface pressure differences (NCEP minus AWS). Note that the vertical scales are the same for each segment of the time series.

2.2.8 Coordinate Systems

The calculation of atmospheric delay at the laser footprint locations requires knowledge of the footprint latitude, longitude, and initial height estimate. The laser footprint coordinates are given as geodetic latitude, longitude, and height above ellipsoid [*Schutz,* 1999]. The reference ellipsoid used is WGS-84, defined by semi-major axis a (6378137.0 m), semi-minor axis b (6356752.3142 m), and first eccentricity squared e^2 (0.00669437999013) [*NIMA,* 1997]. Howeve,r all of the atmospheric data from NCEP are referenced to orthometric height, i.e. height

above geoid. Thus, we need to convert the laser footprint ellipsoid height to height above geoid. The height difference between the coordinate systems can range from -100 m to 100 m, leading to a delay difference of approximately 23 mm to -23 mm. To calculate orthometric height we need to know the value of the geoid at the footprint location. Let H be the orthometric height, h be the ellipsoid height, and N_g be the geoid value. Then the height conversion is

$$H = h - N_g \tag{2.27}$$

The geoid values may be calculated using the National Imagery and Mapping Agency 30 arc-minute geoid grid as defined for WGS-84 [*NIMA*, 1997], and is interpolated using bilinear interpolation to the footprint locations.

2.2.9 Processing Flow

There are two separate processes for calculating the atmospheric delays. The "background" process is the archiving of the required NCEP data. These data should be archived on-site as it is only posted to the NOAA ftp site for 24 hours before being replaced by the next day's data. After the required fields are extracted, the daily volume of data (as of March 2000) is 25.8 Mbytes. The main process is the calculation of the delays. The timing of the delay calculation is driven by two data streams: the NCEP fields and the laser ranges. In order to calculate the delays within 12 hours of real time, an assuming that the laser ranges are available in a timely fashion, the biggest impediment to delay processing is the up to 9.5 hour time lag on the 12Z FNL analysis field (Table 2.1). The following processing flow assumes that the laser range data is available on a much shorter time lag than the NCEP fields. All the processing is done in 6 hour time blocks, as this is the time step of the NCEP fields.

Let t_1 be a given 6 hourly time step, and let t_2 be the next time step. Let P_{12} be a set of all laser range footprints with a time tag, t, such that $t_1 \leq t < t_2$.

1. Between t_1 + 5 hr and t_1 + 9.5 hr: Access NCEP fields for t_1. If FNL analysis is archived on-site, proceed. If not archived, attempt to retrieve from the NOAA ftp site. If not available, use the next best analysis for forecast.

2. Calculate delays for P_{01} at time value t_1.

3. Interpolate with respect to time delays for P_{01} at t_0 and P_{01} at t_1. (Note, delays for P_{01} at t_0 were calculated in the previous loop of this process). Save these delay values.

4. Calculate delays for P_{12} at time value t_1. Do these calculations as soon as laser ranges come in, and make sure they are completed before the next time step.

5. Repeat for next time step (t_2).

2.3 Validation

The error budget set out in the GLAS science requirements assumes less than 20 mm single shot atmospheric delay rms error [*GLAS Science Team*, 1997]. To validate the atmospheric delay estimate requires that we validate our surface pressure and precipitable water vapor estimates, especially in the polar regions. We have already performed a number of pre-launch validation studies. The surface pressure and precipitable water vapor validation will be continuously performed and monitored over the lifetime of the ICESat mission.

Sources of readily obtainable surface pressure measurements are Automatic Weather Stations (AWS) in Antarctica and Greenland [*Sterns and Wendler*, 1988; *Steffen et al*, 1996], and GPS stations with meteorological packages. Comparisons of model estimates with polar AWS's for one year data in 1999 showed an rms error of less than 5 mbar once a mean offset was removed. The majority had less than 3 mbar rms error. The offset removal is justified as the station heights are not accurately known. These rms surface pressure errors correspond to delay errors of less than 12 mm, and usually less than 7 mm. This validation study is described in Chapter 2.

Precipitable water vapor data are harder to come by, although the technique of GPS meteorology can provide some data for validation. GPS processing produces an estimate of total delay at microwave wavelengths, which is much more sensitive to water vapor than optical wavelengths. If the surface pressure at the GPS station is known then precipitable water vapor estimates can be derived. If the station does not have an on-site meteorological package then our NCEP surface pressure model may be used, greatly increasing the amount of available data. The error associated with using NCEP surface pressure is approximately 1.6 mm of precipitable water vapor (PW). We have used this method to compare 8 GPS stations in Antarctica and 2 in Greenland that are

part of the IGS global network, for the first 6 months of 2000. The rms errors are all less than 2 mm of precipitable water vapor (i.e. 0.16 mm of delay), which is almost negliable and of the same order as the measurements themselves. This validation study is described in Chapter 3.

2.4 Summary

A successful employment of GLAS requires a correction for atmospheric delay from refractivity. The refractivity equations used are based on Owens formulas [1967], modified for an increased concentration of atmospheric carbon dioxide from 300 ppm to 375 ppm. This refractivity formulation is more suitable for satellite laser altimetry, rather than the formulas recommended by IUGG for ground based geodesy. The refractivity equation used contributes less than 0.2 mm to the total delay error.

When the refractivity equation is integrated through the atmosphere, the zenith delay can be shown to be directly related to surface pressure and total column precipitable water vapor. For pointed angles off zenith a mapping function relates the total delay to the zenith delay. The error associated with the simple mapping function used is less than 0.5 mm for pointing angles of less than 10° and decreases to zero for nadir pointing. Surface pressure is calculated using the NCEP global analyses. NCEP produces 1° by 1° gridded fields of atmospheric variables, including temperature, geopotential height, and relative humidity, at a number of standard pressure levels every 6 hours. These atmospheric fields are spatially interpolated to the location of the laser footprints, the delay error due this interpolation is less than 2 mm. There is also an error associated with the temporal interpolation used to estimate delay at the laser pulse time tags. By using higher temporal resolution automatic weather station surface pressure data, we estimated this error to be less than 0.3 mm. A hydrostatic equilibrium model of the atmosphere is integrated from the upper atmospheric levels to the estimated height of the laser footprint in order to calculate surface pressure. The NCEP global analyses give total column precipitable water vapor as a single field, and this is used without modification.

Examples of zenith atmospheric delay over Antarctica and Greenland are shown in Figures 2.11 and 2.12, for 0 GMT January 1, 1998. The seasonal and interannual variation will largely depend on surface pressure variations. Trenberth [1981] gives an overview of global pressure variations. The large scale seasonal surface pressure variations over the globe vary with latitude.

In the tropics the variation is annual with a peak in the winter and total variation on the order of a few millibars. In the Southern polar regions there is a strong semi-annual signal with peaks in Spring and Autumn and total variation magnitude is approximately twice as much as the tropics. The semi-annual pattern is in the North polar regions as well but not as strong. The mid-latitudes are the transition zones between the annual and semi-annual patterns.

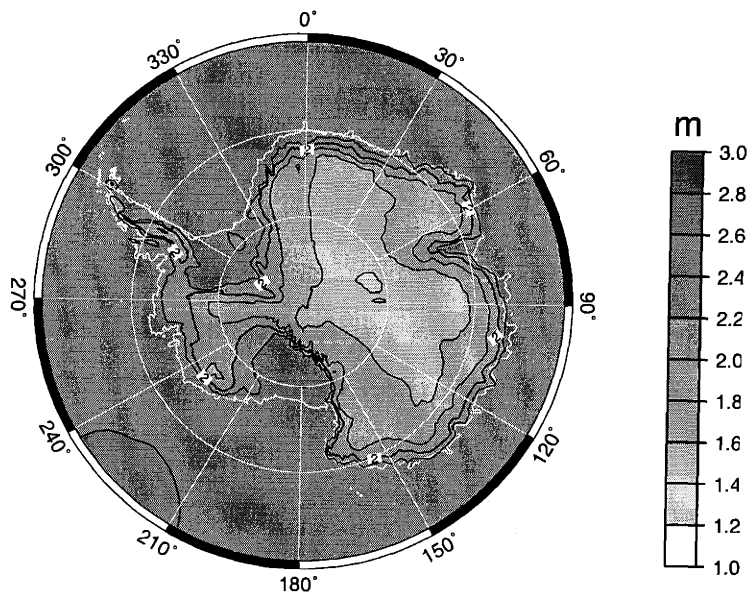

Figure 2.11. Zenith atmospheric delay for Antarctica, 0 GMT January 1, 1998.

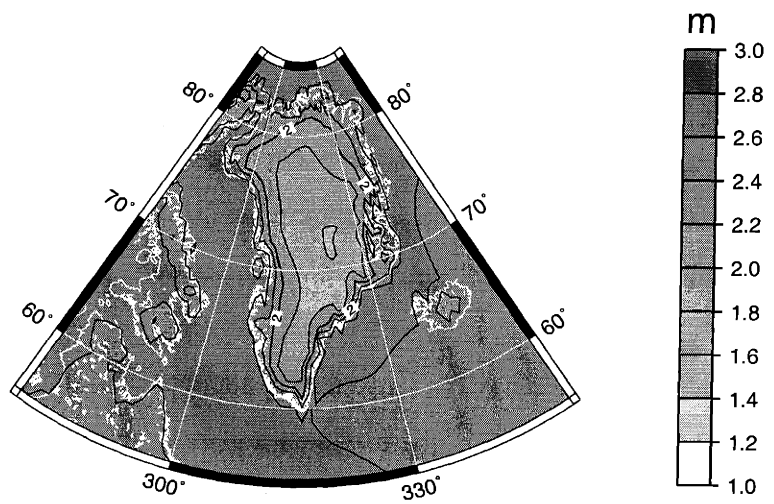

Figure 2.12. Atmospheric delay for Greenland, 0 GMT January 1, 1998.

To validate the atmospheric delay estimate requires that we validate the surface pressure and precipitable water vapor estimates, especially in the polar regions. The next two chapters discuss these validations in detail, looking for spatial and temporal patterns and correlations that may adversely affect the interpretation of ICESat data. The major error source appears to be the surface pressure estimate, the validation studies will particularly focus on this estimate.

A summary of the delay errors estimated in this chapter are given in Table 2.2.

Table 2.2: Subset of atmospheric delay errors

Error Source	Contribution
Refractivity model	0.2 mm
Mapping function (for pointing angles < 10°)	0.5 mm
NCEP direct PW field (vs. integrated value)	0.1 mm
Spatial interpolation	2 mm
Temporal interpolation	0.3 mm
Total ICESat atmospheric delay error budget	**20 mm**

Appendix A: Calculation of Surface Pressure

An atmospheric model of pressure with respect to height is required to reduce the upper level NCEP fields to a surface pressure. To simplify the physical model of the atmosphere we will make certain assumptions. A static atmosphere model will allow us to consider the vertical distribution of atmospheric variables. Although the atmosphere is actually a dynamic system, static atmosphere formulas for variables like pressure and density are valid to a high degree of accuracy. We will assume a horizontally stratified atmosphere in hydrostatic equilibrium, such that pressure is related to height by the hydrostatic equation

$$dP = -g(Z)\rho(Z)dZ \tag{A1}$$

where Z is geometric height, P is pressure, g is gravity, and ρ is density.

To allow easier integration of this equation, we will convert geometric height into geopotential height. A geopotential meter is defined as the work done by lifting a unit mass one geometric meter through a region in which gravity is uniformly 9.80665 m/s^2, the value of mean sea level gravity. The geopotential measured with respect to mean sea level (assumed zero potential) is called geopotential height, H, such that

$$H = \frac{1}{g_0}\int_0^Z g\,dz \tag{A2}$$

where g_0 = 9.80665 m^2/s^{2}m' [*NOAA*, 1976]. The derivative of this equation with respect to geometric height is

$$g_0 dH = g dZ \tag{A3}$$

This can be substituted into the hydrostatic equation to give

$$dP = -g_0\rho(H)dH \tag{A4}$$

We now require an expression that will convert elevation in geometric meters to geopotential meters. This will be related to the variation of gravity with height. Approximating the Earth as a sphere with only radial mass variations, gravity is inversely proportional to radius squared, which will give a conversion equation of

$$g = g_{msl}\left(\frac{R^2}{(R+Z)^2}\right) \tag{A5}$$

where R = 6371009 m is the mean radius of the Earth, g_{msl} is gravity at mean sea level. Substitut-

ing this equation for gravity into Equation A2 gives the conversion formula

$$H = \frac{g_{msl}}{g_0}\frac{RZ}{(R+Z)} \tag{A6}$$

Mean sea level gravity depends on geodetic latitude, the formula is based on calculations of the standard geodetic reference system [*Moritz*, 1980] such that

$$g_{msl} = g_{eq}(1 + k\sin^2\phi)(1 - e^2\sin^2\phi)^{-\frac{1}{2}} \tag{A7}$$

where ϕ is latitude, $g_{eq} = 9.7803267715$ m/s^2, $k = 0.001931851353$, $e^2 = 0.00669438002290$.

Many atmospheric models, such as the U.S. Standard Atmosphere [*NOAA*, 1976], simplify their calculations for pressure by assuming the air to be a dry, ideal gas. We shall include non-ideal gas effects and water vapor partial pressure. The equation of state for a pure non-ideal gas is

$$Z^{-1}\frac{PV}{RT} = \frac{m}{M} \tag{A8}$$

where Z^{-1} is called the inverse compressibility and depends empirically on pressure and temperature [*Harrison,* 1965b], P is pressure, V is volume, R is the universal gas constant, T is temperature, m is mass, and M is molecular weight.

Density can be written as $\rho = m/V$, and we can split mass components of water and dry air: $m = m_w + m_d$. If we assume that moist air obeys Dalton's Law of partial pressures, the separate masses can be evaluated by the non-ideal equation of state to give a density equation of

$$\rho = \frac{1}{RT}(Z_w^{-1}P_wM_w + Z_d^{-1}(P - P_w)M_d) \tag{A9}$$

where $R = 8314.510$ J/kmol.K, $M_w = 18.0152$ kg/kmol, $M_d = 28.9632$ kg/kmol for 375 ppm carbon dioxide concentration, P is the total pressure and P_w is the partial pressure of the water vapor in the air. It is implicitly assumed that the dry air components are homogeneously mixed throughout the lower atmosphere and therefore the mean molecular weight of dry air is a constant.

Equations for inverse compressibility have been experimentally determined by Owens [1967], these formulas are accurate to within a few parts per million

$$Z_w^{-1} = 1 + 1650\frac{P_w}{T^3}[1 - 0.01317(T - 273.15) + 1.75\times10^{-4}(T - 273.15)^2 + 1.44\times10^{-6}(T - 273.15)^3] \tag{A10}$$

$$Z_d^{-1} = 1 + (P - P_w)\left[57.90\times10^{-8}\left(1 + \frac{0.52}{T}\right) - 9.4611\times10^{-4}\frac{(T - 273.15)}{T^2}\right] \quad \text{(A11)}$$

We need an equation for water vapor pressure. Given sufficient saturation vapor pressure data over a wide range of temperature, the information can be stored in an analytical form. One of the better forms uses Chebyshev polynomials [*McGarry,* 1983]

$$T\log_{10}\left(\frac{P_s}{P_b}\right) = \frac{a_o}{2} + \sum_{s=1}^{n} a_s E_s(x) \quad \text{(A12)}$$

where P_b = 1000 Pa, P_s is saturation vapor pressure, $E_s(x)$ are Chebyshev polynomials:

$$\left.\begin{aligned} E_0(x) &= 1 \\ E_1(x) &= x \\ E_{s+1}(x) &= 2xE_s(x) - E_{s-1}(x) \\ x &= \frac{2T - (T_{max} + T_{min})}{T_{max} - T_{min}} \end{aligned}\right\} \quad \text{(A13)}$$

The coefficients a_s (s = 0,...,10) are a_s = {2794.027, 1430.604, -18.234, 7.674, -0.022, 0.263, 0.146, 0.055, 0.033, 0.015, 0.013}, T_{max} = 648 K, and T_{min} = 273 K [*Ambrose*, 1987].

To get the water vapor pressure from the saturation vapor pressure we use relative humidity [*Harrison*, 1965a]

$$P_w = RhP_s \quad \text{(A14)}$$

where relative humidity is in a fractional form with values between 0 and 1. Actually, this equation is only true for pure water vapor, not moist air. However, the equation is approximately true for moist air. Note that the World Meteorological Organization has adopted the practice of evaluating relative humidity with respect to liquid water at all temperatures, even those below 0 °C.

We now have an expression for density that depends on temperature, relative humidity and pressure. To solve the hydrostatic equation we must express temperature and relative humidity as functions of geopotential height, in order to get an expression for density that only depends on geopotential height. The NCEP global analyses have values for temperature, geopotential height and relative humidity at standard pressure levels. We shall assume that temperature varies linearly with respect to geopotential height between these levels, a relatively good assumption for the

lower atmosphere such that

$$T = T_0 + L(H - H_0) \tag{A15}$$

$$L = \frac{T_1 - T_0}{H_1 - H_0} \tag{A16}$$

where L is the temperature gradient; T_0 and H_0 are temperature and geopotential height at the upper level; T_1 and H_1 are temperature and geopotential height at the lower level: $H_1 < H \leq H_0$. We will also assume that relative humidity varies linearly with respect to geopotential height between levels such that

$$Rh = Rh_0 + S(H - H_0) \tag{A17}$$

$$S = \frac{Rh_1 - Rh_0}{H_1 - H_0} \tag{A18}$$

where S is the relative humidity gradient, Rh_0 is relative humidity at the upper level, Rh_1 is relative humidity at the lower level. Given these expressions for temperature and relative humidity, the hydrostatic equation becomes

$$\frac{dP}{dH} = -\frac{g_0}{RT}[Z_w^{-1}(H)P_w M_w + Z_d^{-1}(H, P)[P - P_w(H)]M_d] \tag{A19}$$

This differential equation is first order, non-linear and inhomogeneous, we are not able find an analytic solution. To obtain a numerical solution for pressure we will numerically integrate down from the upper level geopotential height to the desired geopotential height. Pressure varies smoothly with geopotential height, this means that we are relatively unrestricted in our choice of numerical method. We will use the Bulirsch-Stoer method, this method is one of the best ways to obtain high accuracy solutions with minimal computational effort, so long as integrated function is smooth and has no singular points within the range of integration [*Press et al.,* 1989].

References

Ambrose, D., Pressure-volume-temperature, in *Recommended Reference Materials for the Realization of Physiochemical Properties*, K. N. Marsh ed., Blackwell Sci. Pub., 73-114, 1987.

Astronomical Almanac, U. S. Government Printing Office, 1999.

Birch, K. P. and M. J. Downs, Corrections to the updated Eldén equation for the refractive index of air, *Metrologia, 31,* 315-316, 1994.

Boer, G. J., K. Arpe, M. Blackburn, M. Deque, W. L. Gates, T. L. Hart, H. le Treut, E. Roeckner, D. A. Sheinin, I. Simmonds, R. N. B. Smith, T. Tokioka, R. T. Wetherald and D. Williamson, Some results from an intercomparison of climates simulated by 14 atmospheric general circulation models, *J. Geophys. Res., 97,* 12771-12786, 1992.

Carlson, R. E. and T. A. Foley, The R^2 parameter in multiquadric interpolation, *Comp. Math. Appl., 21*, 29-42, 1991.

Ciddor, P. E., Refractive index of air: new equations for the visible and infrared, *Appl. Opt., 35,* 1566-1573, 1996.

Ciddor, P. E. and R. J. Hill, Refractive index of air. 2. Group index, *Appl. Opt., 38,* 1663-1667, 1999.

Davis, J. L., T. A. Herring, I. I. Shapiro, A. E. E. Rogers and G. Elgered, Geodesy by radio interferometry: Effects of atmospheric modeling errors on estimates of baseline length, *Radio Sci., 20,* 1593-1607, 1985.

Dongarra, J. J., *LINPACK User's Guide,* SIAM, Philadelphia, 1979.

Duda, D., J. Spinhirne, E. W. Eloranta, Atmospheric multiple scattering effects on GLAS altimetry - Part 1: Calculations on single pulse bias, *IEEE Trans Geo. Rem. Sen., 39*, 92-101, 2001.

Eldén, B., The dispersion of standard air, *J. Opt. Soc. Am., 43,* 339-344, 1953.

Eldén, B., The refractive index of air, *Metrologia, 2,* 12-80, 1966.

GLAS Science Team, Geoscience Laser Altimetry System (GLAS) Science Requirements Document, Version 2.01 (ed. B. Schutz), October 1997.

Fleagle, R. G. and J. A. Businger, *An Introduction to Atmospheric Physics,* Academic, Orlando, FL, 1980.

Foley, T. A., Interpolation to scattered data on a spherical domain, in *Algorithms for Approximation II*, M. Cox and J. Mason eds, Chapman and Hall, London, 303-310, 1990.

Foley, T. A., The map and blend scattered data interpolant on a sphere, *Comput. Math. Appl., 24,* 49-60,1992

Franke, R., Scattered data interpolation: Tests of some methods, *Math. Comp., 38*, 181-200, 1982.

Hardy, R. L., Multiquadric equations of topography and other irregular surfaces, *J. Geophys. Res., 76*, 1905-1915, 1971.

Hardy, R. L., Theory and applications of the multiquadric-biharmonic method, *Comp. Math. Appl., 19*, 163-208, 1990.

Hardy, R. L. and S. A. Nelson, A multiquadric-biharmonic representation and approximation of disturbing potential, *Geophys. Res. Lett., 13*, 18-21, 1986.

Harrison, L. P., Fundamental concepts and definitions relating to humidity, in *Humidity and Moisture*, A. Wexler ed, Reinhold Pub. Co., New York, vol. 3, 3-70, 1965.

Harrison, L. P., Imperfect gas relationships, in *Humidity and Moisture*, A. Wexler ed, Reinhold Pub. Co., New York, vol. 3, 3-70, 1965.

Heiskanen, W.A. and H. Moritz, *Physical Geodesy,* W.H. Freeman, San Francisco, 1967.

IUGG (International Union of Geodesy and Geophysics), Resolutions, 13th General Assembly, *Bull. Geodesique, 70,* 390, 1963.

IUGG (International Union of Geodesy and Geophysics), Refractive indices of light, infrared and radio waves in the atmosphere, *IAG Special Commission Report, presented at 22nd General Assembly of IUGG,* 1999.

Kanamitsu, M., Description of the NMC Global Data Assimilation and Forecast System, *Wea. and Forecasting, 4(3)*, 335-342, 1989.

Kanamitsu, M., Alpert, J. C., Campana, K. A., Caplan, P. M., Deaven, D. G., Iredell, M., Katz, B., Pan, H. L., Sela, J., and White, G. H., Recent Changes Implemented into the Global Forecast System at NMC, *Wea. and Forecasting, 6,* 425-435, 1991.

King, M. D., Y. J. Kaufman, W. P. Menzel, D. Tanre, Remote sensing of cloud, aerosol, and water vapor properties from the Moderate Resolution Imaging Spectrometer (MODIS), *IEEE Trans Geo. Rem. Sen., 30*, 2-27, 1992

Kley, D., J. M. Russell III, C. Phillips (eds.), SPARC Assessment of Upper Tropospheric and Stratospheric Water Vapour, *WCRP Report No. 113, WMO*, December 2000.

Lawson, C. L., C^1 surface interpolation for data on a sphere, *Rocky Mtn J. Math., 14*, 177-184, 1984.

Mahesh A., J. Spinhirne, D. Duda, E. W. Eloranta, Atmospheric multiple scattering effects on GLAS altimetry - Part 2: Analysis of expected errors in Antarctic altitude measurements, *IEEE Trans Geo. Rem. Sen.,* submitted August 2001.

Marini, J. W., Correction of satellite tracking data for an arbitrary tropospheric profile, *Radio Sci., 7,* 223-231, 1972.

Marini, J. W. and C. W. Murray, Correction of laser range tracking data for atmospheric refraction at elevation angles above 10 degrees, *NASA Tech. Rep. X-591-73-351*, 1973.

McGarry, J., Correlation and Prediction of the Vapor Pressures of Pure Liquids over Large Pressure Ranges, *Ind. Eng. Chem. Process Des. Dev., 22*, 313-322, 1983.

Moritz, H., Geodetic Reference System 1980, *Bulliten Geodesique, 54(3),* 395-405, 1980.

National Imagery and Mapping Agency, Department of Defense World Geodetic System 1984: Its Definition and Relationships with Local Geodetic Systems, *NIMA Tech. Rpt 8350.2,* Bethesda, MD, Third Edition 4 July, 1997.

National Oceanic and Atmospheric Administration, U.S. Standard Atmosphere, 1976.

Niell, A. E., Global mapping functions for the atmospheric delay at radio wavelengths, *J. Geophys. Res., 101(B2),* 3227-3246, 1996.

Nielson, G. M. and R. Ramaraj, Interpolation over a sphere based upon a minimum norm network, *Comp. Aided Geom. Des., 4*, 313-321, 1987.

Owens, J. C., Optical refractive index of air: Dependence on pressure, temperature, and composition, *Appl. Opt., 6,* 51-59, 1967.

Palm, S., W. Hart, D. Hlavka, D. Duda, J. Spinhirne, GLAS Atmospheric Data Products ATBD, Version 2.0, February 1999.

Parrish, D. F., and Derber, J. C., The National Meteorological Center's Spectral Statistical-Interpolation Analysis System, *Mon. Wea. Rev.*, vol. 120, 1747-1763, 1992.

Peck, E. R. and K. Reeder, Dispersion of Air, *J. Opt. Soc. Am., 62,* 958-962, 1972.

Pottmann, H., Interpolation on surfaces using minimum norm networks, *Comp. Aided Geom. Des., 9*, 51-67, 1992.

Pottmann, H. and M. Eck, Modified multiquadratic methods for scattered data interpolation over a sphere, *Comp. Aided Geom. Des., 7*, 313-321, 1990.

Press, W. H., B. P. Flannery, S. A. Teukolsky, W. T. Vetterling, Numerical Recipes, Cambridge Uni. Press, 1989.

Quinn, K. J., Annual report of the GLAS tropospheric delay science team, 1996.

Renka, R. J., Interpolation of data on the surface of a sphere, *ACM Trans. Math. Software, 10*, 417-436, 1984.

Rüeger, J. M., *Electronic Distance Measurement - An Introduction*, Springer-Verlag, NY, 1996.

Saastamoinen, J., Atmospheric correction for the troposphere and stratosphere in radio ranging of satellites, in *The Use of Artificial Satellites for Geodesy, Geophys. Monogr. Ser., vol. 15,* edited by S. W. Henriksen, A. Mancini, and B. H. Chovitz, 247-251, AGU, Washington D. C., 1972.

Schutz, B., GLAS Geolocation, *GLAS Algorithm Theoretical Basis Document,* Uni. Texas, 1999.

Stackpole, John D., The WMO Format for the Storage of Weather Product Information and the Exchange of Weather Product Messages in Gridded Binary Form, *NOAA Office Note 388,* 1994.

Steffen, K., J. E. Box, and W. Abdalati, Greenland Climate Network: GC-Net, *in Colbeck, S. C. Ed. CRREL 96-27 Special Report on Glaciers, Ice Sheets and Volcanoes, trib. to M. Meier,* 98-103, 1996.

Stearns, C. R., and G. Wendler, Research results from Antarctic automatic weather stations, *Rev. Geophys., 26 (1)*, 45-61, 1988.

Trenberth, K. E., Seasonal variations in global sea-level pressure and the total mass of the atmosphere, *J. Geophys. Res, 86(C6),* 5238-5246, 1981.

Trenbreth, K. E. and J. G. Olsen, An evaluation and intercomparison of global analyses from the National Meteorological Center and the European Centre for Medium Range Weather Forecasts, *Bull. Am. Met. Soc, 69,* 1047-1057, 1988.

Wahba, G., Spline interpolation and smoothing on a sphere, *SIAM J. Sci. Stat. Comp., 2*, 5-16, 1981. See also errata, *SIAM J. Sci. Stat. Comp. 3*, 385-386, 1981.

Wahba, G., Surface fitting with scattered noisy data on Euclidean *d*-space and on the sphere, *Rocky Mtn J. Math., 14*, 281-299, 1984.

Zwally, H. J., B. Schutz, W. Abdalati, J. Abshire, C. Bentley, A. Brenner, J. Bufton, J. Dezio, D. Hancock, D. Harding, T. Herring, B. Minster, K. Quinn, S. Palm, J. Spinhirne, and R. Thomas, ICESat's laser measurements of polar ice, atmosphere, ocean, and land, *submitted to J. of Geodynamics,* 2001.

Chapter 3

Comparisons of Antarctic Automatic Weather Station Surface Pressure Data to NCEP Global Analyses.

3.1 Introduction

As described in Chapter 2, the ICESat atmospheric delay correction is primarily dependent on the value of surface pressure at the laser footprint location. For the component of delay that depends on surface pressure there is approximately 2.35 mm of delay for every 1 hPa of surface pressure, i.e. 2.35 m of total delay for an typical surface pressure value of 1000 hPa. Numerical weather models can provide an internally consistent global data set for calculating surface pressure that is continuously available over the whole lifetime of the mission. The National Center for Environmental Prediction (NCEP) produces one such operational model that is easily accessible by anonymous ftp. NCEP produces 1 by 1 degree uniform in latitude and longitude gridded fields of atmospheric variables, such as temperature, geopotential height, relative humidity. These fields are produced at 26 standard pressure levels from 1000 hPa to 10 hPa every 6 hours, the NCEP global analyses have been described in greater detail in Section 2.2 of Chapter 2. The upper atmospheric fields are spatially interpolated to the location of the laser footprints. A hydrostatic equilibrium model of the atmosphere is then integrated from the upper atmospheric levels to the estimated height of the laser footprint in order to calculate surface pressure, this model is detailed in Appendix A. In order to validate our delay estimates we must validate this method of calculating surface pressure against ground based measurements. The ICESat error budget allows for no more than 20 mm of atmospheric delay error [*GLAS Science Team,* 1997]. Therefore we require that the surface pressure error be no more than 8 hPa, assuming that other error sources in the atmospheric delay estimate are negligible compared to the surface pressure error. This chapter focuses on the polar regions, since they are ICESat's primary concern.

Using the NCEP direct measure of surface pressure is problematic for a variety of reasons. Primarily, NCEP uses an outdated U.S. Navy elevation dataset. Comparisons with a digital elevation dataset for Antarctica [*Drewry,* 1983] show errors of over 1 km in some locations. Areas of

greatest variability are near steep topography, such as the Transantarctic mountains. This is the leading cause of bias between the NCEP direct surface pressure field and ground station observations. Bromwich et al. [1999] calculated the average difference between the NCEP estimates and AWS measurements of surface pressure for July 1994 in Antarctica, differences of up to 170 hPa were observed. The spectral nature of the NCEP model also leads to spurious waves in the surface pressure field near areas of steep topography. Our vertical integration method of calculating surface pressure should alleviate these problems. It is essential to perform this integration rather than using the NCEP surface pressure field so that the correct heights of the laser footprints are used.

Antarctica is a data sparse region. There are also communication difficulties in transfering what data there is available in a timely manner. Due to these problems, numerical weather models tend not to be as accurate at high Southern latitudes. Studies have compared analyses produced by different forecasting centers, notably the European Center for Medium-Range Weather Forecasting (ECMWF). These comparisons show clearly the deficiencies of the models in the Antarctic regions compared to the rest of the world [*Trenberth and Olsen*, 1988]. Most of the meteorological data for Antarctica comes from manned research stations. These stations are generally located around the coast. To help alleviate this spatial distribution problem, automatic weather stations (AWS's) have been installed since 1980 to support operational weather forecasting and various other research activities [*Stearn and Wendler,* 1988]. AWS's provide the only readily available source of meteorological data with coverage across the entire continent (Figure 3.1). In this study we have used AWS surface pressure measurements to validate the NCEP surface pressure estimates used to calculate ICESat atmospheric delays.

Previous studies can be a guide to model inadequacies and problems. However, the operational NCEP global analyses system is routinely updated and modified. For this reason we should continuously monitor and validate the NCEP derived surface pressure estimates against in-situ measurements over the lifetime of the ICESat mission. On the positive side, the operational NCEP system is continuously improving. Studies have shown errors to be steadily decreasing as new data sources are added and model refinements are made [*Cullather et al,* 1997; *Trenberth and Olsen,* 1988].

A serious effort to study Antarctic meteorology and issues surrounding operational analyses and forecasts was initiated by the Antarctic First Regional Observing Study of the Troposphere

(FROST) Project [*Turner et al.,* 1996]. Using data from this project, Cullather et al. [1997] has performed the most recent and comprehensive comparison of the NCEP operational analyses and forecasts to in-situ measurements in the Antarctic region. This study compared NCEP surface pressure values to AWS measurements. The direct surface pressure field from NCEP was used and as discussed previously the direct field suffers from numerous problems. Also, a coarser NCEP grid spacing of 2.5 degrees was used, with the adjacent grid point to the AWS station that had the closest matching elevation being used for comparison. Therefore, any quantitative measure of NCEP surface pressure error derived from FROST project would be an upper bound to errors associated with our surface pressure scheme. Average monthly standard error of the surface pressure differences for a subset of AWS stations were generally less than 5 hPa, this measure is the rms error with a mean error removed to account for height biases between the NCEP and AWS values. Over the time period of the study, from 1985 to 1995, the monthly correlations between NCEP surface pressure and AWS measurements show a distinct improving trend that is attributed to changes in the operational NCEP analysis scheme. Interior stations tended to perform better than coastal stations. Monthly standard errors averaged over the 10 years of data also showed an error maximum in austral winter. Error values seem to be related to the amount of synoptic activity. This study also suggested that intense lows are underestimated by the numerical analyses, which may explain the error correlation with synoptic activity level. Another point to keep in mind is that there is less data available in winter for assimilation into the NCEP model, we would expect less accurate pressure models due to this as well.

In the next section a general description of Antarctic meteorology is given, focusing on the spatial and temporal variability of surface pressure. Note that any comparison of NCEP surface pressure estimates to AWS measurements will result in a combination of errors from both sources. Section 3.3 describes the Automatic Weather Station system and data and discusses possible errors in the data. Results of the comparisons are given in Section 3.4. We looked at 2 years worth of data in order to discern any seasonal signals in the delay errors that might be confused for seasonal signals in ice sheet height variations. Discussion and summary are given in Section 3.5.

3.2 Antarctic Weather Patterns

Weather in Antarctica is dominated by the effects of topography. Steep topographic gradients at the coast tend to block the synoptic systems that circle the continent from reaching the interior. Strong cooling over the surface of the domed shaped continent generates persistent katabatic winds, i.e. gravity driven winds that result from dense, air flowing down slope. These winds intensify in the winter when cooling is at a maximum. Surface radiative cooling also creates a temperature inversion in the lower troposphere. Surface temperatures tend to show an annual pattern called a "coreless" winter, temperatures rapidly drop in January and after April remain fairly constant, rapidly warming again in September. This temperature pattern is primarily due to the asymmetric annual cycle of incident solar radiation south of the Antarctic Circle. There is also a semiannual component in the Southern Hemisphere atmospheric circulation that reinforces the coreless winter. The distinct annual cycle and a suggestion of the semi-annual cycle can be seen in Figure 3.2, which shows two years of monthly mean AWS surface temperatures grouped by region. Each regional plot also has mean monthly climatology based on multiyear data, except for the peninsula region which does not have a long term AWS available. The annual cycle is intensified with increasing distance southward, as can be seen by comparing plateau stations to coastal or peninsula stations. A comprehensive survey of Antarctic climatology and meteorology may be found in King and Turner [1997], an overview of AWS monthly mean climatic data is given by Stearns et al. [1993].

There is an annual signal in the surface pressure field that tends to be stronger with increasing distance inland. The amplitude can be greater than 20 hPa in the interior of East Antarctica [*Parish and Bromwich,* 1997; *Radok et al.,* 1996]. There is also a semi-annual component that is more evident nearer the coast. The major feature of Antarctic surface pressure is the circumpolar trough of low pressure, which is generally located about 66 °S. This trough undergoes a distinct semi-annual variation in position and strength, with maxima at the equinoxes. The circumpolar trough dominates seasonal pressure variations at coastal locations [*King and Turner,* 1997]. Coastal locations also show much more short time scale variability due to the synoptic weather systems which circle the continent, these generally do not penetrate inland due to the steep topography of the continent. Synoptic activity level increases when the circumpolar trough deepens in spring and autumn. In general, synoptic activity level also increases during the winter. The AWS

climatic study by Stearns et al. [1993] show the annual and semi-annual surface pressure described by the above references, Figures 3.5 through 3.7 of their paper cover plateau and coastal examples. Figure 3.3 of this chapter shows similar monthly mean surface pressure data for 1998 and 1999, an overall mean value has been removed from each station for ease of viewing. Each regional plot also has mean monthly data for one station based on multiyear data, except for the peninsula region which does not have a long term AWS available. The seasonal variations are not as clear when compared to the multiyear data. Monthly means for 1998 appear to contain the signals however 1999 is clearly an anomalous year. In particular, the 6 hourly time series data show a persistent high pressure system around June 1999 (day 530) that is a departure from the expected climatology (Figure 3.5). This high pressure system is evident in station records across the whole continent, except for the peninsula stations (Figure 3.5j and 3.5k).

3.3 Automatic Weather Stations

Automatic Weather Stations are an important source of meteorological data in Antarctica, especially in the interior where there are few other observations. Since 1980 an increasing number of AWS units have been installed, for the 2 year time period of this study from 1998 to 1999 there were 51 total stations available. Data from AWS units support a large number of meteorological and climatological investigations and since 1990 AWS data has been assimilated into operational numerical weather analyses and forecasts. Stearns and Wendler [1988] and Stearns et al. [1993] describe the AWS system and results of research using the data.

The basic AWS unit consists of wind speed, wind direction, air temperature, and pressure sensors mounted on a 3 m tower. The pressure sensor is mounted approximately 2 meters above the ground, however this height is nominal due to changing snow levels over time. The pressure sensor is a Paroscientific digiquartz pressure transducer, it is reported to be accurate to $\pm$ 0.1 hPa and calibrations should be within $\pm$ 0.2 hPa [*Stearns et al.,* 1993]. This type of pressure transducer can drift downwards with time, manufacturor specifications state that the long term pressure drift is no more than 0.1 hPa per year. However field studies have observed a 4 hPa drift over 5 years for one unit. Ideally re-calibrations are performed every 2 to 3 years [*Stearns et al.,* 1993]. Re-calibrations may show up as jumps in the AWS pressure record.

The University of Wisconsin-Madison administers AWS activities for the United States Ant-

arctic Program, data is available via anonymous ftp from the university. The most readily available data format is the 10 minute time interval "raw" data, which is provided as is with little or no corrections to remove bad data. There is also a 3 hourly time interval data format which has been examined for bad data and corrected, however this format takes longer to process and at the time of this study was only available up to the end of 1997. We used the 10 minute data for 1998 and 1999, it was decimated to a 6 hourly time intervals to match the NCEP data. An initial examination of the data showed that station records vary in length and there are some gaps in the data, presumable due to temporary instrument failure. To ensure a sufficient amount of data for analysis, we only examined stations with an equivalent of 200 days of coincident NCEP and AWS data over 2 years. There were 38 stations that matched this criteria, their locations are shown in Figure 3.1. A complete record of all AWS and NCEP data used in this study may be found at http://www-gpsg.mit.edu/~katyq/plots_aws. The plots on this web site are in alphabetical order by station, absolute and differenced values of surface pressure and temperature are shown.

An initial comparison of AWS surface pressure values to NCEP estimates manifested 8 stations with obviously bad AWS data. The uncorrected data and differences are shown in Figure 3.4, sections of bad data are indicated by the dashed lines. Five station records, Elizabeth, Gill, Marilyn, Mount Siple, and Windless Bight, were repaired by removing the bad sections of data, these points were usually up to 40 hPa in error except for Gill which had a section of data over 200 hPa too low. Ferrell had the last few days of its record removed, it can be seen that the AWS pressure values have flat-lined. Two stations, Siple Dome and Butler Island, had obvious offsets in their records, linear fits were made to the offset segments and corrected for. Siple Dome's pressure measurement dropped by 16.5 hPa at day 389. Butler Island's pressure measurement had jumps of 15.8 hPa over the length of the record. The corrected records can be viewed at http://www-gpsg.mit.edu/~katyq/plots_aws.

Other stations show systematic errors that appear to be due to the AWS data rather than the NCEP data. For example, Bonaparte Point evidences a drift in the pressure differences that isn't seen in near by stations, such as Racer Rock (Figures 3.5j and 3.5k). This may be an example of the downward drift that some pressure transducers experience. One of the worst pressure comparisons is for Dome C II on the East Antarctic plateau (Figure 3.5b). There is an annual signal in the differences not seen in other plateau stations, e.g. Clean Air (Figure 3.5a), as well as 10 hPa jumps within the space of 6 hours, particularly in winter, that are not realistic. Another station with

greater than 10 hPa jumps between 6 hour points is Penguin Point (Figure 3.5g). The nearby station of D-10 does not show similar jumps (Figure 3.5e), implying that the AWS pressure data for Penguin Point might be in error. Such errors in AWS data cannot be easily fixed, these stations probably should not be used for ICESat validation.

3.4 Surface Pressure Comparisons

As stated in the previous section, this study covered two years of data for 1998 and 1999. Differences in surface pressure between NCEP estimates and AWS measurements were calculated every 6 hours where both values were available. Figure 3.1 shows the locations of the stations we used for validation. Table 3.1 is a summary of the surface pressure comparisons averaged over the entire 2 years. Based on previous studies, we have grouped stations according to regions with similar meteorological conditions. The mean offset in the differences is not a significant measure of NCEP error because we do not have sufficiently accurate values for the AWS unit elevations. There is an approximately 1 hPa change in pressure for every 10 m change in elevation. A mean value was subtracted from the differences before any further statistical calculations were performed, in order to account for this unknown elevation difference. The standard deviations, or rms errors, are more indicative of the true error. For all stations the rms error is less than 5 hPa, which is below the upper bound of 8 hPa set by the ICESat error budget. The last two columns in Table 3.1 are correlations of rms error in surface pressure to NCEP values of surface pressure and temperature. All starred correlation values are significant at the 95% level, which is true for the majority of stations. Rather than implying a direct link between pressure and temperature and rms error, this is probably an indirect measure of synoptic activity level, which is known to adversely effect the accuracy of the NCEP model.

Figure 3.6 shows the rms errors from Table 3.1 plotted on a map of Antarctica. As anticipated from previous studies, stations on the coast generally have higher rms error values. Dome C II on the East Antarctic plateau is an anomaly to this pattern, this is due to errors in AWS data. Bonaparte Point on the peninsula also has AWS data problems, as discussed in the previous section. Some of the differences in rms error between stations might be due to differing station elevations. Figure 3.7 shows the rms errors adjusted to a height of 3500 m, which is higher than any of the stations. The height adjustment is only a simple exponential function of pressure with

respect to height. This doesn't take into account the temperature lapse rate, and as such is useful for only a qualitative comparison. By correcting for different station heights some of the variability was accounted for. A good example of this is the reduction of rms variability between the West Antarctic stations. However, there is still a tendency for inland stations to have lower rms error values. In both Figure 3.6 and Figure 3.7 Mount Siple still has a relatively high rms error. It is difficult to say whether this is due to the AWS or NCEP values as there are no close by stations to corroborate. Mount Siple was one of the stations with bad sections of AWS data removed (Figure 3.4), there may still be problems with the pressure sensor in the segments of data retained. There is one peak in the differences around day 115, 1998, that appears to be due to the NCEP data not capturing an intense low pressure system (Figure 3.5f).

We expect stations that are close together in distance to have similar rms error values. A measure of this is the amount of correlation between pressure difference values plotted as a function of distance between stations (Figure 3.8). There is a definite correlation relationship with respect to distance. A 100 km moving average was applied to the correlation values. This average goes to zero around 1000 km, which is the length scale of most synoptic systems. This supports the idea that NCEP surface pressure error is related to synoptic activity level.

To better study any seasonal variations we calculated the rms error for surface pressure for 30 day segments (Figure 3.9). Before the rms differences were calculated, a 2 year mean of the differences was subtracted to account for any errors in station height. This correction for height bias may not be valid if any seasonal signal in the rms error is asymmetric. This is the case for Dome C II. As shown in Figure 3.5b, at the beginning of the Dome C II's record and around day 400 the two pressure time series seem to match relatively well. Yet in the monthly average plot these time periods show peaks in the monthly rms. This is because anomalous readings during the winter have thrown off the 2 year mean difference calculated and hence the monthly rms calculation. This asymmetry in the pressure difference time series is also evident for Bonaparte Point (Figure 3.5k), the drift in AWS pressure readings leads to anomalously high monthly rms values at each end of the time series. The correction for height bias also does not work if the segment of data available does not sufficiently sample at least one yearly cycle. This is the case for White Island (Figure 3.5d). The best pressure comparison is at the beginning of the time series yet the latter part of the record drags down the height bias calculation, leading to an incorrect estimate of monthly rms values. This may also be a problem for Mount Siple, where segments of data in the

summer have been removed due to AWS problems. The 2 year mean difference will tend to reflect the winter value. None of the other stations appear to have a problem with the height bias correction, we may be confident that the monthly rms values reflect the true error.

The monthly mean surface pressure rms errors are all below 5 hPa, except for those stations which have suspected AWS data problems. For most months and stations the rms errors are less than 3 hPa. The general spatial and seasonal patterns of rms errors follow the synoptic activity patterns known from Antarctic climatology. Inland stations on the plateau, the Ross Ice Shelf, and in the West Antarctic have generally lower rms values than the coastal, McMurdo area, and peninsula stations. The McMurdo area stations have an increased rms error in the winter of 1999. This reflects the increased synoptic activity level that can be seen in the time series plots for these stations, for example Pegasus South (Figure 3.5c). The south pole stations of Clean Air, Nico, and Henry show a peak around day 80, this corresponds to a long time scale drop in pressure that the NCEP model seems to lag behind (e.g. Clean Air, Figure 3.5a). This does not appear to be a result of increased synoptic activity and cannot be explained at this time.

3.5 Summary

The 2 year averages of rms surface pressure error are all less than 5 hPa, which corresponds to 12 mm of atmospheric delay error, well below the upper bound of 20 mm set by the ICESat science requirements. Only six stations have rms pressure errors of greater than 3 hPa, or 7 mm, they are Dome C II, Mount Siple, Bonaparte Point, Penguin Point, and White Island. We have good reason to believe that these AWS units have errors in their pressure measurements.

Monthly averages of the rms surface pressure differences reveal the spatial and seasonal patterns in the error. The rms error tends to increase with increasing level of synoptic activity. Antarctic climatology tells us that synoptic activity is generally greater on the coast as the steep topography of the continent edges acts as a barrier southward penetration of storms. Activity level also increases in the winter. The monthly rms plots for 1998 and 1999 shown in Figure 3.9 follow these trends, although is can be seen from just these two years of data that activity level can vary from year to year. The winter storms of 1999 were much more intense than 1998. In general, the upper bound on rms surface pressure error over the majority of the continent is estimated at 3 hPa, corresponding to 7 mm of atmospheric delay.

References

Bromwich, D. H., R. I. Cullather, and R. W. Grumbine, An assessment of the NCEP operational global spectral model forecasts and analyses for Antarctica during FROST, *Weather Forecast., 14,* 835-850, 1999.

Cullather R. I., D. H. Bromwich, and R. W. Grumbine, Validation of operational analyses in Antarctic latitudes, *J. Geophys. Res., 102,* 13,761-13,784, 1997.

Drewry, D. J., The surface of the Antarctic ice sheet. *Antarctica: Glaciological and Geophysical Folio,* Scott Polar Research Institute, Cambridge, UK, 1983.

GLAS Science Team, Geoscience Laser Altimeter System (GLAS) Science Requirements Document, Version 2.01, 1997.

King, J. C., and J. Turner, Antarctic Meteorology and Climatology, Cambridge Uni. Press, Cambridge, UK, 1997.

Parish, T. R., and D. H. Bromwich, On the forcing of seasonal changes in surface pressure over Antarctica, *J. Geophys. Res, 102,* 13,785-12,792, 1997.

Radok, U., I. Allison, and G. Wendler, Atmospheric surface pressure over the interior of Antarctica, *Antarct. Sci., 8,* 209-217, 1996.

Stearns, C. R., and G. Wendler, Research results from Antarctic automatic weather stations, *Rev. Geophys., 26,* 45-61, 1988.

Stearns, C. R., L. M. Keller, G. A. Weidner, and M. Sievers, Monthly mean climatic data for Antarctic automatic weather stations, *in Antarctic Meteorology and Climatology: Studies Based on Automatic Weather Stations, Antarctic Res. Ser., vol. 61,* edited by D. H. Bromwich and C. R. Stearns, 1-21, 1993.

Trenberth, K. E., and J. G. Olsen, An evaluation and intercomparison of global analyses from NMC and ECMWF, *Bull. Am. Meteorol. Soc., 69,* 1047-1057, 1988.

Turner, J., et al., The Antarctic First Regional Observing Study of the Troposphere (FROST) Project, *Bull. Am. Meteorol. Soc., 77,* 2007-2032, 1996.

Table 3.1. Statistics of Surface Pressure Differences (NCEP - AWS), averaged over 2 years

Station	Lat (°N)	Lng (°S)	Elev (m)	No. Points	Sdev (hPa)	Mean (hPa)	Corr. with P	Corr. with T
			Plateau					
Clean Air	-90.00	0.00	2835	1961	1.34	1.52	0.07*	0.06*
Nico	-89.00	89.67	2935	2149	1.24	1.68	-0.08*	-0.11*
Henry	-89.01	-1.03	2755	1933	1.35	-0.52	-0.10*	-0.29*
Dome C II	-75.12	123.37	3250	2047	4.32	-5.46	0.37*	0.39*
Relay Station	-74.02	43.06	3353	2088	2.08	-0.35	0.16*	-0.03
			Coastal					
Mount Siple	-73.20	-127.05	230	1397	4.79	0.41	-0.31*	0.00
Scott Island	-67.37	-179.97	30	1074	1.78	0.76	-0.11*	0.03
Possession Island	-71.89	171.21	30	1748	3.31	6.74	0.06*	-0.03
Manuela	-74.95	163.69	80	2137	2.68	2.44	-0.03	-0.36*
Penguin Point	-67.62	146.18	30	894	3.81	3.69	0.37*	0.08*
D-10	-66.71	139.83	243	1112	2.36	4.81	0.24*	-0.09*
			McMurdo Area					
Ferrell	-77.92	170.82	45	801	1.43	-1.09	-0.04	-0.18*
White Island	-78.09	168.01	30	952	3.51	-2.27	-0.07*	0.72*
Linda	-78.48	168.38	50	1998	1.69	17.20	-0.05*	-0.13*
Minna Bluff	-78.55	166.66	920	2049	2.56	-2.54	-0.13*	0.50*
Pegasus South	-77.99	166.58	10	1927	2.15	-3.55	-0.10*	0.22*
Willie Field	-77.87	167.02	20	1533	2.28	-1.79	-0.01	-0.16*
Windless Bight	-77.73	167.70	61	1058	2.83	-7.74	-0.07*	0.27*
Marble Point	-77.44	163.75	114	1467	1.82	0.10	-0.01	0.08*
			Ross Ice Shelf					
Marilyn	-79.95	165.13	75	2169	1.62	-1.54	0.03	-0.06*
Schwerdtfeger	-79.90	169.97	60	2132	1.54	0.47	-0.08*	-0.07*
Elaine	-83.13	174.17	60	2128	1.58	-4.48	-0.06*	0.03
Lettau	-82.52	-174.45	55	1365	1.01	-2.38	0.00	-0.07*
Gill	-79.99	-178.61	55	2055	1.82	-5.89	-0.07*	0.04
			West Antarctic					
Theresa	-84.60	-115.81	1463	2170	0.99	-0.83	0.01	-0.30*
Doug	-82.32	-113.24	1433	873	0.96	5.84	-0.08*	-0.07*
Byrd	-80.01	-119.40	1530	1663	1.27	-4.41	-0.18*	-0.11*
Erin	-84.90	-128.81	1006	1623	1.59	-9.65	0.22*	-0.01
Harry	-83.00	-121.39	945	1020	1.34	2.17	-0.01	-0.23*
Swithinbank	-81.20	-126.17	945	2146	1.63	2.01	-0.06*	-0.27*
Elizabeth	-82.61	-137.08	549	1757	1.04	-1.87	0.05*	-0.15*
Siple Dome	-81.66	-148.77	620	2093	2.00	7.23	0.10*	-0.18*

Station	Lat (°N)	Lng (°S)	Elev (m)	No. Points	Sdev (hPa)	Mean (hPa)	Corr. with P	Corr. with T
			Peninsula					
Racer Rock	-64.07	-61.61	17	1418	2.39	-1.35	0.01	-0.56*
Larsen Ice Shelf	-66.95	-60.91	17	1538	2.58	1.00	0.37*	0.23*
Bonaparte Point	-64.78	-64.07	8	1438	3.91	11.58	-0.12*	-0.07*
Santa Claus Island	-64.96	-65.67	25	939	2.11	0.47	-0.06*	-0.23*
Butler Island	-72.21	-60.17	91	1900	2.46	0.37	-0.05*	0.06*
Limbert	-75.42	-59.95	40	1175	1.25	-4.30	0.02	-0.12*

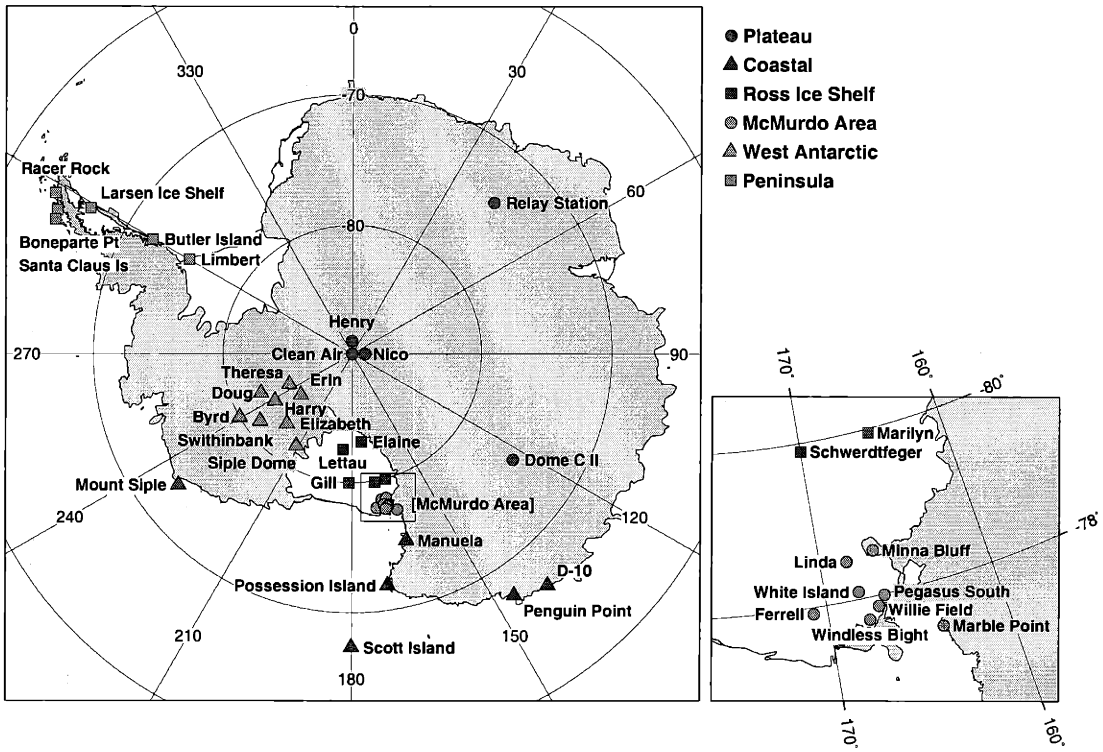

Figure 3.1. Location map for Antarctic Automatic Weather Stations. Stations are grouped according to regions with similar meteorological conditions.

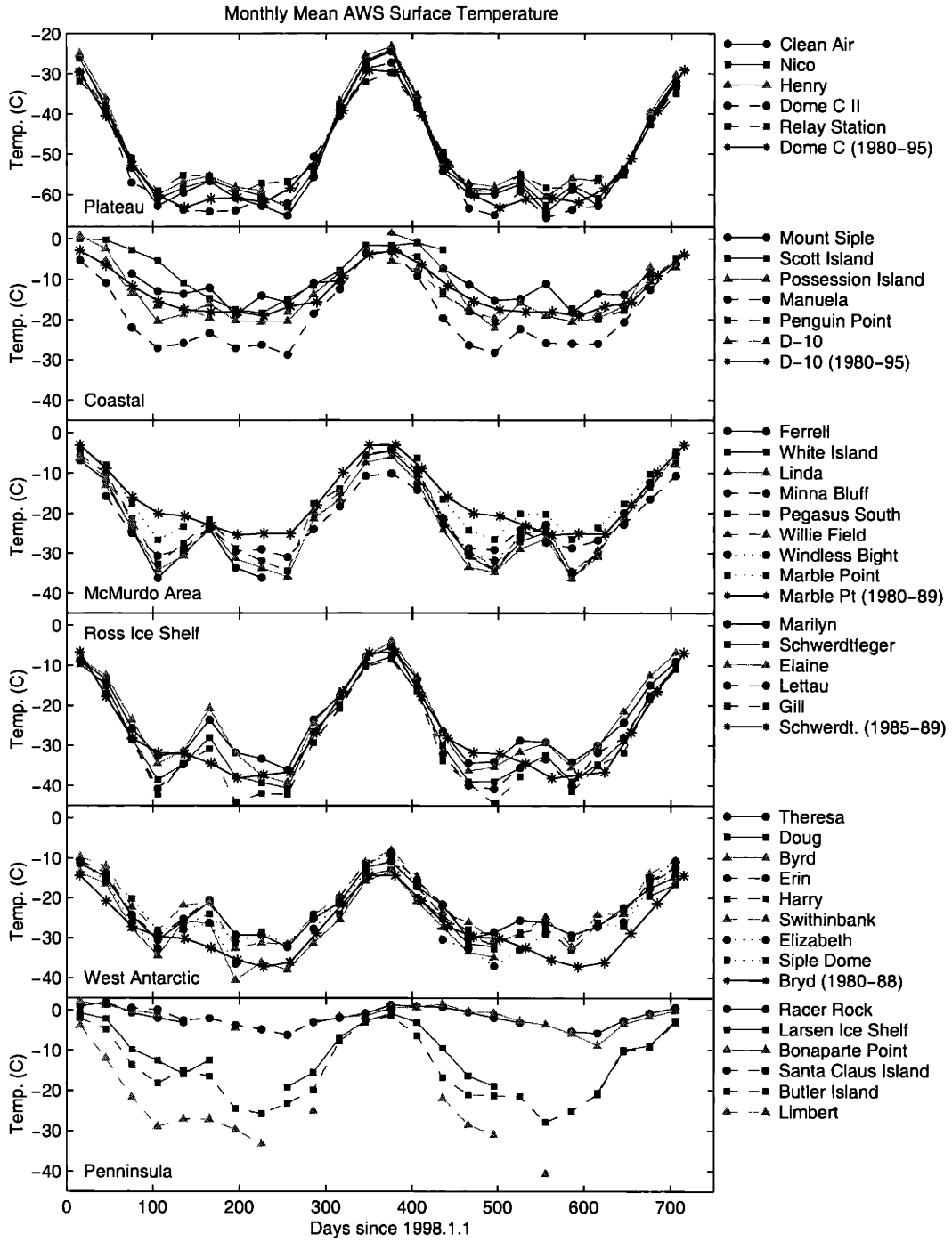

Figure 3.2. Monthly mean AWS surface temperatures, grouped according to meteorological region. Each region has an example of mean monthly climatology, except for the Peninsula region which does not have long term station data available.

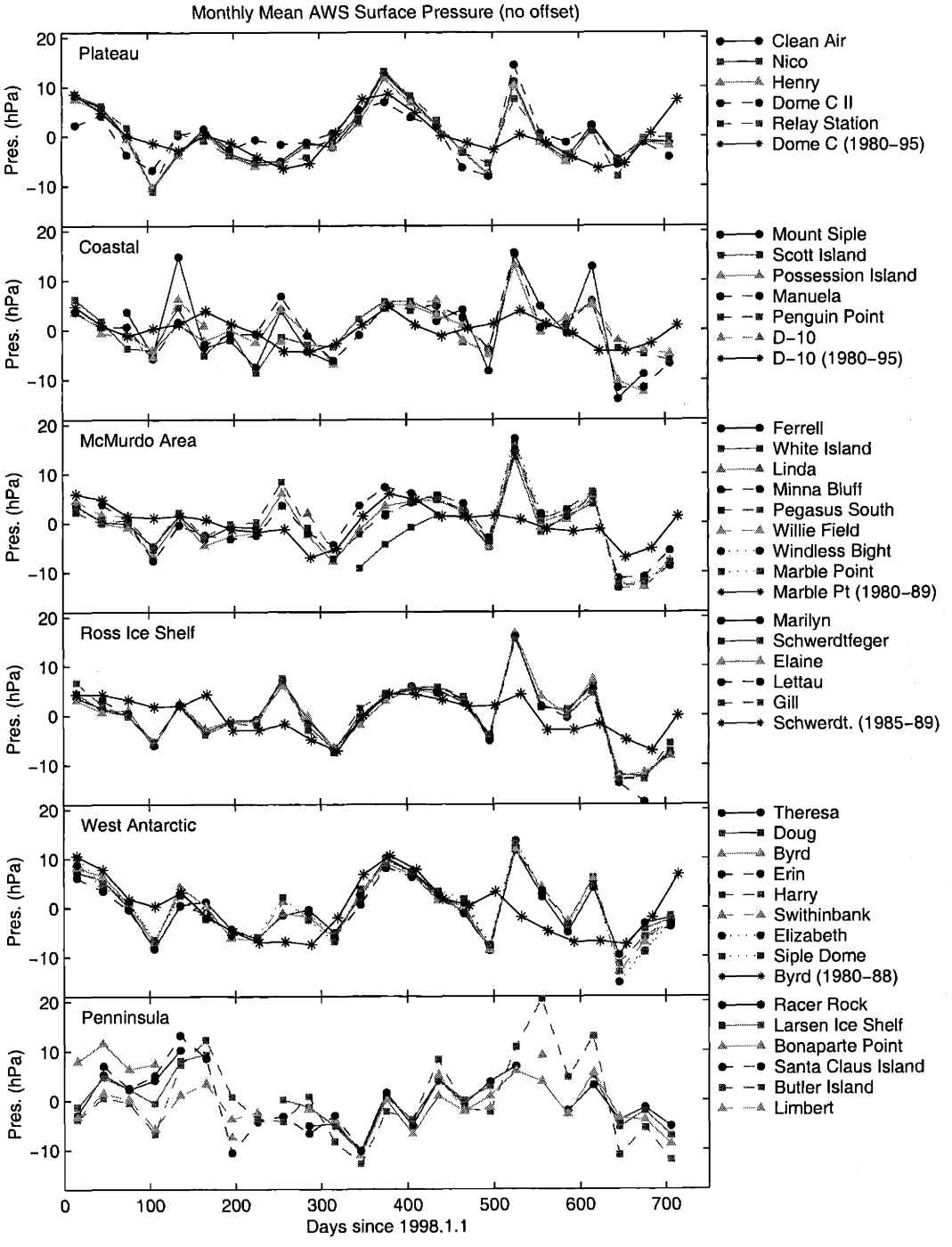

Figure 3.3. Monthly mean AWS surface pressures, grouped according to meteorological region. There has been a mean annual pressure subtracted from each station's monthly mean values. Each region has an example of mean monthly climatology, except for the Peninsula region which does not have long term station data available.

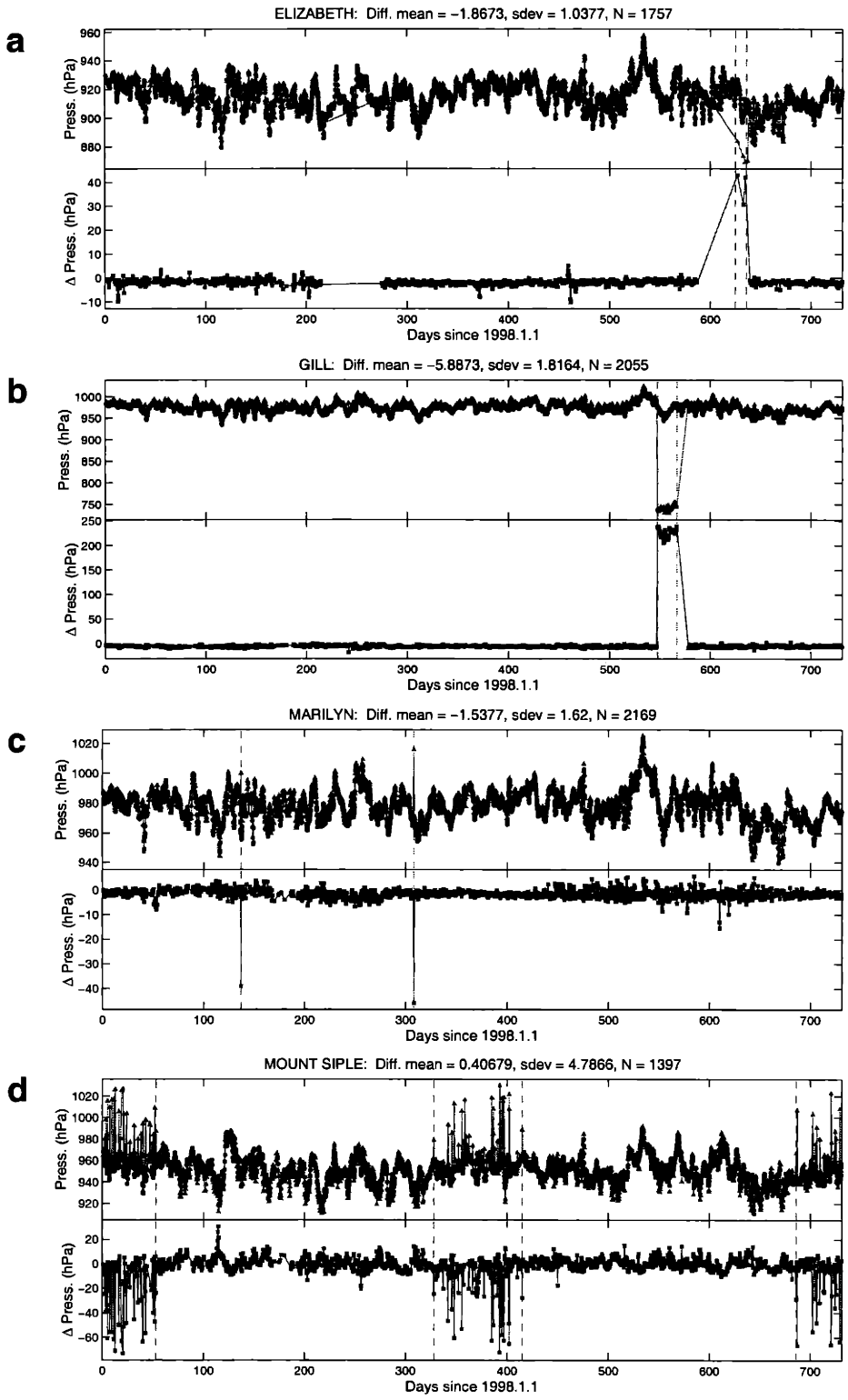

Figure 3.4 a-d. Time series data for stations with bad AWS surface pressure data. Upper plot for each station shows NCEP surface pressure values (squares) and AWS values (triangles). Lower plot is surface pressure differences, NCEP minus AWS. Note that the vertical scales are different for each station.

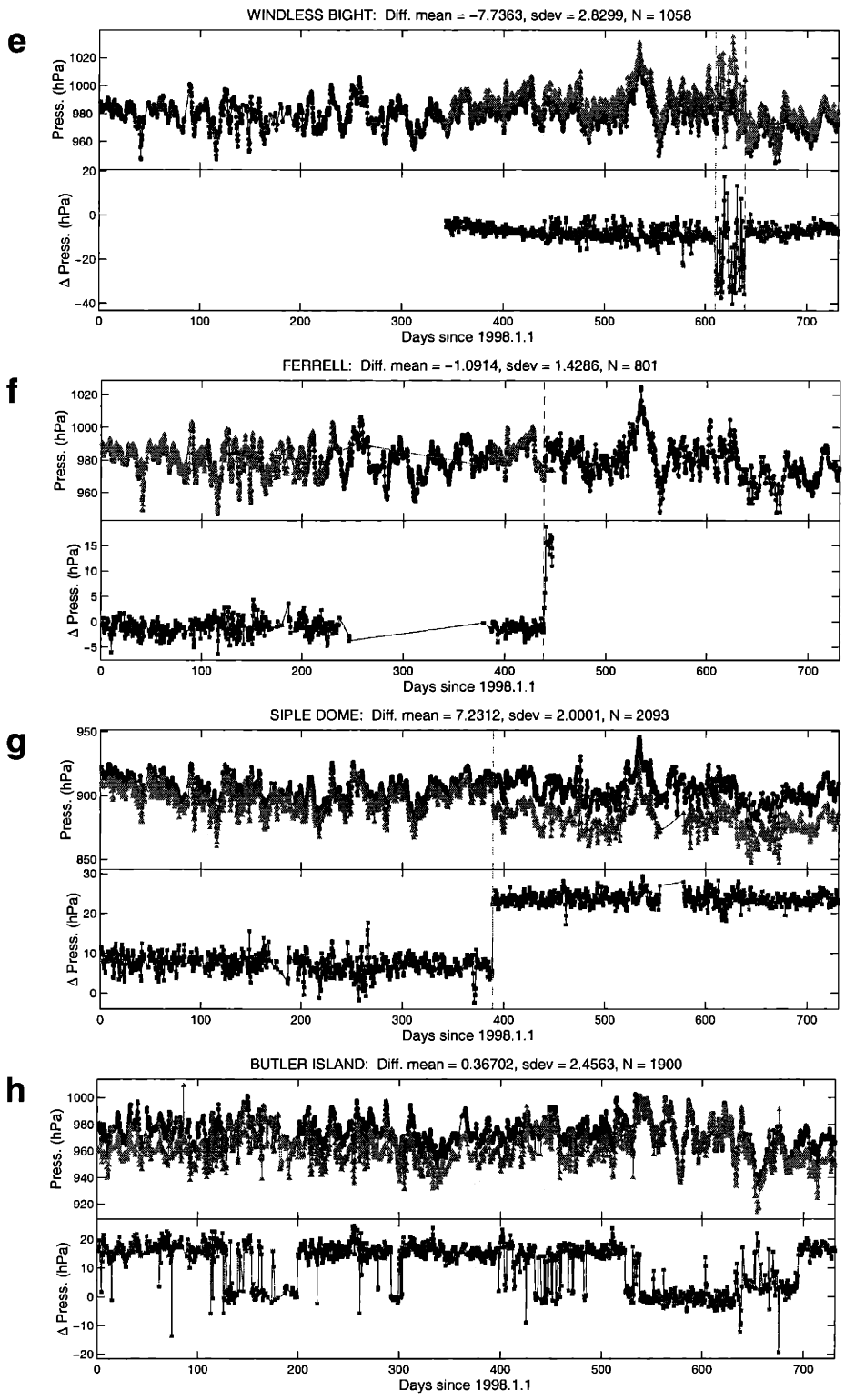

Figure 3.4e-h. Time series data for stations with bad AWS surface pressure data. Upper plot for each station shows NCEP surface pressure values (squares) and AWS values (triangles). Lower plot is surface pressure differences, NCEP minus AWS. Note that the vertical scales are different for each station.

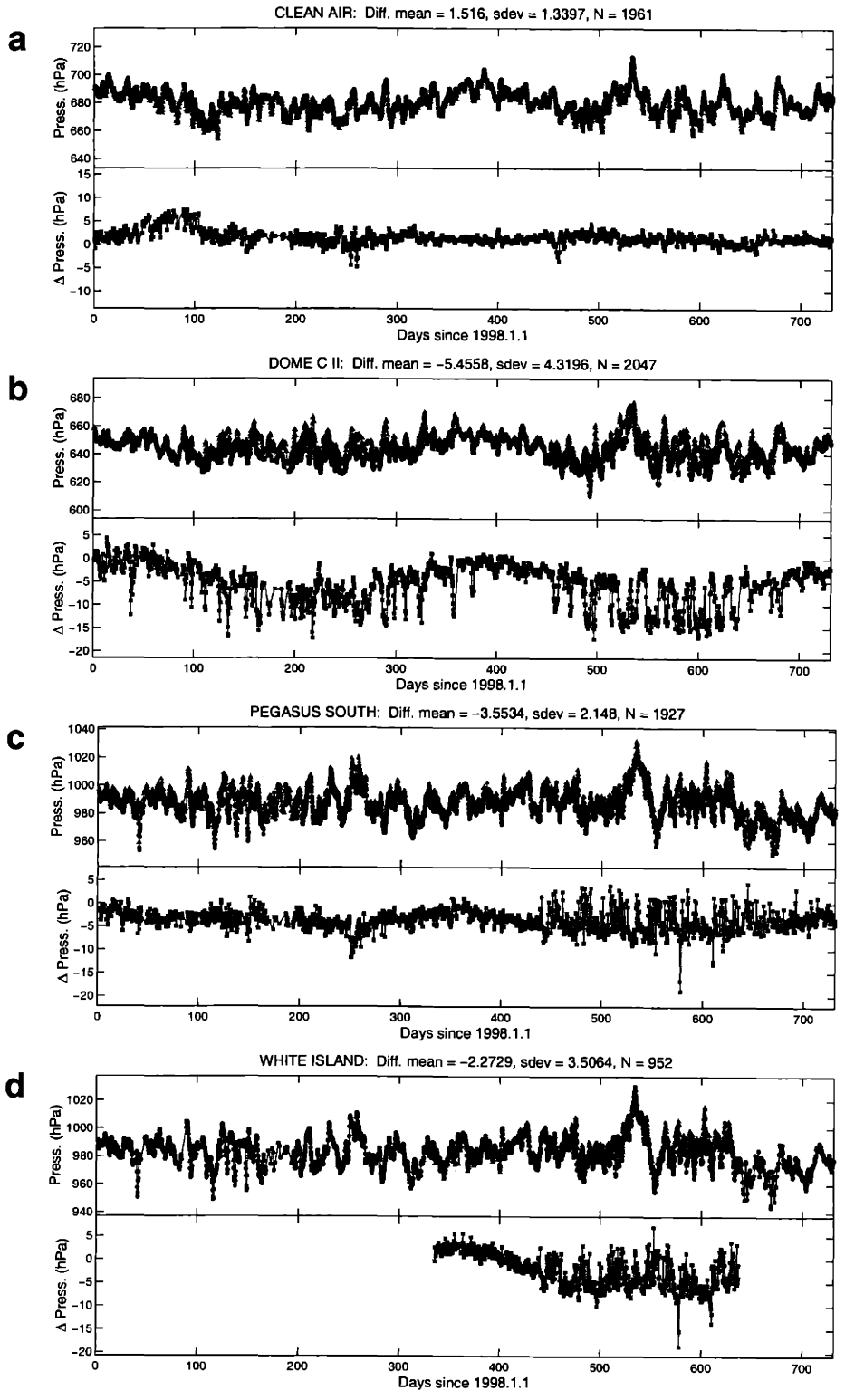

Figure 3.5a-d. Time series data for selected stations. Upper plot for each station shows NCEP surface pressure values (squares) and AWS values (triangles). Lower plot is surface pressure differences, NCEP minus AWS. Note that the vertical scale range is the same for each station, although the offsets are different.

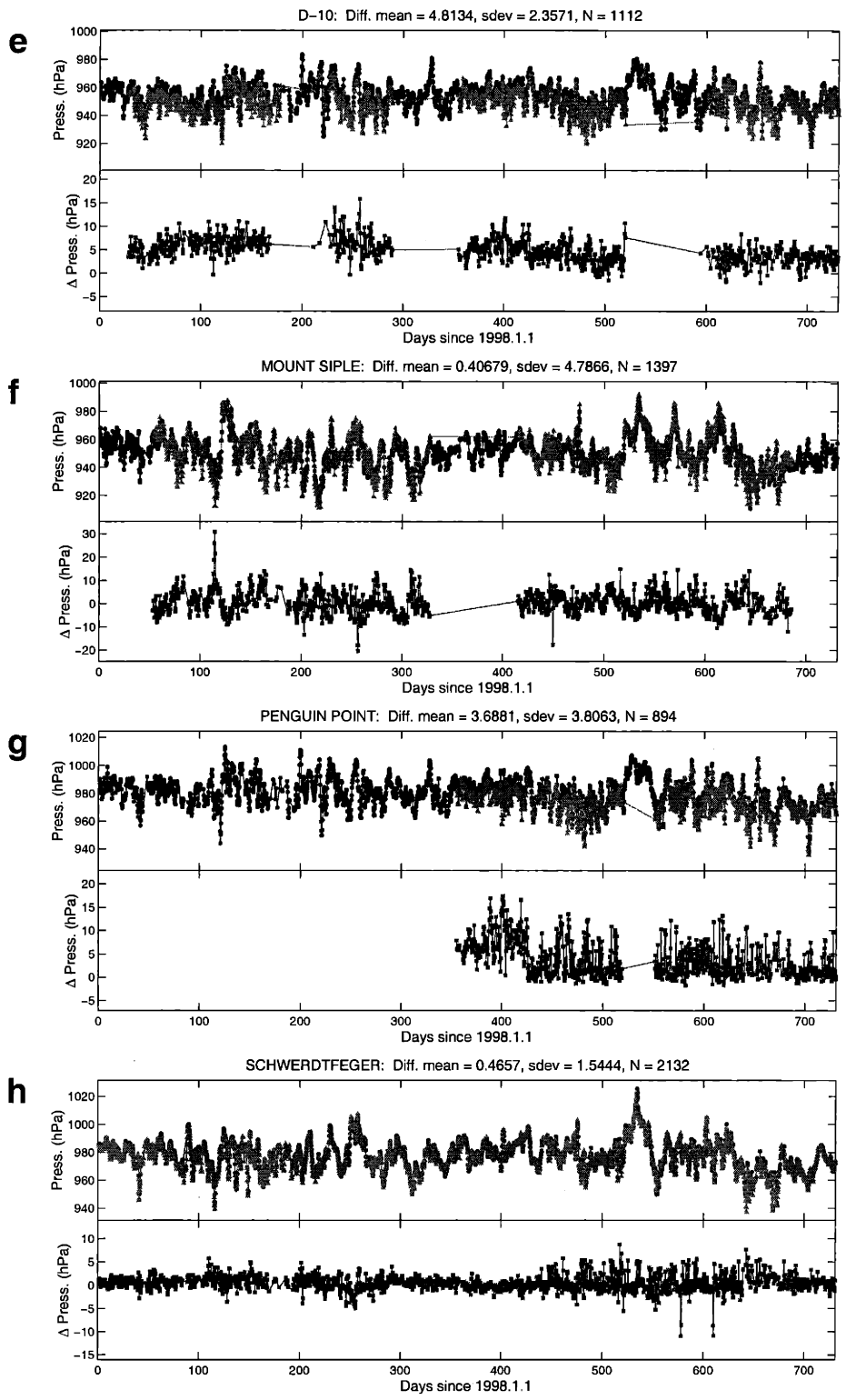

Figure 3.5e-h. Time series data for selected stations. Upper plot for each station shows NCEP surface pressure values (squares) and AWS values (triangles). Lower plot is surface pressure differences, NCEP minus AWS. Note that the vertical scale range is the same for each station, although the offsets are different.

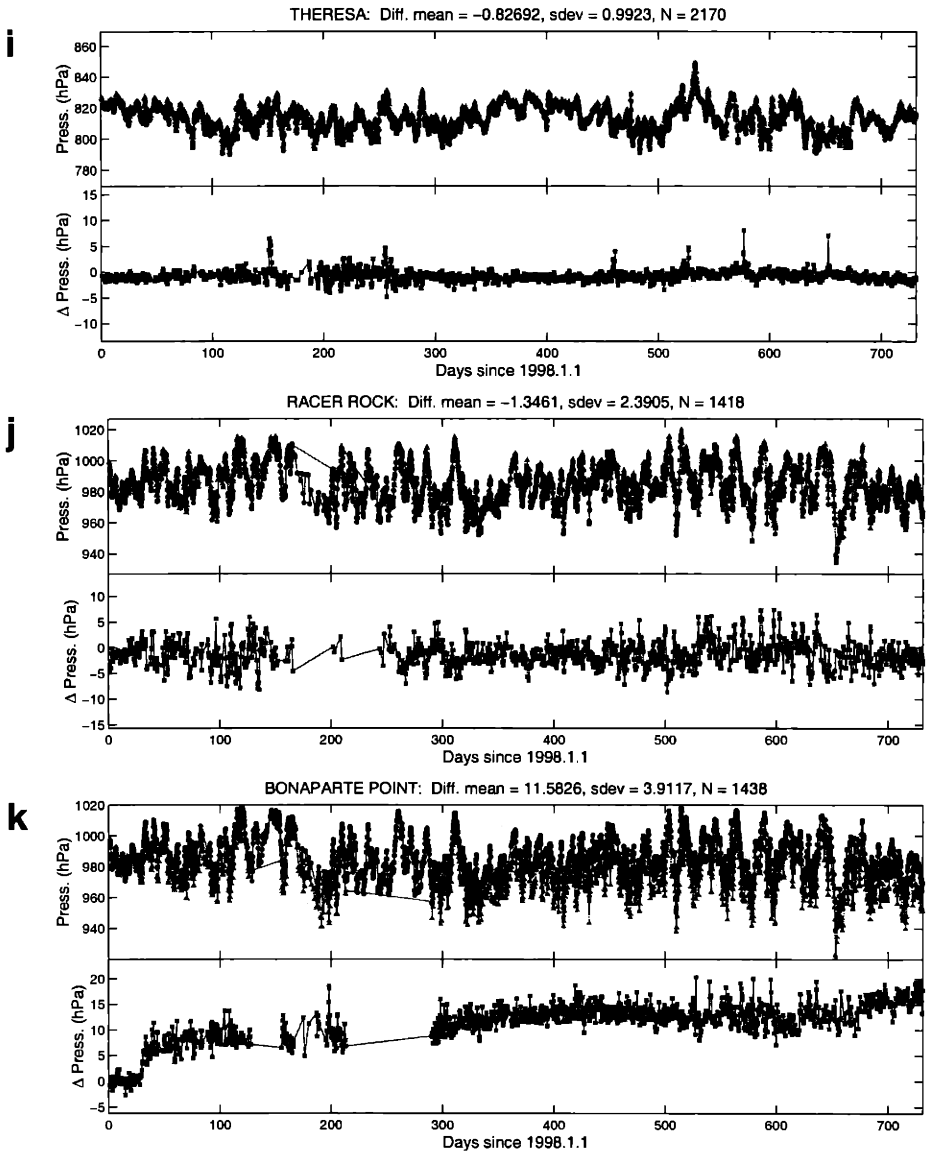

Figure 3.5i-k. Time series data for selected stations. Upper plot for each station shows NCEP surface pressure values (squares) and AWS values (triangles). Lower plot is surface pressure differences, NCEP minus AWS. Note that the vertical scale range is the same for each station, although the offsets are different.

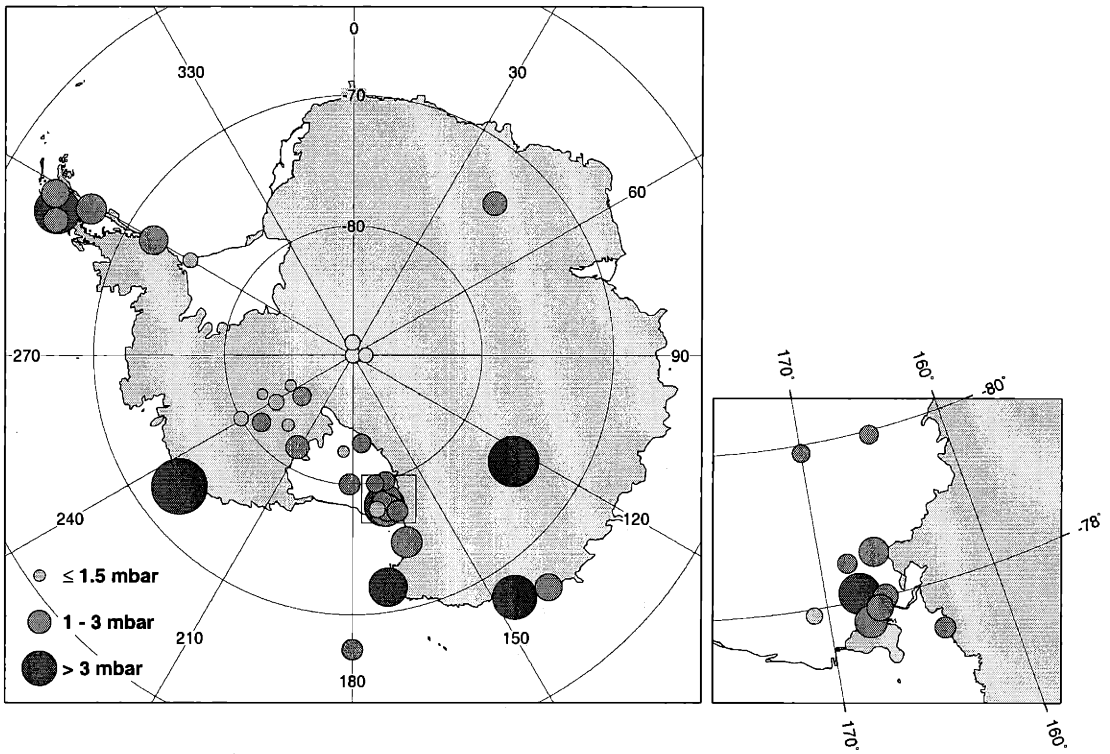

Figure 3.6. RMS suface pressure differences, averaged over 2 years (1998 - 99). Diameter of circle is directly proportional to rms value. For each station, the mean value of the differences was subtracted before the rms difference was calculated.

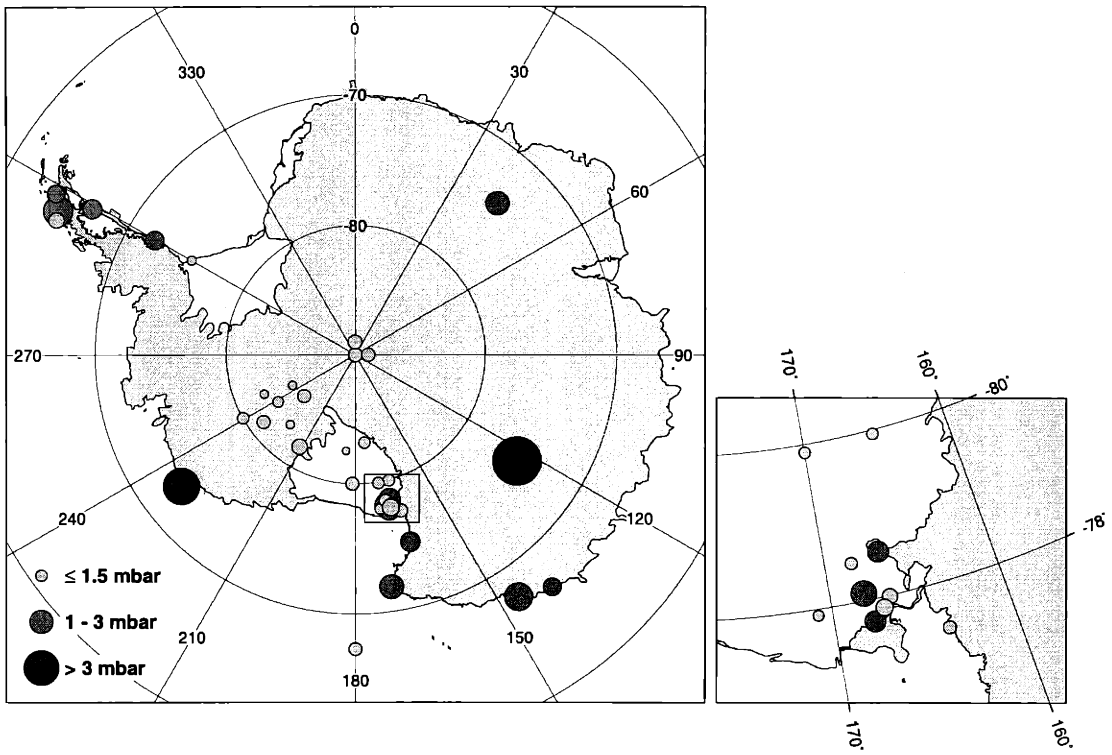

Figure 3.7. RMS suface pressure differences adjusted to a common height of 3500 meters, averaged over 2 years (1998 - 99). Diameter of circle is directly proportional to rms value. For each station, the mean value of the differences was subtracted before the rms difference was calculated.

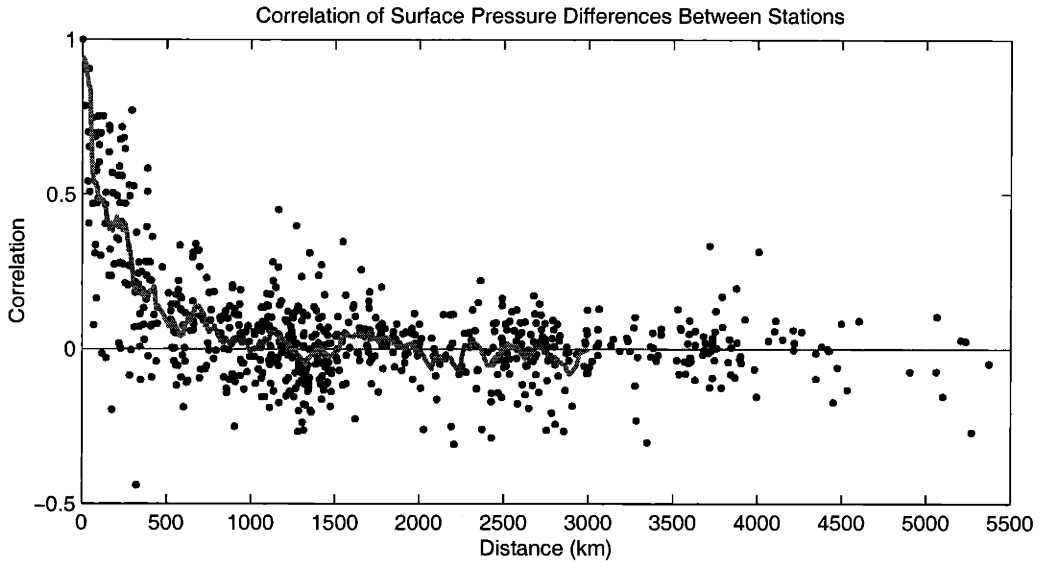

Figure 3.8. Correlation of surface pressure differences between stations versus distance between stations. Line is 100 km moving average of correlations.

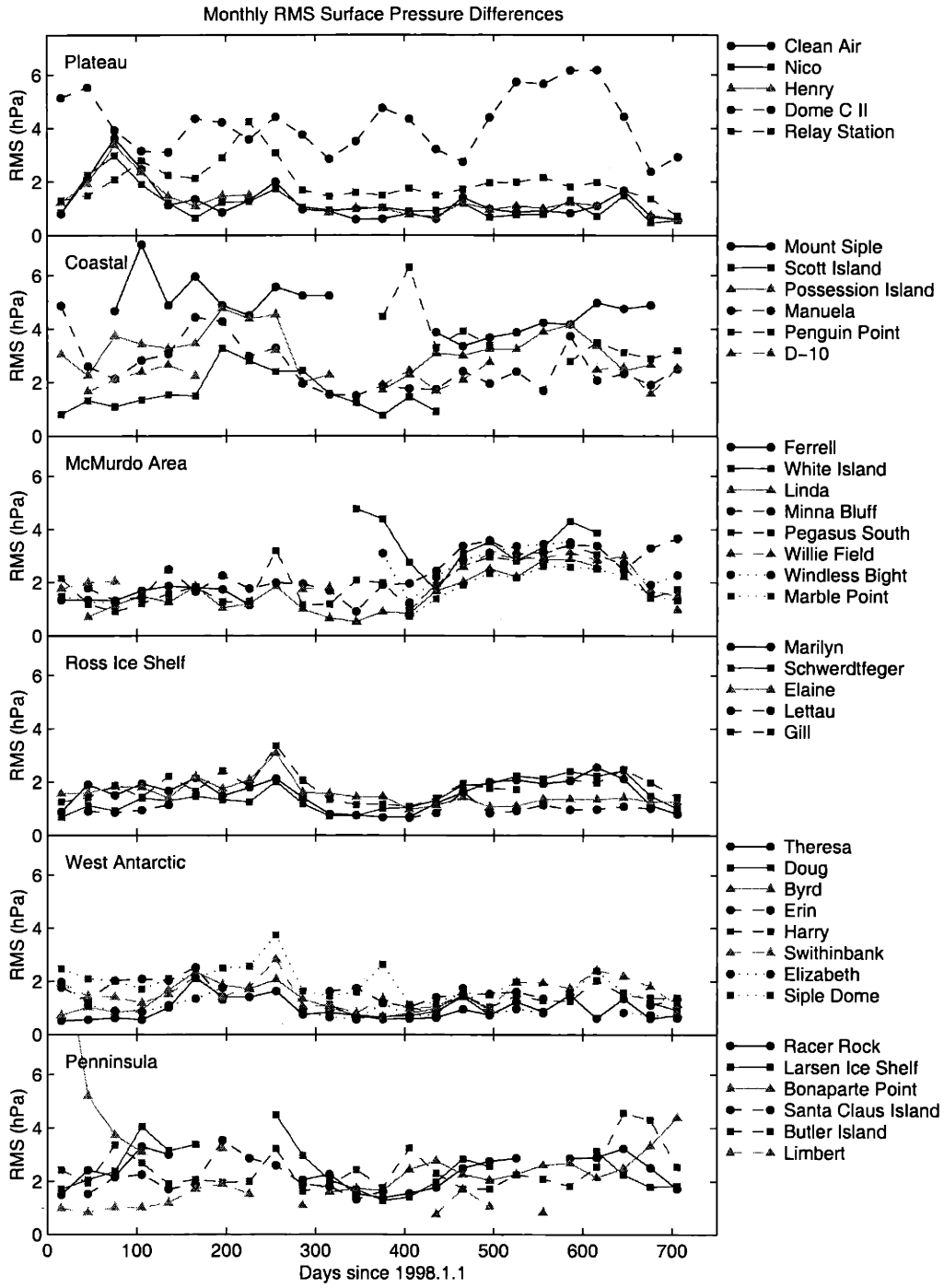

Figure 3.9. Monthly rms surface pressure differences, grouped according to meteorological region. For each station the mean value of the differences, calculated of the entire 2 year record, was subtracted before the rms difference for each month was calculated.

Chapter 4

Estimating Precipitable Water Vapor using GPS Tropospheric Delays and Numerical Weather Model Data and the Implications for ICESat Delay Validation

4.1 Introduction

Water vapor is the most significant atmospheric component in terms of its effect on the intensity and variability of the weather. The latent heat energy that is exchanged through condensation and evaporation drives the global weather patterns [*Chahine*, 1992]. Water vapor is unevenly distributed in the atmosphere, both horizontally and vertically, and varies on timescales from seconds to decades. Although water vapor is such an important atmospheric component, it tends to be poorly determined in numerical weather models, precisely because it is so variable.

Any new source of data that could improve our knowledge of water vapor distribution would be valuable, this has been one of the goals of GPS meteorology. As GPS signals propagate through the atmosphere they are refracted, which introduces a delay into the travel time. A large part of the refractivity depends on the water vapor amount along the signal ray path, making GPS delay estimates a valuable tool for sensing atmospheric water vapor.

When processing GPS data this delay must be estimated and accounted for. The common method for estimation is to parameterize the atmospheric delay and model it as a stochastic process. The parameters are then solved for in the overall geodetic solution [*Herring et al,* 1990; *Tralli et al,* 1992]. Total delay in the zenith direction is typically of the order of 2.3 m, with the component that depends on water vapor contributing 0 to 35 cm. For ray paths off vertical the signal travels through more of the atmosphere and is therefore experiences more delay. Converting from total path delays to zenith delays is commonly performed using a mapping function. These mapping functions are an important element of the GPS processing. This method produces estimates of GPS zenith delay that are accurate to within 6-10 mm [*Rocken et al*, 1995; *Gendt,* 1996], depending on the GPS network size.

Another method of estimating GPS delay is to directly use atmospheric data. Refractivity of the atmosphere at GPS wavelengths is a function of pressure, temperature, and amount of water vapor [*Thayer,* 1974]. To calculate zenith delay the refractivity equation is integrated through the atmospheric column. Total zenith delay may then be expressed as a function of surface pressure, total precipitable water vapor, and mean temperature of the atmospheric column [*Saastamoinen,* 1972; *Davis et al.,* 1985]. Values for these atmospheric variables may be obtained from numerical weather models or in-situ meteorological measurements. The basic zenith delay equation has two terms. The first term, called the hydrostatic delay, is proportional to surface pressure such that 1 hPa corresponds to approximately 2.3 mm of delay. The second term, called the "wet" delay, is approximately proportional to precipitable water vapor (PW) such that 1 mm PW corresponds to approximately 6 mm of delay. For ray paths at an angle to zenith, the delay equation is modified by a mapping function that primarily depends on elevation angle and sometimes climatological parameters, depending on the form of mapping function used [*Davis et al.,* 1985; *Niell,* 1996]. All delays described in this paper are expressed as zenith delays. Precipitable water vapor is typically the least accurately known variable in this method of estimating GPS delay. Given sufficiently accurate values of surface pressure and mean temperature, the errors in numerical weather model derived GPS delay are proportional to the errors in precipitable water vapor.

Combining the delay estimate derived from GPS processing and atmospheric data has become a popular method for calculating precipitable water vapor [*Bevis et al,* 1992, 1994; *Rocken et al,* 1993, 1995; *Duan et al,* 1996; *Businger et al,* 1996; *Niell et al,* 2001]. If surface pressure is known to within 0.5 hPa and mean temperature to within 2%, then precipitable water vapor can be estimated by subtracting the hydrostatic component of delay, as calculated using direct surface pressure measurements, from the total stochastic GPS delay. Precipitable water vapor can be estimated to within 1 mm using this GPS meteorology technique. This level of agreement has been validated by comparisons to water vapor radiometer measurements [*Rocken et al,* 1995]. These derived estimates for precipitable water vapor can be a valuable addition to numerical weather models [*Smith et al,* 2000; *Ware et al,* 2001], or the delays can be directly assimilated into the numerical weather models as a way of improving the forecasts, studies have shown that direct assimilation of GPS delays do indeed improve the forecasts [*Kuo et al,* 1993; *Zou et al,* 1995; *Elgered,* 2001].

The comparison of GPS precipitable water vapor estimate and the numerical weather model

estimate provides valuable information about both methods. These weather models are attractive because they provide an internally consistent, readily available global data set. However, they have higher errors than in-situ meteorological measurements, and we need to quantify these errors. Precipitable water vapor is the most difficult atmospheric variable to model, knowing the errors in precipitable water vapor is important for evaluating numerical weather models. Knowing the errors in precipitable water vapor is also important for evaluating the errors in the ICESat atmospheric delay model, as described in Chapter 2. The purpose of this study is to investigate the comparison between GPS derived PW and the NCEP numerical weather model values, with the goal of quantifying the errors and then applying this knowledge to validate the ICESat atmospheric delay estimates. Hopefully the results will also indicate areas for improvement in both the GPS and NCEP modeling.

We have three basically independent data sources available. The numerical weather model data, the GPS ground station data, and the in-situ meteorological units situated at a certain small subset of the GPS stations. The numerical weather model data used are the National Center for Environmental Prediction (NCEP) global analyses. The NCEP data and GPS station location information are used to calculate surface pressure, precipitable water vapor, and mean temperature. The GPS ground station data are used in GPS data processing to estimate total atmospheric delay. The meteorological units at a subset of the GPS stations provide direct measurements of surface pressure, denoted as MET surface pressure. Using this and the GPS delay values we can derive a value for precipitable water vapor that may be compared to the NCEP value. This calculation can also be performed using NCEP surface pressure values instead of MET surface pressure.

The next section summarizes the equations used for calculating GPS delay and it's relationship to surface pressure and precipitable water vapor. Section 3 discusses the data sets we are using, Section 4.1 briefly describes the GPS data and the processing used to calculate delay, Section 4.2 introduces the NCEP numerical weather model, Section 4.3 describes the calculation of NCEP surface pressure and shows the results of comparisons to in-situ MET measurements, and Section 4.4 discusses the calculation of NCEP precipitable water vapor. Section 4 shows the results of our precipitable water vapor comparisons, examining the spatial and temporal variations. We also look at the comparison of NCEP delay estimates and GPS delays. Of particular interest are the comparisons where the precipitable water vapor value is low since this will help

validate ICESat optical delay estimates.

4.2 Theory

The signal from a GPS satellite will be refracted as it travels through the atmosphere to receivers on the ground. The delay due to this refraction is the difference between the integral of the index of refraction along the signal path and the path if the signal were traveling through vacuum:

$$D = \int_{atm} n(s)ds - \int_{vac} ds \tag{4.1}$$

If the atmosphere is assumed to be azimuthally symmetric about the receiver then this equation may be simplified to a zenith delay modified by a mapping function. This mapping function depends on the elevation angle between the GPS satellite and ground receiver such that [*Davis, et al.,* 1985]

$$D = m(\varepsilon)\int_{Z}^{\infty}(n(z) - 1)dz \tag{4.2}$$

where $m(\varepsilon)$ is a mapping function, ε is the elevation angle, Z is the height of the receiver. The integral in Equation 4.2 is now the zenith delay.

There are different forms of the mapping function depending on what assumptions and simplifications to the structure of the atmosphere are made. Assuming the atmosphere is azimuthally and spherically symmetric, the mapping function may be approximated by a continued fraction form [*Marini,* 1972]:

$$m(\varepsilon) = \cfrac{1}{\sin\varepsilon + \cfrac{a}{\sin\varepsilon + \cfrac{b}{\sin\varepsilon + \cfrac{c}{\sin\varepsilon + \ldots}}}} \tag{4.3}$$

The parameters in the mapping function are estimated by comparing models to ray tracing solutions using climatic data. These parameters may depend on surface meteorology, averaged climatologies, location, or time of year. As of the beginning of 2002, 6 of the 7 Analysis Centers of the International GPS Service (IGS), including Scripps, were using the Niell [1996] mapping function, one was using Saastamoinen's [1972] formulation. The Niell mapping function depends

on latitude, height above sea level, and day of year. Niell [1996] provides an extensive overview and comparison of atmospheric delay mapping functions. This chapter does not require the explicit use of mapping functions as we are concerned with zenith delays, however the mapping functions are an implicit element of the GPS estimates of delay.

In Equation 4.2, the argument of the integral is normally given as refractivity, i.e. $(n - 1) = 10^{-6}N$. The formula for refractivity of air at radio values from Thayer [1974] is

$$N = k_1 \frac{P_d}{T} Z_d^{-1} + k_2 \frac{P_w}{T} Z_w^{-1} + k_3 \frac{P_w}{T^2} Z_w^{-1} \tag{4.4}$$

where N is refractivity, P_d and P_w are the partial pressures of dry-air and water vapor, T is temperature, and Z_d and Z_w are the compressibilities of dry-air and water vapor, and k_1, k_2, and k_3 are empirically determined constants. The compressibility factors account for non-ideal gas behavior. The first two terms of Equation 4.4 are due to the induced dipole moments of the dry air components and water molecules, respectively. The third term is due to the permanent dipole moment of the water molecule, which none of the dry air components possesses. Note that the optical refractivity formula, as given in Chapter 2, Equation 2.4a, does not have this third term because optical frequencies are not in the range of natural resonances of the water molecule. This third term in the refractivity formula at radio frequencies is the primarily the reason why GPS delay values are much more sensitive to water vapor than optical laser altimetry delay values.

The values for the refractivity constants have been subject to some debate. Thayer's values for k_2 and k_3 are considered unreliable because the extrapolation of k_2 from optical wavelengths ignores infrared resonances [*Hill et al,* 1982]. Direct measurements made at radio frequencies have been used to determine these constants, Smith and Weintraub [1953] calculated averaged values from a compilation of experimental values. Hasagawa and Stokesbury [1975] recalculated averaged values for a wider range of direct measurements. Bevis et al [1994] took the same list of experimental results that Hasagawa and Stokesbury used and performed a more considered statistical analysis, rejecting outliers and adopting more conservative standard errors. The Bevis values for the refractivity constants appear to be the most robust and will be used in this chapter, they are $k_1 = 77.60 \pm 0.05$ K hPa^{-1}, $k_2 = 70.4 \pm 2.2$ K hPa^{-1}, and $k_3 = (3.739 \pm 0.012)\ 10^5$ K^2 hPa^{-1}.

Using Thayer's [1974] formula for refractivity, Davis et al [1985] performed a detailed derivation of zenith delay formulas, the following is primarily based on these formulas with some

updates of empirical parameters. The total delay may be partitioned into a hydrostatic component that is proportional to surface pressure and a non-hydrostatic, or "wet", component that is proportional to precipitable water vapor. The refractivity may be restated as

$$N = k_1 \frac{R}{M_d} \rho + \left(\frac{k'_2}{T} + \frac{k_3}{T^2} \right) P_w Z_w^{-1} \tag{4.5}$$

where ρ is the total density and $k'_2 = k_2 - k_1 M_w / M_d$. M_w/M_d is the ratio of the molecular weight of water vapor and dry air, based on Bevis et al [1994] $k'_2 = 22.1 \pm 2.2$ K hPa^{-1}. Integrating the first term of Equation 4.5 by assuming hydrostatic equilibrium gives the hydrostatic component of zenith delay as

$$ZHD = 10^{-6} k_1 \frac{R}{M_d} g_m^{-1} P_S \tag{4.6}$$

where P_S denotes surface pressure, g_m is the mean value of gravity in the column of the atmosphere, the universal gas constant, R, is 8314.510 J/kmol.K, the dry-air molecular weight, M_d, is 28.9632 kg.kmol^{-1} [*Ciddor,* 1996], and k_1 is 0.7760 K/Pa [*Bevis et al,* 1994]. Since gravity decreases slowly with height and can be closely approximated as a simple function of latitude, the mean gravity can be expressed accurately in terms of the height, Z, and latitude, ϕ, of the ground point to which the altimeter measurement is made [*Saastamoinen,* 1972]

$$g_m = 9.8062(1 - 0.00265\cos(2\phi) - 3.1\times10^{-7}(0.9Z + 7300)) \text{ ms}^{-2} \pm 0.001 \text{ ms}^{-2} \tag{4.7}$$

The remaining two terms of Equation 4.5 may be integrated through the atmospheric column to give the wet component of zenith delay such that

$$ZWD = 10^{-6} \frac{R}{M_w} (k_2' + k_3 / T_m) PW \tag{4.8}$$

where PW is precipitable water vapor, T_m is the mean temperature, the molecular weight of water, M_w, is 18.0152 kg.kmol^{-1}, k_2' is 0.221 K/Pa and k_3 is 3739 K^2/Pa [*Bevis et al,* 1994].

The mean temperature is defined as

$$T_m = \frac{\int (P_w / T) dz}{\int (P_w / T^2) dz} \tag{4.9}$$

Mean temperature can be estimated a number of ways. Integrating direct measurements through

the atmosphere, i.e. along radiosonde profiles, is the most accurate method. This is obviously impractical for operational GPS processing. However radiosonde datasets may be used to estimate simplified models of T_m. Bevis et al [1992] analyzed radiosonde profiles over two years for the United States. Comparing these radiosonde values to a constant value for T_m = 260 K leads to ~15% errors due to atmospheric variations with location and time. A linear regression of mean temperature with respect to surface temperature yielded better results, using $T_m = 70.2 + 0.72\ T_s$ (temperature in kelvins) leads to a relative error no more than 2%. When numerical weather models are available we may vertically integrate through the model levels to obtain an estimate for mean temperature, much like integrating a radiosonde profile. When the National Meteorological Center's Nested Grid Model was compared to radiosonde data the error was less than 1% [*Bevis et al,* 1994]. We will use the NCEP global analyses to directly integrate for mean temperature, this is likely to have approximately the same relative error as the Bevis et al [1994] estimate for mean temperature. It should certainly be more accurate than the linear surface temperature estimate which is only based on continental U.S. data.

The basic equations may be re-arranged to derive precipitable water vapor as a function of total delay and surface pressure such that

$$PW = \frac{ZD - 10^{-6} k_1 \frac{R}{M_d} g_m^{-1} P_S}{10^{-6} \frac{R}{M_w} (k_2' + k_3 / T_m)} \tag{4.10}$$

where *ZD* is total zenith delay as estimated from GPS data processing, and surface pressure is from either an in-situ meteorological unit or estimated from NCEP global analyses. We have used the NCEP estimate for mean temperature even for stations with in-situ surface meteorology.

Given an approximate value of 9.8 ms^{-2} for mean gravity, the hydrostatic delay goes as 2.3 mm per hPa, or 2.3 m for a typical surface pressure value of 1000 hPa. This is the major component of the total zenith delay. When 260 K is used for as a typical value for mean temperature, the wet delay goes as 6.7 mm per mm PW. Precipitable water vapor can vary from less than 5 mm in polar regions and up to 50 mm in the tropics, leading to 3 to 35 cm of wet delay.

4.3 Data

4.3.1 GPS Atmospheric Delay

The GPS system is fundamentally a ranging system. Signal travel times between satellites and ground stations are converted into ranges, if the satellite positions and the ranges between multiple satellites and ground stations are known then the positions of the ground stations can be calculated. Any effect that modifies the ranges must be estimated and accounted for when processing GPS data. The atmospheric delay is one of these effects. If the atmospheric delay is parameterized, these parameters may be estimated for each station as part of the overall GPS solution.

The GPS data we will be using come from the International GPS Service (IGS). IGS maintains a global network of over 100 permanent GPS stations (Figure 4.1). Data from these stations are processed by a number of IGS Analysis Centers [*Beutler et al,* 1999]. The Analysis Center results we have used in this study are from the Scripp's Orbit and Permanent Array Center (SOPAC). This Analysis Center processes the greatest number of global stations and data from SOPAC are readily available via anonymous ftp. Zenith delay estimates are produced hourly along with standard error estimates.

SOPAC uses the GAMIT/GLOBK GPS processing software, which is distributed by the Massachusetts Institute of Technology's GPS and Geodynamics Group [*King et al*, 1999; *Herring*, 1998]. GAMIT uses a weighted least squares algorithm to jointly estimate station positions, satellite orbits, station zenith delays, and other required parameters. The GLOBK Kalman filtering software is then used to combine the GAMIT solutions from different networks or observation sessions. As shown in the previous section, the atmospheric delay is usually expressed as a combination of hydrostatic and wet zenith delays, with corresponding mapping functions that account for the increase in delay with decreasing elevation angle. These delay and mapping algorithms are used by GAMIT/GLOBK to estimate corrections to the zenith delay from an a priori value, usually based on default meteorological values. The time variation of the zenith delay is modeled as a piecewise linear function between time steps, constrained using a random walk stochastic process [*Herring et al,* 1990; *Tralli et al,* 1992]. The standard errors reported by SOPAC for the IGS stations are typically less than 6 mm. Total zenith delay values are typically on the order of 2.3 meters, with the wet component typically in the range of 0 - 30 cm. These delay values are

denoted as "GPS" delays throughout this chapter.

In addition to SOPAC zenith delay estimates, we will also be using the IGS combination tropospheric estimates as a check on some of the SOPAC results. IGS has seven different Analysis Centers (AC) that separately process GPS data from the IGS global network of stations. Each AC uses slightly different processing methods and parameterizations, resulting in varying zenith delay estimates between ACs. A single combined product is produced every 2 hours, the consistency between ACs is at the 4 mm level for both bias and standard deviation [*Gendt*, 1996, 1997, 1998].

4.3.2 Numerical Weather Model

Given an estimate of total zenith delay from GPS processing, if surface pressure and mean temperature are known then Equation 4.10 may be used to estimate precipitable water vapor. In the absence of in-situ meteorological data, numerical weather models may be used to estimate these atmospheric variables. In the case of mean temperature, using a numerical weather model is far more accurate than using an estimate based on surface temperature [Bevis et al, 1994]. For surface pressure, direct measurements are certainly more accurate than numerical weather model estimates. However, less than a third of the IGS global stations have meteorological packages. Therefore the numerical weather model estimates of surface pressure have the decided advantage of being available at every station.

The numerical weather model data we have used are from the National Center for Environmental Prediction (NCEP) global analyses. These analyses are output from the Global Data Assimilation System (GDAS), which assimilates various observational meteorological data sets and produces global grids of atmospheric variables at various vertical levels. The NCEP fields are produced on 1 degree uniform latitude and longitude grid every 6 hours, starting at 0 GMT. The NCEP global analyses are more extensively described in section 2.2 of Chapter 2, and the spatial and temporal interpolation methods used with this data are also discussed. The NCEP data and GPS station location information are used to calculate surface pressure, precipitable water vapor, and mean temperature at each station, which are used to estimate total zenith delays. These delay values denoted as "NCEP" delays throughout this chapter.

4.3.3 Surface Pressure

Surface pressure is an integral component of the GPS delay estimates. Even more so, surface pressure is the most important component of the optical delay estimate used for the ICESat delay correction. If the NCEP surface pressure estimates are sufficiently accurate we can use them to calculate precipitable water at GPS stations, using the zenith delay estimated by GPS processing. Unfortunately, the NCEP global analyses do not provide error estimates with their products. However, comparisons with other operational weather models may qualitatively point out problem areas, such as the high Southern latitudes [*Trenbreth and Olsen,* 1988]. We shall quantitatively validate the NCEP surface pressure estimates using the in-situ measurements at GPS stations.

We have compared NCEP surface pressure estimates to GPS meteorological unit measurements for two years of data in 1999 and 2000, using GPS stations within the IGS global network. The GPS meteorological units (MET's) are in-situ meteorological stations that measure temperature, pressure, and humidity. These values are generally reported at least every hour. The pressure sensors used in the IGS network are Paroscientific digiquartz pressure transducers. The reported accuracy is +- 0.01% of the value, which +- 0.1 hPa for a typical surface pressure value of 1000 hPa. These pressure transducer may drift downwards with time but the drift should be less than 0.1 hPa per year. Calibrations every 2 to 3 years will alleviate this problem.

NCEP produces a direct surface field, however this field is unsuitable for geodetic purposes. The raw topography NCEP uses is taken from the US Navy 10 arcminute dataset, which is area averaged in the spectral domain to the NCEP one degree grid resolution. This creates spurious waves in the surface pressure near steep gradients and also smooths out high relief. For a vertically integrated variable like total precipitable water vapor this leads to incorrect integration ranges. Areas where the NCEP topography is expected to be in error are small islands, flat areas adjacent to high relief (Gibb's effect), and the tops of mountains.

We calculated the NCEP surface pressure using the upper atmospheric level fields of geopotential height, temperature, and relative humidity. Surface pressure is estimated at the GPS station locations by spatially interpolating the NCEP fields to GPS station locations and then integrating to the surface, this algorithm is detailed in Appendix A. This method requires that the geodetic latitude, longitude, and height above geoid of the GPS station be known. However, the GPS data processing calculates Earth centered, Earth fixed coordinates. The conversion from geocentric

latitude, longitude, and radius to geodetic latitude, longitude, and height above ellipsoid can be calculated using a direct solution. This solution is accurate to a centimeter [*Bowring,* 1976]

$$\lambda_C = \lambda_D$$

$$\phi_D = \operatorname{atan}\left(\frac{Z + e'^2 b \sin^3\theta}{p - e^2 \cos^3\theta}\right)$$

$$h = \frac{p}{\cos\phi_D} - N(\phi_D)$$

where ϕ_C,λ_C,R_C are geocentric coordinates, ϕ_D,λ_D,h are geodetic coordinates

$$\begin{aligned} Z &= R_C \sin\phi_C \\ p &= R_C \cos\phi_C \\ \theta &= \operatorname{atan}\left(\frac{Za}{pb}\right) \\ N(\phi_D) &= \frac{a}{\sqrt{1 - e^2 \sin^2\phi_D}} \\ e'^2 &= \frac{a^2 - b^2}{b^2} \end{aligned} \tag{4.11}$$

For the WGS-84 ellipsoid, the semi-major axis (a) is 6378137.0 m, the semi-minor axis is 6356752.3142 m, and the eccentricity squared (e^2) is 0.00669437999013. To convert geodetic height above ellipsoid to height above geoid, we use the WGS-84 30 arcsecond geoid value grid distributed by the National Imagery and Mapping Agency [*NIMA,* 1997], bilinearly interpolated to the GPS station locations. Height above geoid is ellipsoidal height minus geoid value.

During the time period of our study (1999-2000), there were 32 IGS stations reporting surface pressure measurements. For each of these stations we calculated NCEP surface pressure and compared the MET values where the two time series intersected. The NCEP estimates are produced every 6 hours, we chose to examine only those stations with at least 200 days of joint pressure data, i.e. 800 points, to ensure sufficient data. The MET surface pressure time series are sporadic for a number of stations, these stations also tend to have less reliable values. The 200 day restriction reduced the number of stations to 18. The locations of the GPS stations are shown in Figure 4.1, those with meteorological units are indicated by triangles, those without by squares. The overwhelming majority are located in the continental United States.

For each of the 18 stations we calculated a mean bias between the NCEP surface pressure

estimate and the MET value and a corresponding standard deviation of the differences. These statistics are listed in Table 4.1 along with station location information, note that height is with respect to the geoid.

Table 4.1. Statistics of surface pressure differences (NCEP - MET), averaged over 2 years

Station	Latitude	Longitude	Height (m)	No. points	Mean Bias (hPa)	Sdev (hPa)
ALBH	48.39	236.51	50.96	1221	0.3224	0.5750
ALGO	45.96	281.93	235.82	1213	0.9662	1.2493
AOML	25.73	279.84	26.73	2080	0.2523	0.4500
AUCK	-36.60	174.83	98.08	1565	-0.8174	0.5382
BAHR	26.21	50.61	9.05	2052	0.5694	0.6015
BJFS	39.61	115.89	98.18	939	0.1196	0.8741
CHAT	-43.96	183.43	48.03	1584	0.6497	1.6231
CHUR	58.76	265.91	26.45	1103	-0.8487	0.8488
JPLM	34.20	241.83	457.72	1307	0.0259	1.1232
MDO1	30.68	255.99	2027.87	1608	0.7787	0.6312
NRC1	45.45	284.38	115.25	1113	-0.7097	0.4958
POTS	52.38	13.07	103.67	1173	-0.9950	0.6996
PRDS	50.87	245.71	1263.24	994	1.9768	1.4262
SCH2	54.83	293.17	518.16	1256	1.5665	1.1273
STJO	47.60	307.32	143.05	974	1.4969	0.8552
USNO	38.92	282.93	82.62	2549	0.8165	0.8733
WES2	42.61	288.51	113.54	2356	-1.1788	0.6481
YELL	62.48	245.52	206.78	1237	0.6315	0.4337

Figure 4.2 graphically shows the statistics from Table 4.1, the upper plot shows the mean biases of the pressure comparison and the lower plot shows the standard deviation. Unfortunately, most of the stations are clustered in the United States. There may be insufficient coverage be certain, but based on these plots there does not appear to be a geographical dependence to the means and variances. For example, AUCK and CHAT are relatively close together yet have significantly different standard deviations. Figure 4.3 shows the time series for these two stations. The pressure variations show the same basic pattern, however CHAT has much more intense pressure variations. This is largely due to the fact that CHAT is on a island directly in the path of prevailing weather systems from the East. The higher pressure differences for CHAT may be due to the intense lows in the record. The NCEP model is known to sometimes underestimate sharp lows, an example of this is around day 58, 1999 for CHAT (Figure 4.4). Compare this to the same time

interval for AUCK, where the intense low is not present.

Combining all the stations into a single statistic, Figure 4.5 shows a scatter plot of pressure differences and the corresponding histogram. The overall mean of the pressure differences is 0.2758 hPa, the standard deviation is 1.2027 hPa. Based on this, and the individual station results, we expect the upper bound on NCEP surface pressure rms error to be less than 2 hPa, with no discernible systematic bias. To find what effect this surface pressure error will have on precipitable water vapor estimates, consider a very simplified version of Equation 4.10:

$$PW \approx (ZD - aP_S)/b \tag{4.12}$$

where a is approximately 2.3 mm/hPa and b is approximately 6.7 mm/(mm PW). Assuming for now the errors in ZD and P_S are uncorrelated, the error budget for PW is

$$\sigma_{PW}^2 \approx \frac{\sigma_{ZD}^2}{b^2} + \left(\frac{a}{b}\right)^2 \sigma_{P_s}^2 \tag{4.13}$$

The zenith delay error for the GPS processing is approximately 10 mm [*Rocken et al*, 1995] and when combined with the surface pressure the above equation goes as

$$\sigma_{PW} \approx (2.2277^2 + 0.4714^2)^{1/2} \text{ mmPW} \approx 1.6 \text{ mmPW} \tag{4.14}$$

This is of sufficient accuracy that we will be able to use NCEP surface pressure to calculate precipitable water vapor in the following analyses, thus greatly increasing the available amount of data.

It should be noted that the surface pressure biases calculated using the GPS meteorological units are valid, since we have precise measurements for the station heights. This was not the case for the surface pressure comparisons in Chapter 3 which used the automatic weather stations. Unfortunately, there are no MET units in the polar regions where we wish to validate the ICESat atmospheric delay. Also, the latitude coverage of the existing MET units is too clustered to say whether there is a systematic bias in the NCEP surface pressure calculations. Therefore, while the biases calculated are statistically significant, without a systematic variation it is difficult to say whether the biases are due to errors in the NCEP model or errors in the MET data or errors in the GPS station height calculations. Regardless, the biases are within ±2 hPa for individual stations and are well within the ICESat error budget.

4.3.4 NCEP Precipitable Water Vapor

There are two ways we can calculate NCEP precipitable water vapor. NCEP produces a total column precipitable water vapor field. However, this field potentially has the same accuracy concerns as the NCEP direct surface pressure field, given that is it integrated down to the same problematic topography field. The other way to calculate precipitable water vapor is to integrate through the atmospheric column ourselves to the GPS station height, much like the surface pressure integration method described in Appendix A. This value of precipitable water vapor is an integral of water vapor density through the atmosphere:

$$PW = \int_{Z_0}^{\infty} \rho_w dZ \tag{4.15}$$

where PW is the integrated precipitable water vapor, ρ_w is water vapor density, and Z_0 is station height. The NCEP atmospheric fields are produced on a set of standard vertical levels. Equation 4.15 can be approximated by piecewise numerical integration between the vertical levels, starting at the surface and going up to the top of the troposphere. Water vapor density is calculated from the temperature and relative humidity fields.

To test whether the integrated NCEP precipitable water vapor value is better than the direct NCEP field, we compared these values to GPS estimates of precipitable water vapor calculated using Equation 4.10. We wish to see which version of NCEP PW minimizes the errors with respect to GPS PW. Figure 4.6 shows the two comparisons with respect to latitude, averaged over the two years of data. The upper plot is the integrated NCEP PW comparison and the lower plot is the direct NCEP PW comparison. Overall, the direct field has a greater variance than the integrated field. The very worst comparisons are for two GPS stations in Hawaii: Mauna Kea (MKEA) and Kokee Park (KOKB). MKEA has a mean difference of 25.58 mm precipitable water vapor, KOKB has a mean difference of 14.05 mm. Figure 4.7 helps to explain why. The contours are for the NCEP topography field. The elevation of the MKEA GPS station is 3738 m, yet the NCEP topography shows approximately 15 m. For KOKB the GPS station elevation is 1157 m, while the NCEP elevation is at most 5 m. This is a classic example of smoothing for high relief at scales of less than a degree, the NCEP spatial resolution. The peaks of the Hawaiian islands are completely missed. Based on these comparisons, we will use integrated NCEP PW for the next section. It is important to use integrated PW for calculating GPS delays, considering that 1 mm PW corresponds to approximately 6.7 mm of delay. It is not so important for the ICESat

optical atmospheric delay calculations, where 1 mm PW corresponds to 0.08 mm of atmospheric delay.

4.4 Results

Based on the results of the surface pressure comparisons, we have used the NCEP derived surface pressure and GPS delay estimates as inputs to Equation 4.10 to calculate precipitable water vapor (PW), theoretically within 1.6 mm PW. Calculating precipitable water vapor using MET surface pressure should be accurate to within 1 mm PW [*Rocken et al,* 1995]. These values for precipitable water vapor are generically referred to as GPS precipitable water vapor values, even though most stations use NCEP surface pressure in their derivation. The fact remains that most of the variation is from the GPS delay estimates.

The GPS precipitable water vapor estimates have been compared to the NCEP integrated precipitable water vapor, with the goal of discerning any geographical or temporal patterns in the differences. We are particularly interested in latitude dependence or annual signals. This would have implications for the accuracy of ICESat measurements and would also help improve our understanding of precipitable water vapor in numerical weather models.

For differences calculated using MET surface pressure we had 14 stations available, whereas for differences calculated using NCEP surface pressure we had 116 stations available. This clearly illustrates the value of using NCEP surface pressure to increase the data coverage. Comparisons for the entire data set, all stations over 2 years, are shown in the scatter plots of Figure 4.8. The top plot shows the comparison between the NCEP PW and the GPS PW using MET surface pressure, the bottom plot is the comparison between NCEP PW and the GPS PW using NCEP surface pressure. Both of the comparisons to NCEP PW have rms values less than 3 mmPW. It is gratifying to see that the rms spread for the population that uses the NCEP surface pressure is not that much bigger than the one with MET surface pressure. For individual station comparisons using MET surface pressure, the mean precipitable water vapor differences (NCEP - GPS) ranged from -0.71 to 0.57 mm PW and the standard deviations ranged from 1.56 to 3.50 mm PW. For comparisons using NCEP surface pressure the mean differences ranged from -2.38 to 1.93 mm PW and the standard deviations ranged from 1.02 to 5.16 mm PW.

Figure 4.9 shows the latitude dependence of these station averaged differences. The upper

plot shows the mean differences and the lower plot shows the rms differences. As an aside, note that the data points using MET surface pressure do not form a discernibly different population from the data points using NCEP surface pressure, which is in agreement with the almost equal predicted PW errors quoted at the beginning of this section and the total population statistics discussed above. The PW mean differences have no obvious variation with latitude. However the PW rms differences do, this is almost certainly due to the increased absolute value and/or variability of water vapor the mid latitudes and tropics. For a quick qualitative test of this hypothesis we re-plotted the PW rms differences from Figure 4.9 with respect to the NCEP PW mean and standard deviation, the results are shown in Figure 4.10. There is a definite linear correlation between the PW rms difference and PW mean value. However, there does not appear to be a correlation with respect to PW standard deviation. It should be noted that for the purposes of ICESat delay calculation, rms differences of less than 6 mm PW lead to optical delay rms errors of less than 0.5 mm, pratically negligible, and the differences are even lower in the polar regions where ICESat's primary mission is focused.

In order to see temporal patterns in the precipitable water vapor comparisons we have calculated the mean and rms differences averaged over 30 day intervals. In order to see the global patterns, we calculated zonal averages every 5 degrees with a 15 degree moving boxcar average. Zonal averages calculated this way have a number of caveats. Since the station distribution is not uniform over the Earth (refer back to Figure 4.1) it follows that these are not true zonal averages. Data over the oceans is completely missing unless one counts the small island data. The Northern Hemisphere mid-latitude band will be dominated by U.S. data and the Southern Hemisphere sub-tropics will be dominated by data from Australian stations. Another consequence of the station distribution is that some zonal averages only have 2 or 3 stations, primarily in the Southern Hemisphere. In fact, we couldn't extend the zonal averages all the way to the poles because of a shortage of polar stations.

Figure 4.11 shows the zonal averages for precipitable water vapor, Figure 4.11(a) is the integrated NCEP value and Figure 4.11 (b) is the GPS derived value. There are definite differences in the tropics, the NCEP field is noticeably drier. The mean differences have been calculated and are shown in Figure 4.12(a), the corresponded rms differences are shown in Figure 4.12(b). The NCEP field is indeed drier in the tropics over most of this time period, and the difference seems to be increasing with time. Using the data in Figure 4.12(a), we have calculated zonal trends with a

linear flight over the 2 years (Figure 4.13), the highest values are around 10^{o}S. These may not be a true secular trends, 2 years of data is not sufficient to study climatological trends. For example the El Nino-Southern Oscillation (ENSO) cycles on average every 3-4 years so any trend estimates should be based on decadal length studies. The rms differences in general show the same pattern of variation as the absolute precipitable water vapor values. This is in agreement the results shown in Figures 4.9 and 4.10.

Trenberth and Guillemot [1995] evaluated the NCEP moisture budget against satellite based measurements, from 1987 to 1991. Keeping in mind that these satellite measurements were only over the oceans, whereas we are using land based GPS stations, some of the same general patterns are in both sets of results (see Trenberth and Guillemot's Figures 4.11 and 4.12, for zonal-time series plots of PW mean and rms differences). The Trenberth and Guillemot show mean biases that are higher in the tropics, as are the rms differences, and the range of values are similar to our results.

A breakout of selected individual stations is shown in Figure 4.14. The top panels in each figure are absolute values of precipitable water vapor, both NCEP and GPS estimates. The middle panels show the mean differences, GPS values subtracted from the NCEP values as in Figure 4.12. The bottom panels show the rms differences. Figure 4.14(a) shows the two stations available in Greenland and Figure 4.14(b) shows the stations with sufficient data for analysis in Antarctica. Note the difference in scale for absolute PW and the more pronounced annual signal in the Greenland data. There is a corresponding annual signal in the rms differences, albeit less obvious. There actually does not appear to be an annual signal in the Antarctic rms differences, rather a downward trend. Perhaps when the atmosphere is this dry there are other errors dominating the rms differences such that the correlation with absolute PW is obscured. Figure 4.14(c) has example stations from the mid-latitudes, as expected from the zonal plots there doesn't appear to be any trends in data. Figure 4.14(d) has example stations from the tropics, compared to the mid-latitude stations there are distinct trends in the mean differences. Note that the scales are the same for Figures 4.14(c) and 4.14(d), except that the absolute PW scale for the tropics has been offset by 20 mmPW. Both the absolute PW values and PW variability are increased in the tropics.

There are two possible reasons for this trend in the tropics, seen in both the zonal averages and the individual stations. Either the NCEP numerical weather model is systematically getting drier in the tropics or the GPS model is increasingly overestimating PW in the tropics. If this is a

real drying trend in the NCEP model then the GPS analysis is not picking it up, for reasons that are unclear. Or there may be something going on with the NCEP model. We are using what is known as the operational NCEP model, model parameters and algorithms will change over time as better methods are incorporated. During the 1999-2000 time frame there were a number of increases to model resolution, perhaps leading to better estimates of water vapor since this is one of the most highly variation atmospheric components. October 1, 2000 an improved orography model was adopted. However, this should have limited effect on our analysis because we vertically integrate our surface pressure and precipitable water vapor fields using the upper atmospheric levels rather than using NCEP's provided surface fields.

There may be a systematic drift in the GPS precipitable water vapor estimates. A global analysis of GPS data between 1992 and 2000 has seen an overall trend in the scale of the global network of approximately -1 mm/yr [*Herring*, 2001]. However this drift is the opposite sign from what you would need to explain our data. At this stage we should further analyze the Scripps data itself. We have compared the Scripps data to the IGS combined tropospheric product described in Section 4.1. Using at the same stations in the mid-latitudes and tropics as in Figure 4.14, Figure 4.15 shows the comparison between the IGS combination zenith delay and the Scripps estimate as a mean bias and standard deviation, using weekly averages. Note that these plots are in units of zenith delay, 6.5 mm of ZD error is approximately equal to 1 mm of precipitable water vapor error. Both figures are on the same scale. There is no discernible trend in the mid-latitude stations, the tropical stations data are too variable to tell, particularly for FORT. The other two tropical stations shown, ASC1 and DGAR, show significant decreases in the standard deviation over the 2 years. A point to note, however, is that this apparent increase in Scripps processing accuracy is probably more a function of the different IGS Analysis Centers' methods converging, particularly with regards to mapping functions and elevation angle cut-offs which significantly effect the zenith delay estimates. Also, the number of Analysis Centers and the number of stations each AC is processing is increasing. Table 4.2 shows the changes in zenith delay modeling from the beginning of 1999 to the end of 2000 for each Analysis Center.

Table 4.2. Analysis Center changes in zenith delay models from 1/1/1999 to 12/31/2000

Analysis Center	Jan 1999: Mapping Fnc	Cutoff [deg]	Dec 2000: Mapping Fnc	Cutoff [deg]
CODE	Dry Neill	10	Neill	10
NRC			Neill	15
ESA	Saastamoinen	20	Saastamoinen	20
GFZ	Dry Neill	20	Dry Neill	15
NOAA	Neill	15	Neill	15
SOPAC	Saastamoinen	7	Neill	10

Scripps has undergone significant adjustments in zenith delay models, changing mapping function and elevation angle cutoff. Figure 4.16 is a clearer version of Figure 315, it shows a simple average of the three stations in each zone, also plotted is the global average of the comparison between the IGS combination and SOPAC, using all available stations. It seems there may well be a downward trend in the Scripps data compared to the IGS combination. If we trust the IGS product more, that would imply that the Scripps data is in error. The big problem with this for our analysis is that the sign of the trend is wrong to explain the trends seen in Figures 4.12 and 4.14. To explain our comparisons we would expect the GPS zenith delay estimates to have an anomalous *upward* drift. Also, the slight downward trend in the IGS/SOPAC comparison too small even if the sign was correct, there is maybe a -1 mm ZD drift over 2000 in the tropics. This corresponds to only -0.15 mm PW. For now, we can't definitely say why there is a drift in the tropics for the NCEP to GPS PW comparison. It's unclear whether the issue is with the NCEP data or the GPS data, or even both. The fact that the systematic drift is in the tropics but not the mid-latitudes or polar regions suggests that it might have something to do with high levels of PW, or even GPS constellation geometry. Further analysis needs to be done.

All the results so far suggest that the rms differences between NCEP PW and GPS PW appear to be correlated with the absolute precipitable water vapor values. Bevis et al [1996] also saw this general relationship when comparing numerical weather model estimates of zenith delay to those calculated from radiosonde profiles. The next logical step is to examine the data with respect to PW. We have calculated the mean and rms PW differences averaged over 2 mm PW bins, using all the available stations. Figure 4.17 shows these results, the top panel shows the number of data points used in each bin, we have set a minimum of 50 for a bin to be used, the middle panel shows the mean PW differences, and the bottom panel shows the rms differences.

An empirical relationship for the rms differences with respect to absolute PW value can be formulated. For absolute PW values of less than 30 mm PW the correlation is almost linear, a rule of thumb relationship is

$$RMS_{PW} = (1 + 0.1PW) \tag{4.16}$$

where the units are mm PW. If one assumes that all the differences are due to errors in the NCEP PW value, then this equation can be used to estimate the rms error in the wet delay for the ICESat mission, since the precipitable water vapor values tend to be much less than 30 mm PW in the polar regions. For precipitable water vapor values over 30 mm PW, the rms difference values tend to level off to 5 mm PW, giving an upper bound on the error.

The mean difference plot with respect to absolute PW in Figure 4.17 shows some curious patterns that we do not have a good explanation for as yet. We know that the overall bias between NCEP PW and GPS PW is negative, on the order of -0.24 mm PW (see Figure 4.8, bottom panel). For absolute PW from 0 to 55 mm PW the bias is negative and is generally trending downwards, reaching a low value of almost -1 mm PW for an absolute PW value of approximately 45 mm PW. Referring back to the zonal averages in Figures 4.11 and 4.12, the NCEP PW does indeed appear to be less than the GPS PW estimate in general and the lowest values are in the tropics where precipitable water is high. The NCEP model's precipitable water vapor values are for the most part driven by measurements made by radiosondes. Some of the radiosondes may not reaching the top of the wet troposphere, therefore underestimating the amount of water vapor. The absolute bias from this type of error would be greatest in areas of high precipitable water vapor where there is more water vapor distributed throughout the entire atmospheric column.

For absolute precipitable water vapor values greater than 50 mm PW, the biases trend sharply upwards, becoming positive and reaching a value of 2 mm PW when absolute PW is around 60 mm PW. Note that the number of points used in each bin for the higher values of absolute PW is relatively low, there are only 100 - 1000 points and 10 - 25 stations used in the bins greater than 60 mm PW. If one assumes that all the errors are in the NCEP PW values then this would imply that for very high values of precipitable water vapor the NCEP model is over estimating. Perhaps it is the case that for high PW values there is also high temporal variability and the NCEP model is preferentially missing the troughs, much like the surface pressure example in Figure 4.4. However, this relationship of positive bias for very high values of precipitable water vapor is not evident in any of the previous averages performed. It may be due to some other rela-

tionship that happens to be correlated with high PW. Referring back to Figure 4.14(d), the highest biases are at the beginning of 1999 for the example tropical stations. It may be only a subset of the tropical data that has the high bias. For Figure 4.18 we plotted the PW binned biases as two subsets, one for the first half of 1999 and the other for the last half. The upward trend and positive biases for very high values of PW are still there, the only difference is that the biases have a mean offset, which agrees with are analysis of Figure 4.14. At this point we do not know what is causing this curious effect. However, it is a very small subset of the data and will not be a concern for the ICESat atmospheric delay calculations over the polar regions.

Much of the preceding discussion of the results has focused on data with high precipitable water vapor values, in general assuming any problems to be due to the NCEP numerical weather model. However, as alluded to in the discussion of the bias drift with time in the tropics, the GPS data may have it own issues that will effect the PW estimate through erroneous modeling of the zenith delay. For example, errors in the mapping functions tend to increase with decreasing elevation angle [*Davis et al*, 1985; *Niell*, 1996]. For stations near the poles the GPS satellites appear lower on the horizon and the GPS data will have on average lower elevation angles, thus higher sensitivity to elevation angle dependent errors. Evidence for this isn't seen in the results so far, e.g. the latitude averaged results in Figure 4.9. But it may be the case that for areas with typically high PW, i.e. the mid-latitudes and tropics, the errors between NCEP PW and GPS PW estimates are dominated by error in the NCEP data, whereas for the polar regions, which typically have low PW, the error may be due to the GPS data.

For small values of total precipitable water vapor the GPS zenith delay estimate should be the same as the optical delay estimate, with the exception of a 0.9865 multiplier on optical delay to account for slightly different refractivity constants. Therefore for small values of PW the GPS delay comparison becomes a direct validation of the ICESat total delay estimate. For PW values less than 5 mm PW we have sorted the zenith delay estimates into 0.1 mm PW bins and calculated the mean and rms bias for all bins with more than 50 data points. Because we are now looking at zenith delay values, any errors in the NCEP estimate will be a combination of the surface pressure and integrated water vapor errors, whereas the errors in the GPS estimates will be purely due to the GPS processing. Figure 4.19 shows the zenith delay comparisons between NCEP zenith delay estimates and those estimated by GPS processing, the top panel shows the number of data points in each bin, the middle panel shows the mean zenith delay differences, and the bottom panel

shows the rms differences.

The mean bias over this range of PW is consistently less than zero. If we assume the GPS delay values are correct then the NCEP delay values are being underestimated. The NCEP surface pressure comparisons with in-situ measurements, as shown in Figure 4.5, show the NCEP to be slightly high when averaged over all stations, this would lead to a positive delay bias. Some validation studies indicate that the NCEP surface pressure tends to be over-estimated for strong synoptic systems where the analyses miss the trough of the low [*Cullather et al*, 1997; *Trenberth and Olsen*, 1988]. The Antarctic coastal stations used in this study, where the PW values are typically low, experience intense storms that circulate around the continent. Therefore, the NCEP pressure may be too high which would not explain the negative delay bias seen in Figure 4.19. On the other hand, precipitable water vapor values may be too low. NCEP water vapor fields are initialized using observations from radiosonde profiles, the radiosonde humidity sensors tend to have a dry bias when the temperature and humidity are very low [*Elliot and Gaffen*, 1991]. This would tend to agree with the negative bias seen in our zenith delay comparisons. However, in absolute terms this error should become less as PW gets lower, which is opposite to the trend seen in Figure 4.19.

Conversely, if the NCEP zenith delay values are correct then the GPS values are too high. This could be due to could indicate a problem with the GPS zenith delay modeling, e.g. erroneous mapping functions. Scripps uses the Niell mapping function in it's processing [*Niell*, 1996]. This mapping function varies with latitude and has a sinusoidal annual component, the parameters were estimated using data from a number of radiosonde stations ranging in latitude from 43°S to 75°N, with the majority of stations in the Northern Hemisphere. It is possible that this mapping function does not do a good job in Antarctica. A future study should look at this issue by comparing radiosonde or numerical weather model derived mapping functions to the Niell mapping function in Antarctica and assess the effect on zenith delay comparisons. Niell gives ZD uncertainties of approximately 3 mm for 5° elevation angle, and states that above elevation angles of 15° the error is negligible. Certainly in Antarctica the average elevation angle is lower, however this does not explain the systematic trend in our zenith delay bias.

There may be problems with other GPS model parameter estimates which can map into delay, e.g. errors in the station height, multipath errors, or mis-modeling of the antenna phase pat-

tern. Incorrect stations height estimations will map into zenith delay errors, the rough rule of thumb is 3 mm zenith delay for every 1 cm height change. Multipath effects from signal scattering at the ground station have been shown to produce shifts in apparent station height [*Elosegui et al*, 1995]. Any error in the station height will lead to an error in the zenith delay, we expect this effect to be restricted to those stations whose antennas placement makes them susceptible to multipath effects. For example, antennas mounted too low to the ground will see low frequency multipath which can be mismodeled as tropospheric delay [*Meertens et al*, 1996]. Antenna phase center variations (PCVs) are a network wide issue. The PCVs are primarily elevation angle dependent and must be correctly modeled and accounted for in high precision GPS processing. Studies have shown that the nominal values for the phase center offsets given by the antenna manufacturers are unreliable and may have discrepancies of up to 4 cm. Rothacher et al [1995] looked at this issue of phase center variations and the effect on station height and tropospheric delay estimates. They found errors of up to 10 cm in station height if the antenna types were mixed and a scale factor in baseline length of up to 0.015 ppm if the same antenna types were used. Incorrectly modeled phase center variations can easily be mismodeled as tropospheric delay, especially at low elevation angles since both models are highly elevation angle dependent. The IGS network has a mix of antenna types in use, although most are Dorne Margolins choke ring antennas. Since 1996, all the major IGS Analysis Centers have been using phase center variation corrections that are defined relative to the Dorne Magolin antennas [*Beutler*, 1996]. These relative corrections have been empirically determined. This accounts for the mixed antenna type errors but there will still be an absolute scale error in the IGS network.

We have examined the GPS zenith delay comparisons for low precipitable water vapor values. The errors derived from this comparison should be the same as the hypothetical optical delay errors. We will now look at the GPS zenith delay comparisons for the entire range of precipitable water vapor values. If we assume all of the delay error in the GPS signal is due to surface pressure, then the GPS delay error becomes the upper bound for the optical delay error. This is unless the surface pressure and precipitable water vapor errors are anti-correlated. In Figure 4.20 we compared the surface pressure differences to the precipitable water vapor differences, there is no discernible correlation. Therefore, we may use the GPS delay error as an estimate for the upper bound of the optical delay error. Figure 4.21 shows the zenith delay comparisons between NCEP zenith delay estimates and those estimated by GPS processing for the entire range of PW. The top

panel shows the number of data points in each bin, the middle panel shows the mean zenith delay differences, and the bottom panel shows the rms differences. The maximum rms error is approximately 28 mm for PW values of greater than about 42 mm PW. If these were the true errors for optical delay they would be beyond the error budget for the ICESat atmospheric delay correction of 20 mm total. However, the assumption is that all of the GPS delay error is due to surface pressure, whereas we are fairly confident that most of the error is due to precipitable water vapor. The ICESat error budget is defined for the primary mission of mapping the icesheets of Greenland and Antarctica. Figures 4.14(a) and 4.14(b) show that the precipitable water vapor values in the polar regions are likely to be no greater than 20 mm PW. If we now return to the bottom panel of Figure 4.21, for a PW value of 20 mm, the rms GPS delay error is approximately 20 mm. This implies that the upper bound on the ICESat delay error in the polar regions is 20 mm, which is coincidentally the maximum allowable ICESat delay error.

4.5 Conclusions

Using GPS delay estimates and NCEP surface pressure has proved to be a valuable tool for validating the ICESat atmospheric delay calibration. Using these data sets, we have looked at comparisons between GPS derived precipitable water vapor and the NCEP integrated PW value. The location dependence and time variations in the rms PW errors point to the conclusion that the rms PW errors are directly related to the absolute value of PW. In general, the mean bias in the comparisons do not appear to show any systematic trends or annual signals in the polar regions. This is a good result for the primary ICESat mission, as any systematic effects in the atmospheric delay would map into spurious signals in the elevation change of the icesheets.

In order to use the NCEP surface pressure values we first validated them against in-situ meteorological units at a small subset of the IGS stations. The results in Section 4.3 indicated that the biases are $\pm$ 2 hPa and the rms error is less than 2 hPa, the biases showed no discernible systematic latitude dependence. We can't say whether these errors are due to NCEP modeling errors, including station height errors, or due to errors in the in-situ meteorological unit measurements. Using NCEP surface pressure estimates instead of in-situ measurements should add no more than 1.2 mm PW rms error. Being able to use the NCEP surface pressure values greatly increased the amount of available GPS derived precipitable water vapor data.

When we compared the GPS PW to the NCEP PW values we looked at the variability with location and time. The rms errors were higher in the tropics and showed an annual signal that peaked in the summer, pointing to a relationship between the PW rms error and the absolute PW value where the PW error goes up as the PW value goes up. When the comparisons were analyzed with respect to PW we were able to derive a rule of thumb relationship such that for values of PW less than 30 mm PW the rms PW error equals $1 + 0.1PW$ (all units in mm PW). For values of PW greater than 30 mm PW, the rms error levels off at approximately 5 mm PW. What does this mean for the ICESat delay error? Every mm of error in PW corresponds to 0.08 mm of optical delay error. Therefore based on these rms PW errors, for all values of PW the wet component of the ICESat delay error should be less than 0.4 mm, and for typical PW values of less than 20 mm PW in the polar regions the ICESat wet delay error should be less than 0.24 mm. This is well within the ICESat delay error budget. In fact, compared to the delay errors due to surface pressure that are practically negligible. In general, the biases for the PW comparison show no systematic effects, except for a troubling downward trend in the tropics. This is not an issue for the primary ICESat mission of mapping the polar icesheets but should be kept in mind for the land based elevation product. We are uncertain what this trend is due to, further investigation is required.

As an upper bound on the total ICESat delay error we looked at the GPS total delay comparison, assuming all the GPS error is due to surface pressure. This assumption is less valid for higher absolute values of PW since we are fairly confident that most of the errors in GPS delay are due to precipitable water vapor. Based on this comparison, the upper bound on the ICESat delay error, for all values of PW, is 28 mm. This is somewhat higher than the ICESat delay error budget of 20 mm. However the primary mission is for the polar regions, where PW values are typically less than 20 mm PW. Therefore the upper bound on the ICESat delay error in the polar regions is 20 mm, a convenient coincidence.

Comparisons of GPS delay where precipitable water vapor values are low should be a direct validation of the ICESat delay. It appears that the NCEP delay may be systematically biased low or alternatively that the GPS derived delay estimate is too high, by approximately 4 mm for zero PW. We are uncertain whether this bias is due to the NCEP numerical weather model or the GPS processing, or both. The implications either way are interesting and a determination of exactly where this bias is coming from should be further explored.

References

Beutler, G., Executive summary, *in Proceedings of the 1996 IGS Analysis Center Workshop (Silver Spring, MD), edited by P. VanScoy and R.E. Neilan, Pasadena, CA, Jet Propulsion Laboratory, JPL Publication 96-23*, xi-xvi, 1996.

Beutler, G., I.I. Mueller, R.E. Neilan, The International GPS Service for Geodynamics: development and start of official service on January 1, 1994, *Bull. Geod., 68*, 39--70, 1994.

Bevis, M., S. Businger, T. A. Herring, C. Rocken, R. A. Anthes, and R. H. Ware, GPS Meteorology: Remote sensing of atmospheric water vapor using the Global Positioning System, *J. Geophys. Res., 97,* 15,787-15,801, 1992.

Bevis, M., S. Businger, T. A. Herring, R. A. Anthes, C. Rocken, and R. H. Ware, GPS Meteorology: Mapping zenith wet delays onto precipitable water vapor, *J. Appl. Met., 33,* 379-386, 1994.

Bevis, M., S. Chiswell, S. Businger,T. A. Herring, Y. Bock, Estimating wet delays using numerical weather analyses and predictions, *Radio Sci., 31(3),* 477-487, 1996.

Bowring, B. R., Transformation from spatial to geographical coordinates, *Survey Review, 23(181),* 323-327, 1976.

Businger, S., S. Chiswell, M. Bevis, J. Duan, R. Anthes, C. Rocken, R. Ware, M. Exner, T. van Hove, and S. Solheim, The Promise of GPS Atmospheric Monitoring, *Bull. Amer. Met. Soc, 77(1),* 5-18, 1996.

Chahine, M. T., The hydrological cycle and its influence on climate. *Nature, 359(6394),* 373--380, 1992.

Ciddor, P. E., Refractive index of air: new equations for the visible and infrared, *Appl. Opt., 35,* 1566-1573, 1996.

Cullather R. I., D. H. Bromwich, and R. W. Grumbine, Validation of operational analyses in Antarctic latitudes, *J. Geophys. Res., 102,* 13,761-13,784, 1997.

Davis, J. L., T. A. Herring, I. I. Shapiro, A. E. E. Rogers and G. Elgered, Geodesy by radio interferometry: Effects of atmospheric modeling errors on estimates of baseline length, *Radio Sci., 20,* 1593-1607, 1985.

Duan, J., M. Bevis, P. Fang, Y. Bock, S. Chiswell, S. Businger, C. Rocken, F. Solheim, T. van Hove, R. Ware, S. McClusky, T. Herring, and R. King, GPS Meteorology: Direct Estimation of the Absolute Value of Precipitable Water, *J. Appl. Met., 35,* 830-838, 1996.

Elliott, W.P., and D.J. Gaffen, On the utility of radiosonde humidity archives for climate studies, *Bull. Am. Meteorol. Soc., 72*, 1507, 1991.

Elgered, G., An overview of COST action 716: Exploitation of ground-based GPS for climate and numerical weather prediction calculations, *Phys. Chem. Earth Part A, 26,* 399-404, 2001.

Elosequi, P., J Davis, R. Jaldehag, J. Johansson, A. Niell, I. Shapiro, Geodesy Using the Globa Positioning System: The Effects of Signal Scattering on Estimates of Site Position, *J. Geophys. Res., 100*, 9921-9934, 1995.

Gendt, G., Comparisons of IGS tropospheric estimates. *Proceedings IGS Analysis Center Workshop, 19-21 March 1996 Silver Spring, Maryland USA*, 151-164, 1996.

Gendt, ory, Pasadena, CA, 1997, pp. 169 - 182

Gendt, IGS Combination of tropospheric estimates - Experience from pilot experiment, *Proceedings IGS Analysis Group Workshop, Darmstadt, Germany*, February 1998.

Hasagawa, S. and D. P. Stokesbury, Automatic digital microwave hygrometer, *Rev. Sci. Instrum., 46*, 867-873, 1975.

Herring, T. A., J. L. Davis, and I. I. Shapiro, Geodesy by radio interferometry: The application of Kalman filtering to the analysis of very long baseline interferometry data, *J. Geophys. Res., 95,* 12,561-12,581, 1990.

Herring, T.A., GLOBK: Global Kalman Filter VLBI and GPS analysis program, *v.4.1, Mass. Inst. of Technol., Cambridge,* 1998.

Herring, T. A., Vertical Reference Frames for Sea Level Monitoring, *Fall AGU Meeting, San Francisco*, 2001.

Hill, R. J., R. S. Lawrence, J. T. Preistley, Theoretical and calculational aspects of the radio refractive index of water vapor, *Radio Sci., 17(5),* 1251-1257, 1982.

King, R.W. and Y. Bock, Documentation for the MIT GPS analysis software: GAMIT, *Mass. Inst. of Technol., Cambridge,* 1999.

Kuo, Y., Y. Guo, and E. Westwater, Assimilation of Precipitable Water Measurements into a Mesoscale Numerical Model, *Mon. Wea. Rev. 121,* April 1993.

Marini, J. W. and C. W. Murray, Correction of laser range tracking data for atmospheric refraction at elevation angles above 10 degrees, *NASA Tech. Rep. X-591-73-351*, 1973.

Meertens, C., J. Braun, C. Alber, J. Johnson, C. Rocken, T. Van Hove, B. Stephens, and R.Ware, Antenna and Antenna Mounting Effects in GPS surveying and Atmospheric Sensing, *EOS*

Trans. Amer. Geophys. Un., 77, F153, 1996.

Neill, A. E., Global mapping functions for the atmosphere delay at radio wavelengths, J. *Geophys. Res.*, 101, 3227-3246, 1996.

Niell, A. E., A. J. Coster, F. S. Solheim, V. B. Mendes, P. C. Toor, R. B. Langley, C. A. Upham, Comparison of measurements of atmospheric wet delay by radiosonde, water vapor radiometer, GPS, and VLBI, *J. Atmos. Oceanic Tech., 18,* 830-849, 2001.

National Imagery and Mapping Agency, Department of Defense World Geodetic System 1984: Its Definition and Relationships with Local Geodetic Systems, *NIMA Tech. Rpt 8350.2,* Bethesda, MD, Third Edition 4 July, 1997.

Rocken, C., R. Ware, T. Van Hove, F. Solheim, C. Alber, J. Johnson, M. Bevis, and S. Businger, Sensing atmospheric water vapor with the Global Positioning System, *Geophys. Res. Lett., 20,* 2631, 1993.

Rocken, C., T. Van Hove, J. Johnson, F. Solheim, R. Ware, M. Bevis, S. Chiswell, and S. Businger, GPS/STORM-GPS Sensing of Atmospheric Water Vapor for Meteorology, *J. Atmos. Ocean Tech., 12,* 468-478, 1995.

Rothacher, M. S. Schaer, L. Mervart, and G. Beutler, Determination of Antenna Phase Center Variations Using GPS Data, *1995 IGS Workshop, Potsdam, Germany, May 15-17,* 1995.

Saastamoinen, J., Atmospheric correction for the troposphere and stratosphere in radio ranging of satellites, in *The Use of Artificial Satellites for Geodesy, Geophys. Monogr. Ser., vol. 15,* edited by S. W. Henriksen, A. Mancini, and B. H. Chovitz, 247-251, AGU, Washington D. C., 1972.

Smith, E. K., and S. Weintraub, The Constants in the Equation for Atmospheric Refractiove Index at Radio Frequencies, *Proc. IEEE,* 41, 1035-1037, 1953.

Smith, T. L., S. G. Benjamin, B. E. Schwartz, S. I. Gutman, Using GPS-IPW in a 4-D data assimilation system, *Earth Planets and Space, 52,* 921-926, 2000.

Thayer, D., An Improved Equation for the Radio Refractive Index of Air, *Radio Sci., 9,* 803-807, 1974.

Tralli, D. M., and S. M. Lichten, Stochastic estimation of tropospheric path delays in Global Positioning System geodetic measurements, *Bull. Geod., 64,* 127-159, 1992.

Trenbreth, K. E. and J. G. Olsen, An evaluation and intercomparison of global analyses from the National Meteorological Center and the European Centre for Medium Range Weather Forecasts, *Bull. Am. Met. Soc, 69,* 1047-1057, 1988.

Trenbreth, K. E. and C.J. Guillemot, Evaluation of the global atmospheric moisture budget as

seen from analyses, *J. Climate, 8*, 2255-2272, 1995.

Ware, R. H., et al, Real-time national GPS networks for atmospheric sensing, *J. Atmos. Solar-Terrest. Phys., 63(12)*, 1315-1330,, 2001.

Zou, X, Y. Kuo, and Y. Guo, Assimilation of Atmospheric Radio Refractivity Using a Nonhydrostatic Mesoscale Model, *Mon. Wea. Rev., January* 1995.

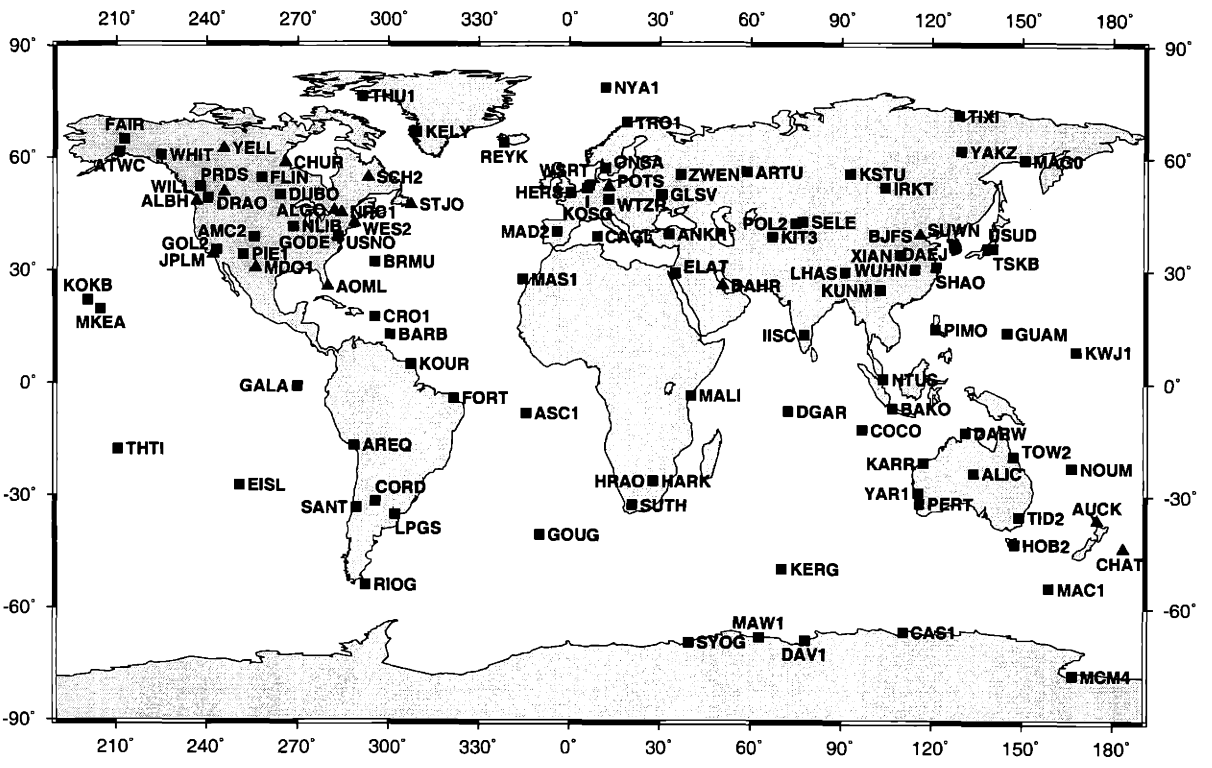

Figure 4.1. Locations of the IGS global GPS stations. Those stations with meteorological units are indicated with triangles, those without with squares.

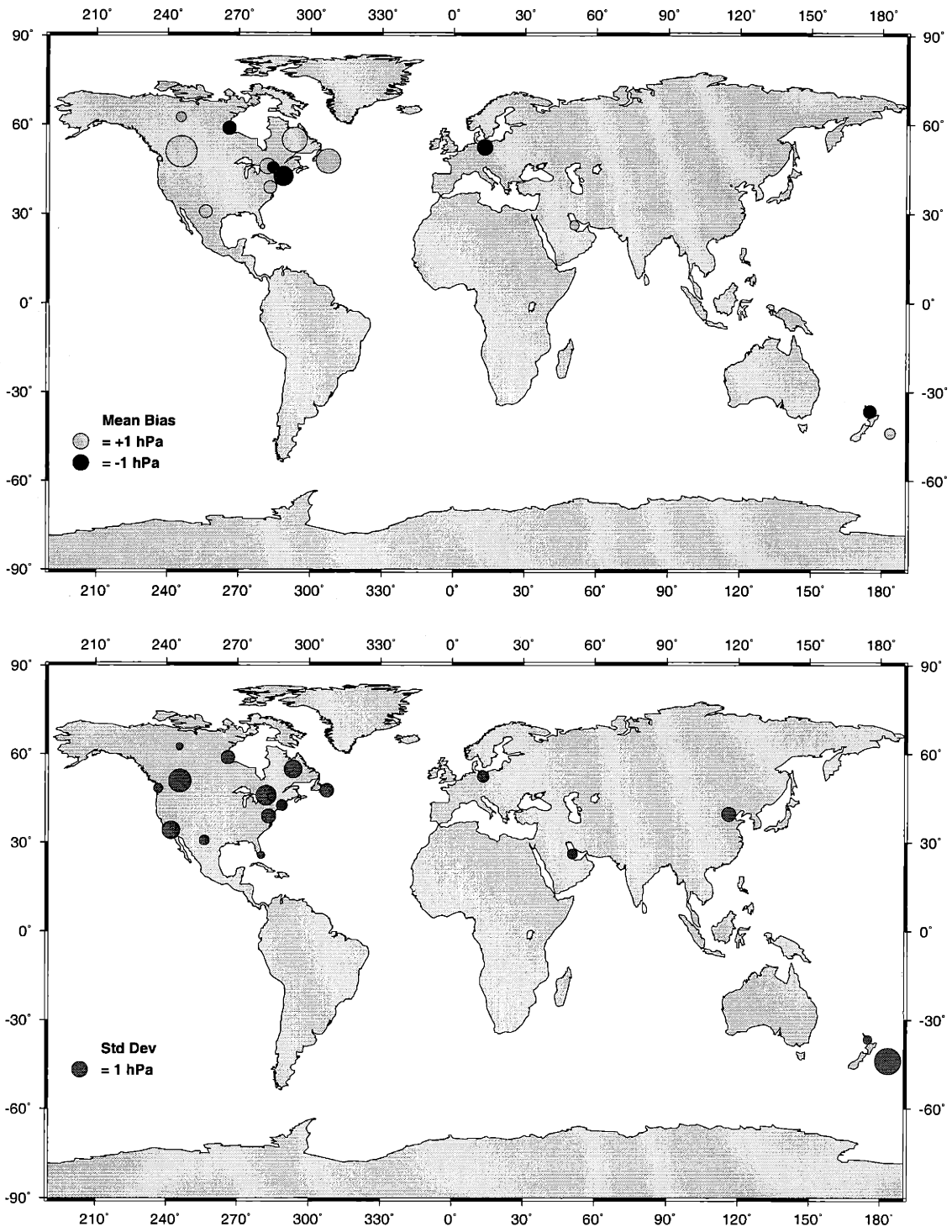

Figure 4.2. The upper plot shows the mean differences of the surface pressure comparisons between the in-situ meteorological units and the NCEP derived value. These averages are taken at individual stations over two years of data in 1999 and 2000. The lower plot shows the standard deviations of these differences.

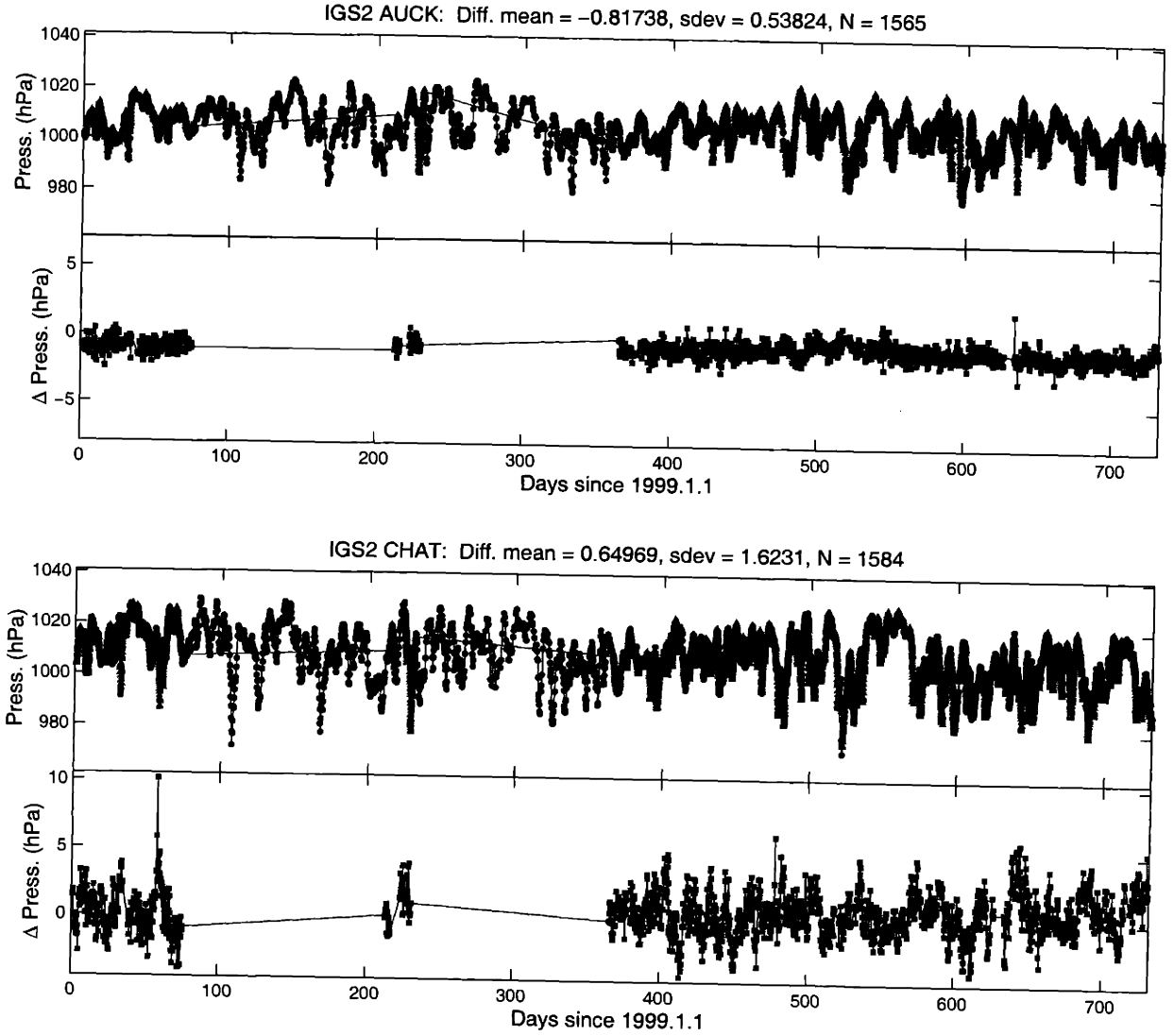

Figure 4.3. Station time series of surface pressure for 1999 and 2000. The upper plots show the undifferenced values, the triangles are the one hourly MET values and the circles are the six hourly NCEP values. The lower plots show the difference between the NCEP and MET values (NCEP - MET). Stations shown are AUCK and CHAT.

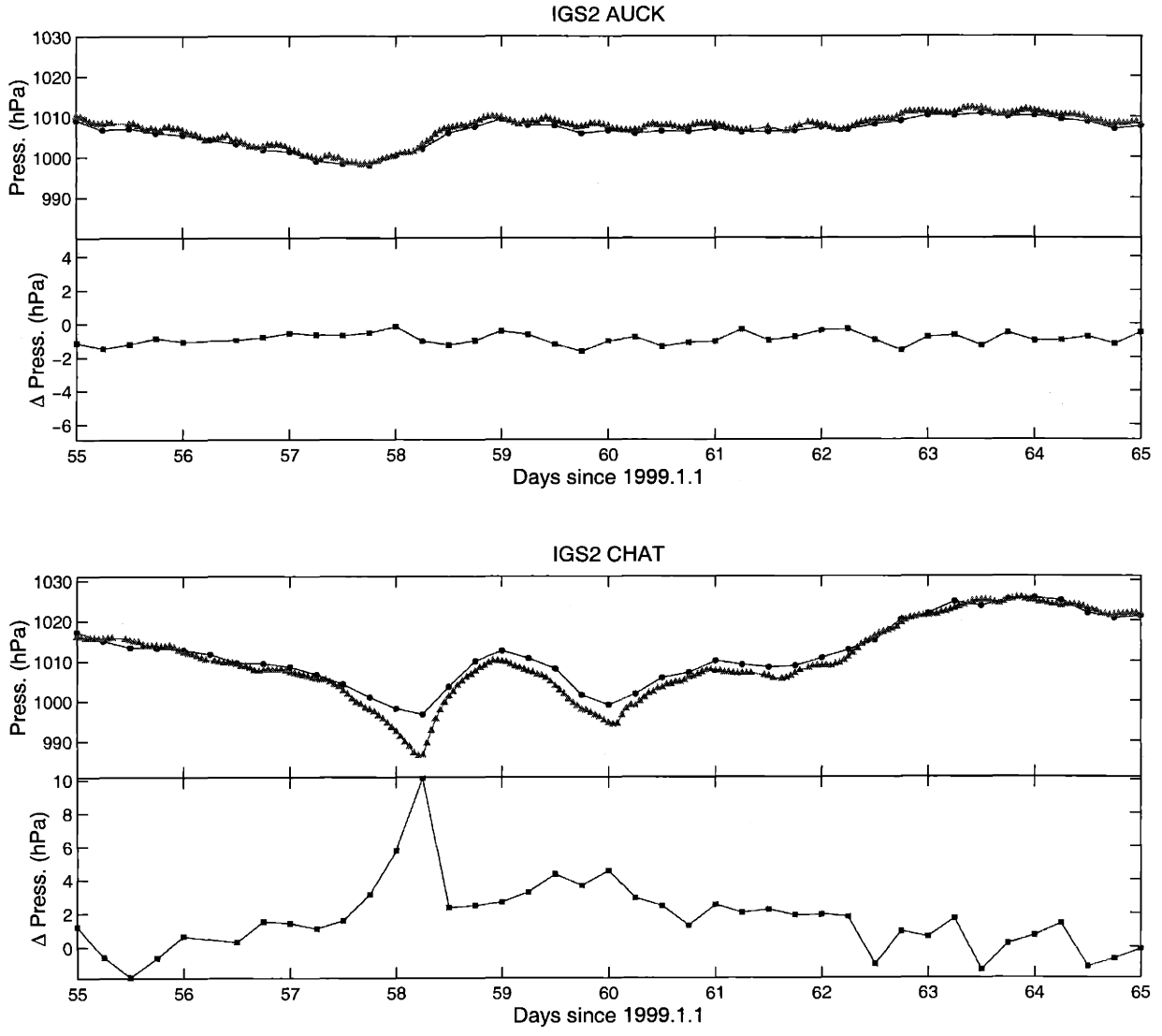

Figure 4.4. Station time series of surface pressure over ten days in 1999. The upper plot shows the undifferenced values, the triangles are the one hourly MET values and the circles are the six hourly NCEP values. The lower plot shows the difference between the NCEP and MET values (NCEP - MET). , Stations shown are AUCK and CHAT, this is a subset of the data shown in Figure 4.3.

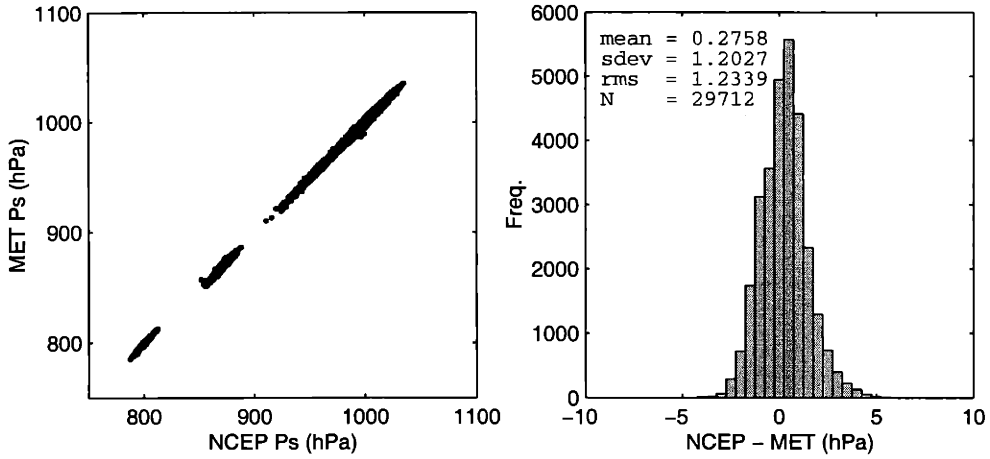

Figure 4.5. Scatter plot of surface pressure differences between NCEP and MET values, using data from all stations, and corresponding histogram (0.5 hPa bins).

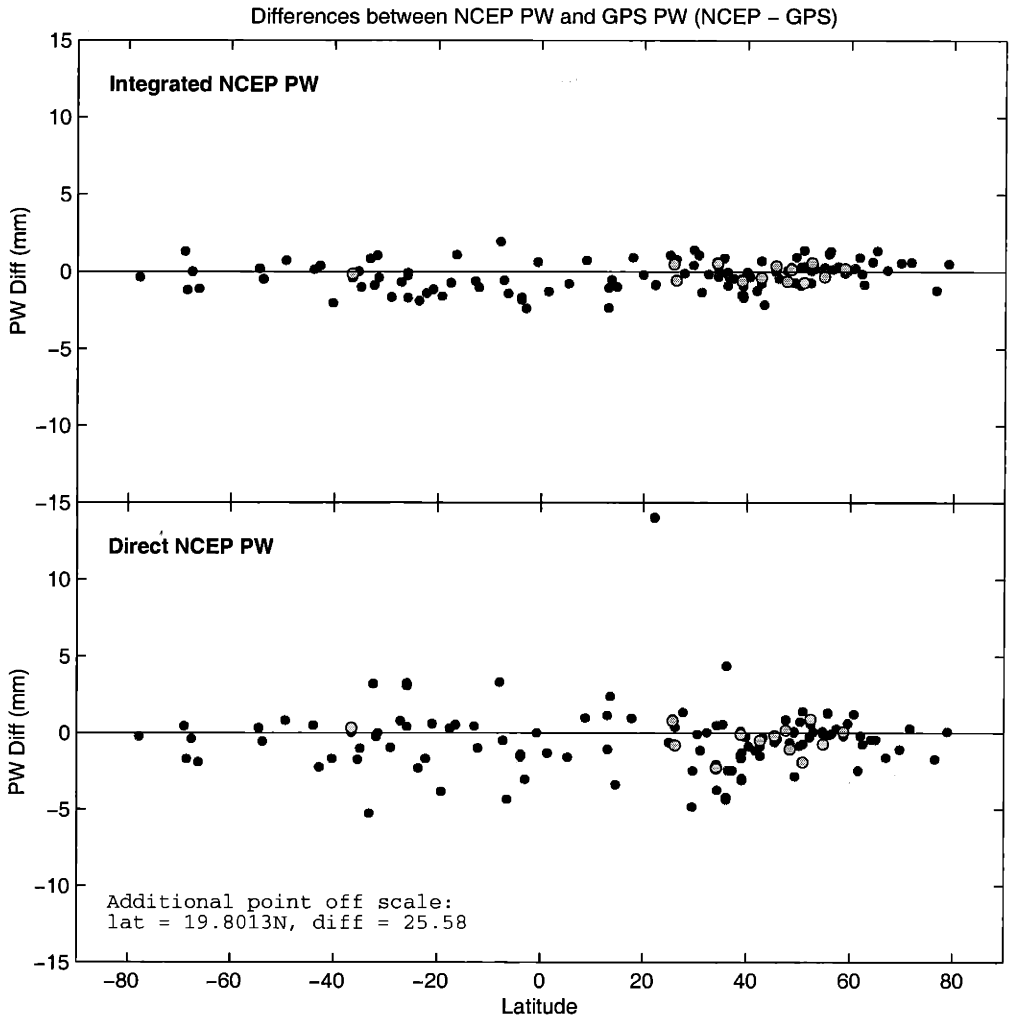

Figure 4.6. Mean differences between NCEP precipitable water vapor and GPS precipitable water vapor for individual stations, with respect to station latitude and averaged of the two years of data. The upper plot is the integrated NCEP PW comparison and the lower plot is the direct NCEP PW comparison. Open circles are those data points calculated using MET surface pressure, solid circles are those calculated using NCEP surface pressure.

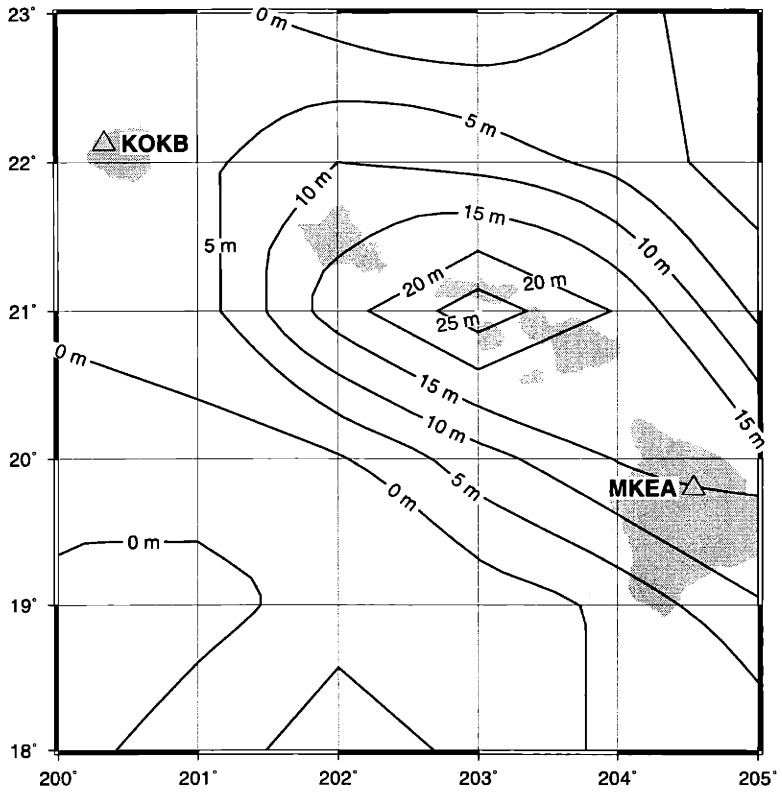

Figure 4.7. Map of Hawaiian islands, GPS stations KOKB and MKEA are indicated. The contours are for the internal topography field used by the NCEP global analyses for modeling surface variables.

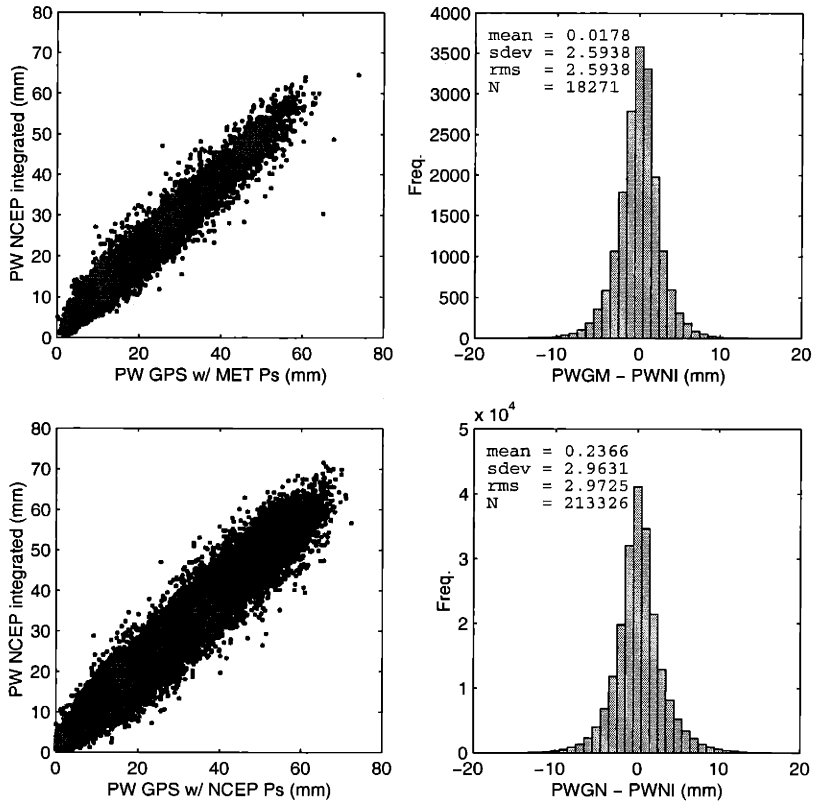

Figure 4.8. Scatter plots of precipitable water vapor differences, comparison between different methods. PWGN is GPS PW calculated using NCEP surface pressure, PWGM is GPS PW calculated using MET surface pressure, and PWNI is the NCEP integrated PW.

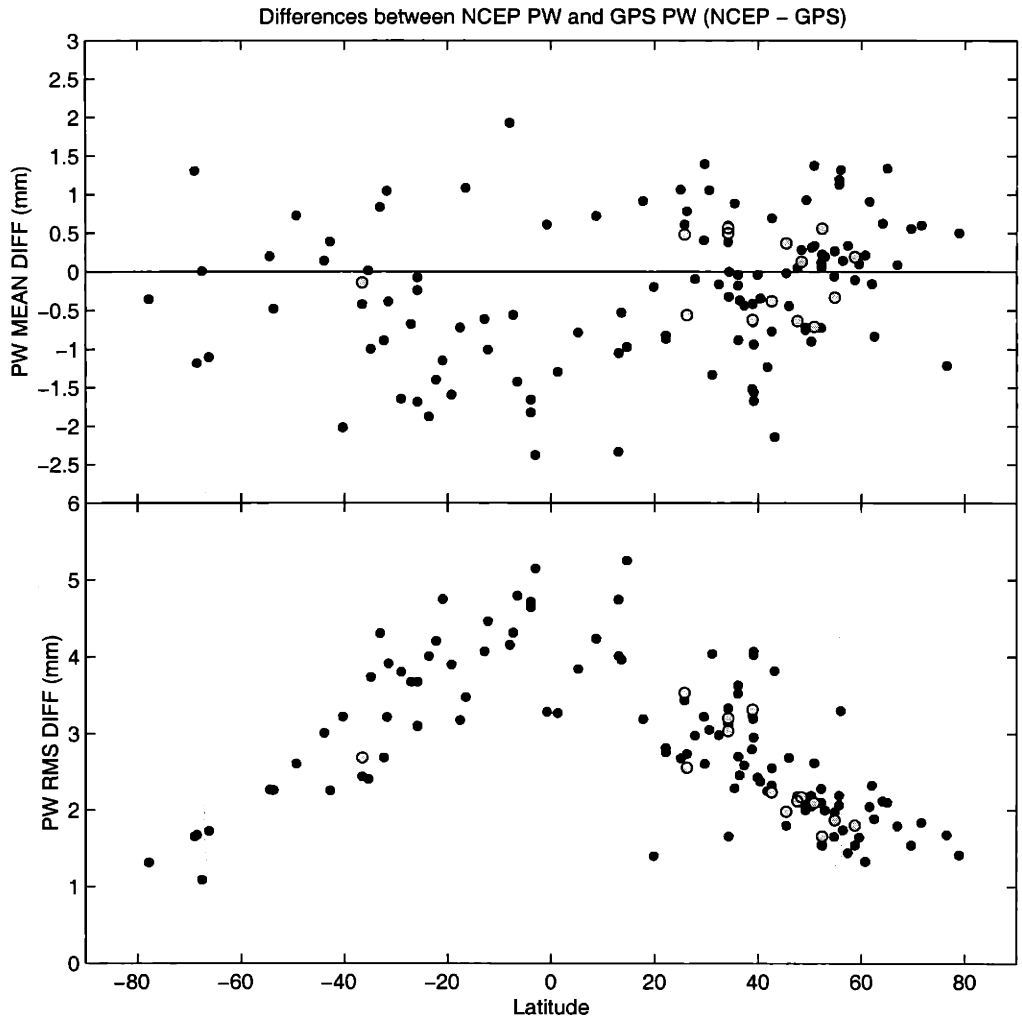

Figure 4.9. Comparison between NCEP precipitable water vapor and GPS precipitable water vapor for individual stations, with respect to station latitude and averaged of the two years of data. The upper plot shows the mean differences (NCEP - GPS) and the lower plot shows the rms differences. Open circles are those data points calculated using MET surface pressure, solid circles are those calculated using NCEP surface pressure.

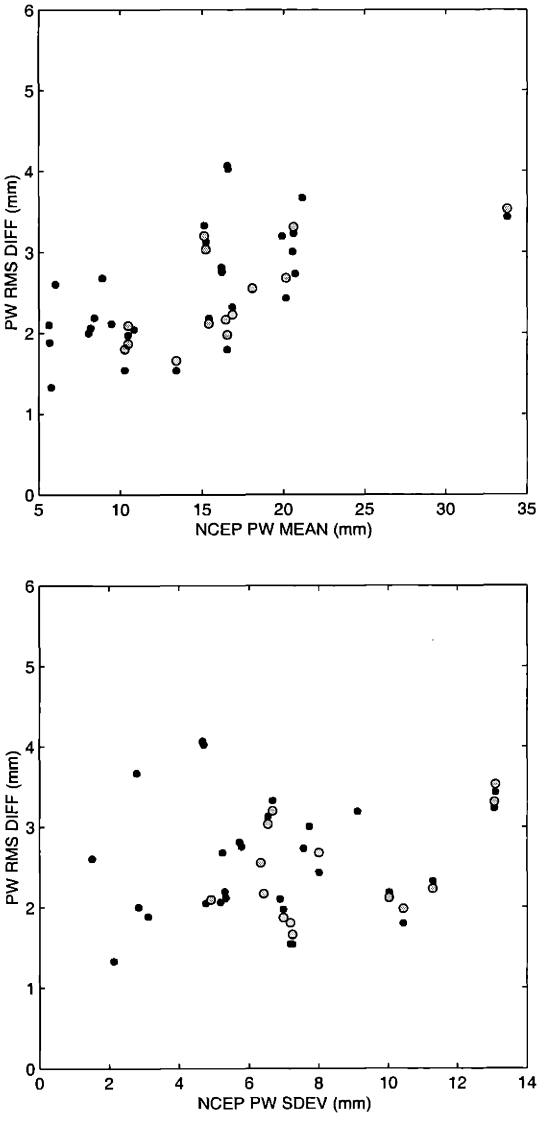

Figure 4.10. RMS differences between NCEP PW and GPS PW for individual stations, with respect to mean NCEP PW (upper plot) and standard deviation of NCEP PW (lower plot). Open circles are those data points calculated using MET surface pressure, solid circles are those calculated using NCEP surface pressure. All data averaged over two years.

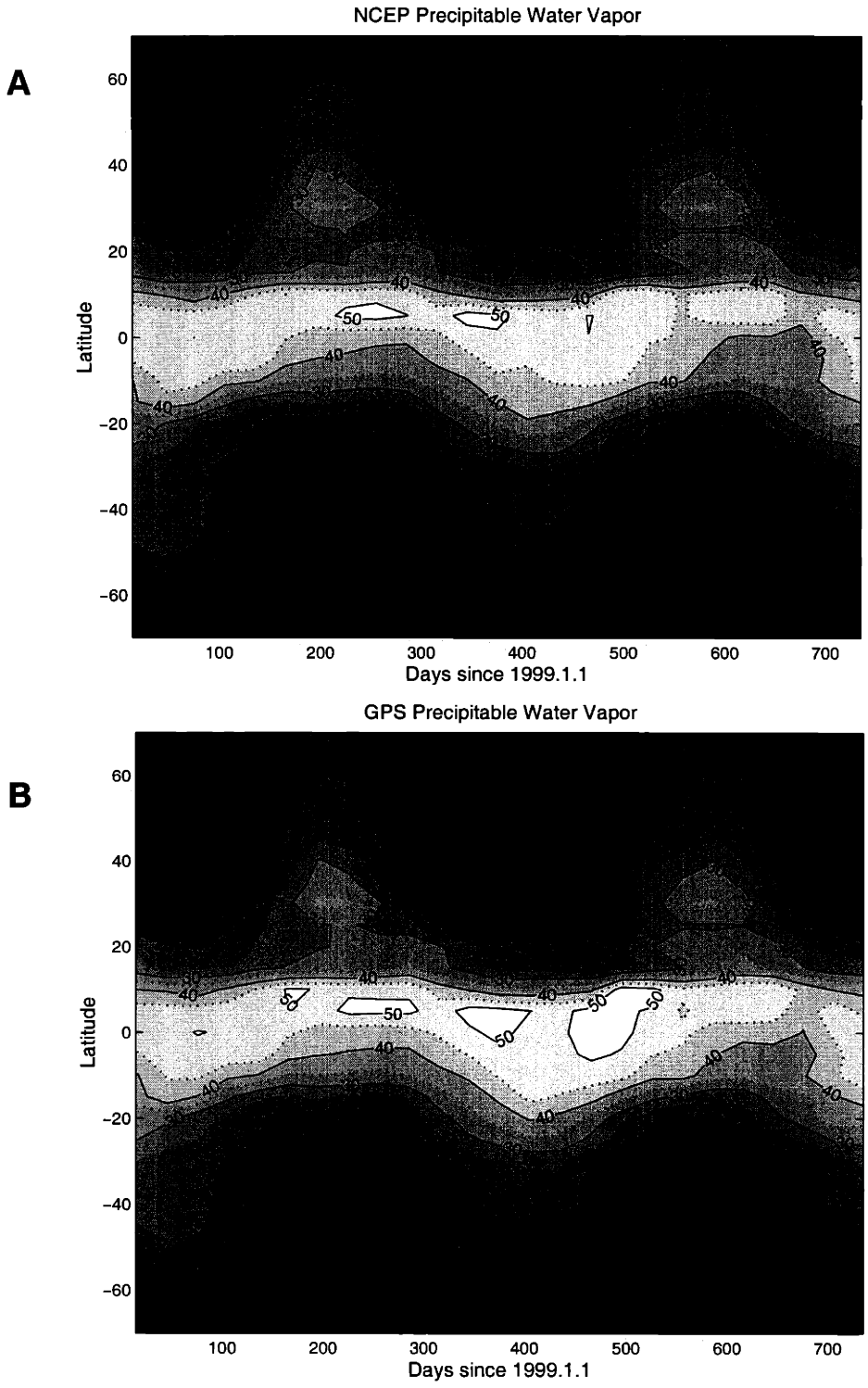

Figure 4.11. Zonal averages of precipitable water vapor estimated at IGS GPS stations. Averages are calculated in 15 moving average latitude bands over 30 day intervals (a) NCEP integrated PW values, (b) GPS PW estimates.

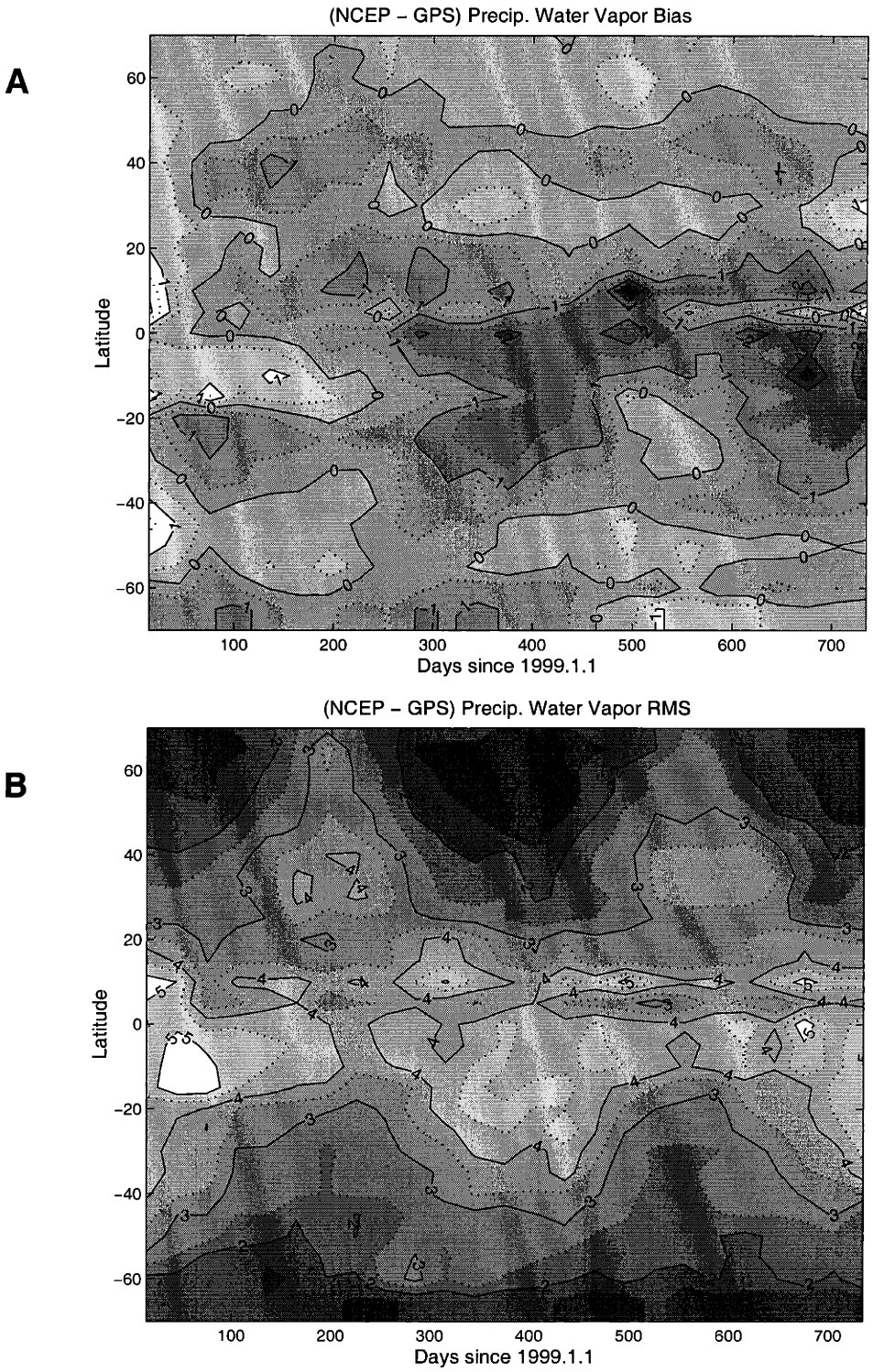

Figure 4.12. Zonal averages of PW comparisons. (a) Mean bias between NCEP integrated PW values and the GPS PW estimates (NCEP - GPS). (b) RMS differences between NCEP PW and GPS PW.

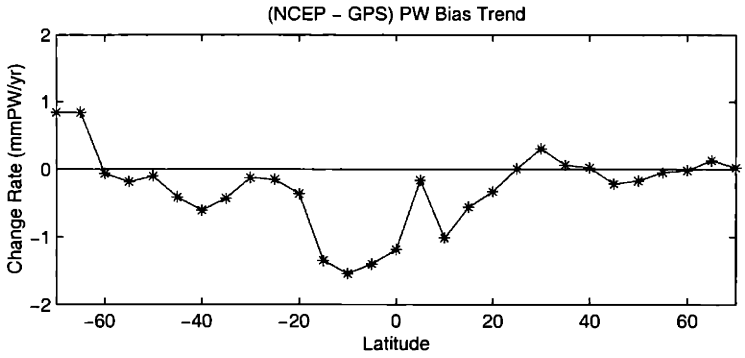

Figure 4.13. Linear trends in the zonal mean differences between NCEP PW and GPS PW (NCEP - GPS). Data is from the same results shown in Figure 4.12.

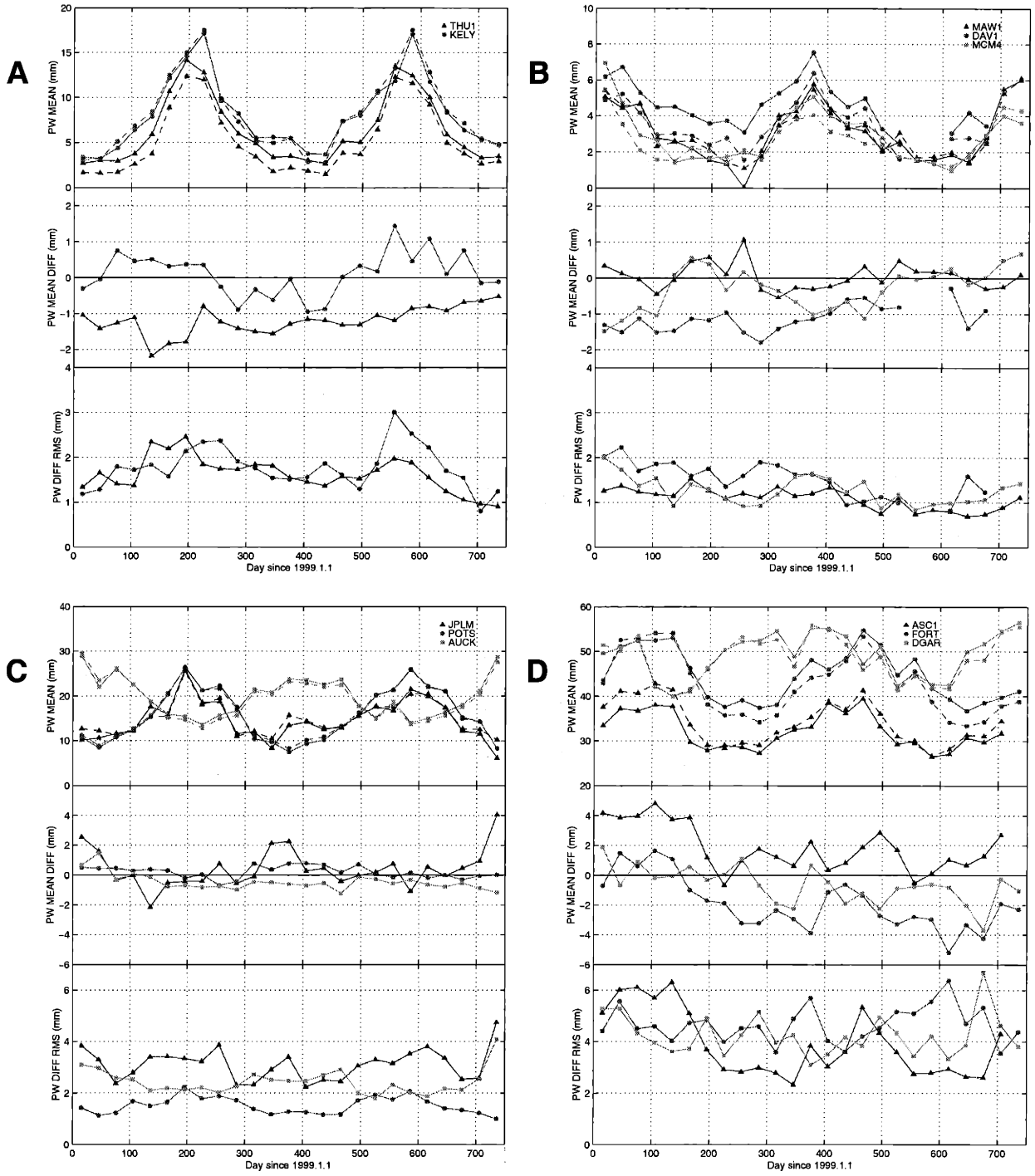

Figure 4.14. Comparison between NCEP and GPS PW, averaged over 30 day intervals. The top panels in each figure are absolute values of PW, solid line is GPS PW, dashed line is NCEP PW. The middle panels show the mean differences, (NCEP - GPS). The bottom panels show the rms differences. (a) Greenland stations, (b) Antarctia stations, (c) examples of mid-latitude stations, (d) examples of tropical stations.

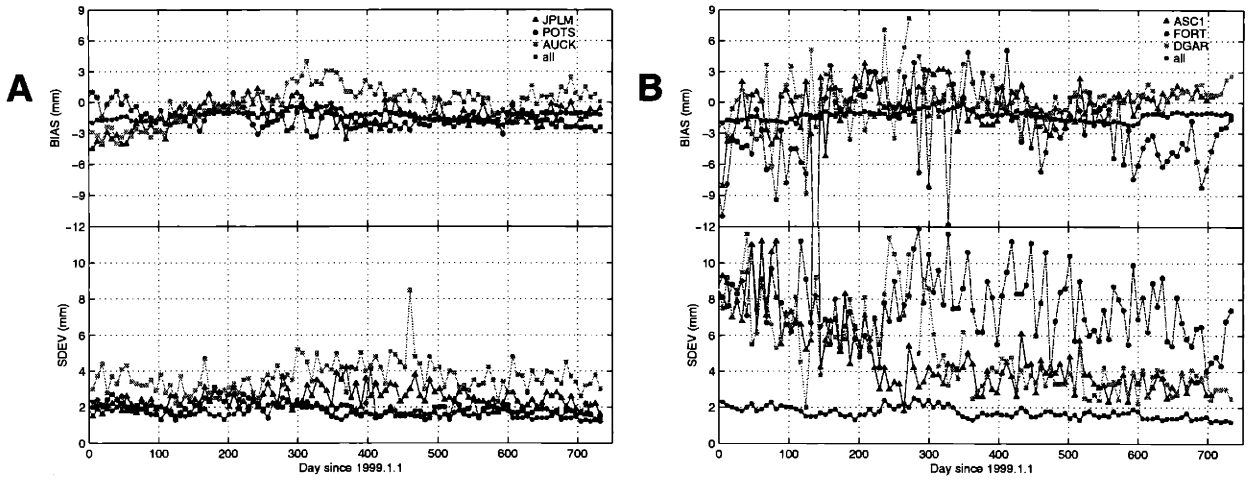

Figure 4.15. Comparison between the IGS combination zenith delay and the Scripps zenith delay, weekly averages. Top panel is mean bias (SOPAC - IGS), bottom panel is standard deviation. (a) Mid-latitude stations, (b) tropical stations.

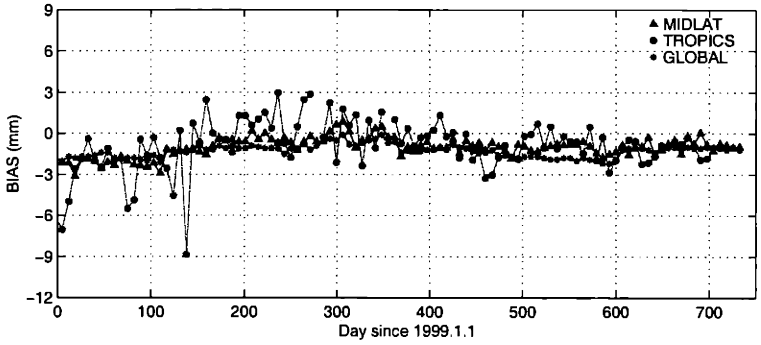

Figure 4.16. Comparison between the IGS combination zenith delay and the Scripps zenith delay, weekly averages. Top panel is mean bias (IGS - SOPAC), bottom panel is standard deviation. (a) Average of three mid-latitude stations (JPLM, POTS, AUCK), (b) average of three tropical stations (ASC1, FORT, DGAR).

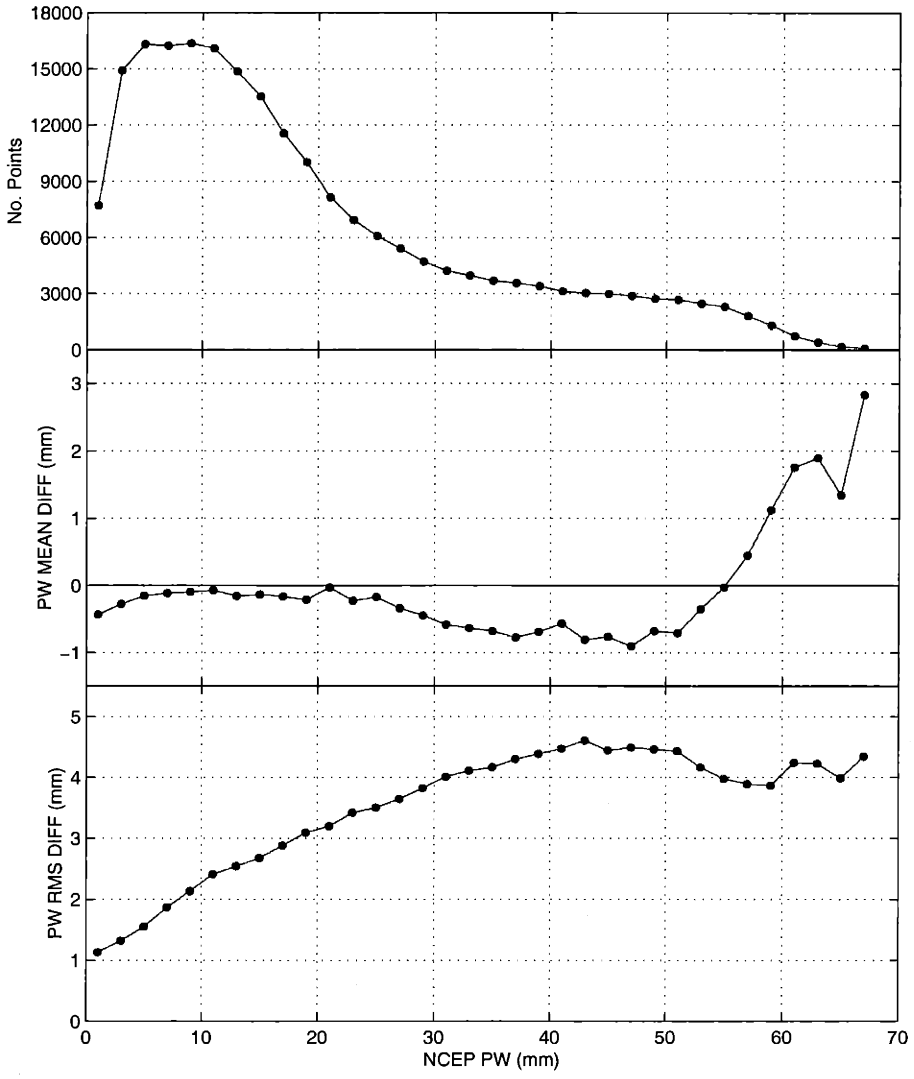

Figure 4.17. Comparison between the NCEP and GPS PW estimates, averaged over 2 mm PW bins of absolute precipitable water vapor . The top panel shows the number of data points used in each bin (minimum of 50), the middle panel shows the mean PW differences (NCEP - GPS), and the bottom panel shows the rms differences.

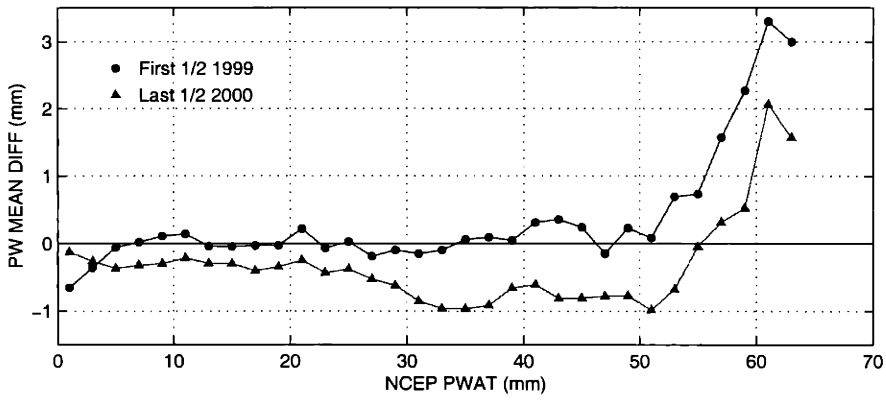

Figure 4.18. Mean bias between the NCEP and GPS PW estimates, averaged over 2 mm PW bins of absolute precipitable water vapor. Two subsets of the data are shown, the first half of 1999 and the second half of 2000.

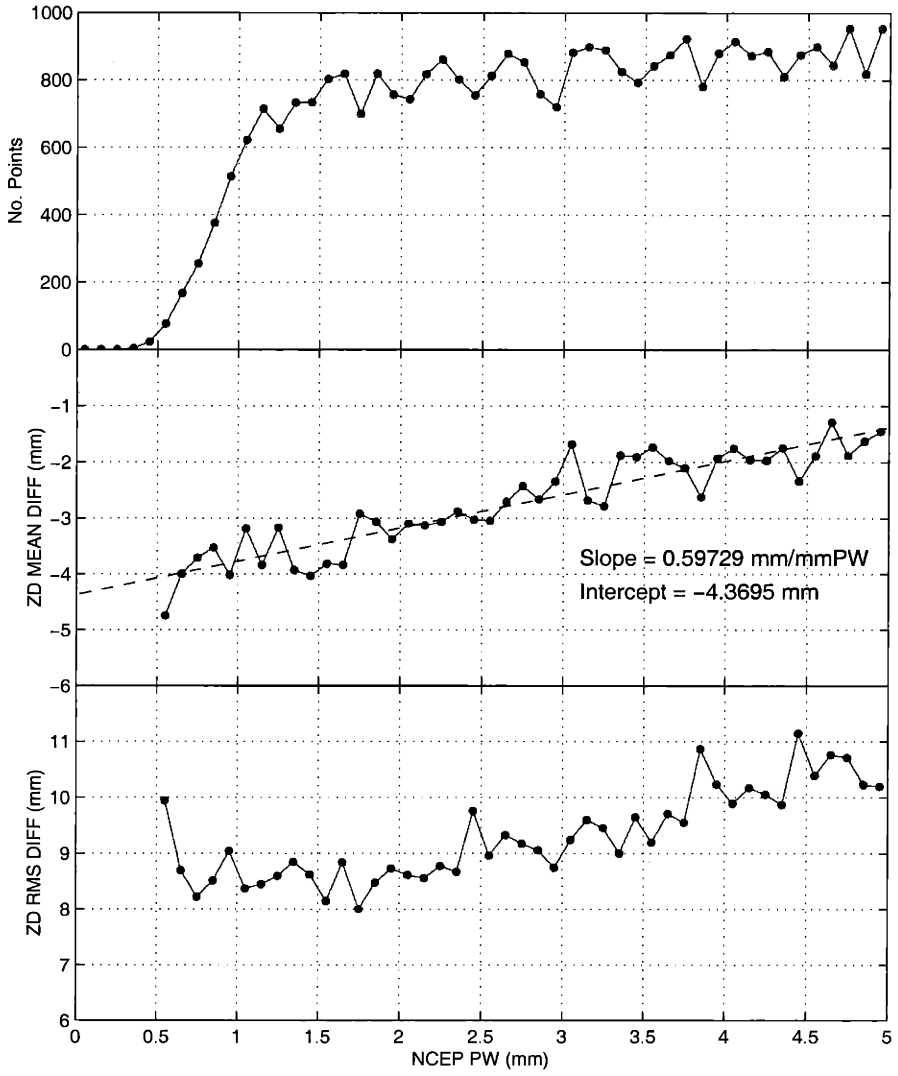

Figure 4.19. Comparison between the NCEP and GPS zenith delay estimates, averaged over 0.1 mm PW bins of absolute precipitable water vapor. The top panel shows the number of data points used in each bin (minimum of 50), the middle panel shows the mean zenith delay differences (NCEP - GPS), and the bottom panel shows the rms differences.

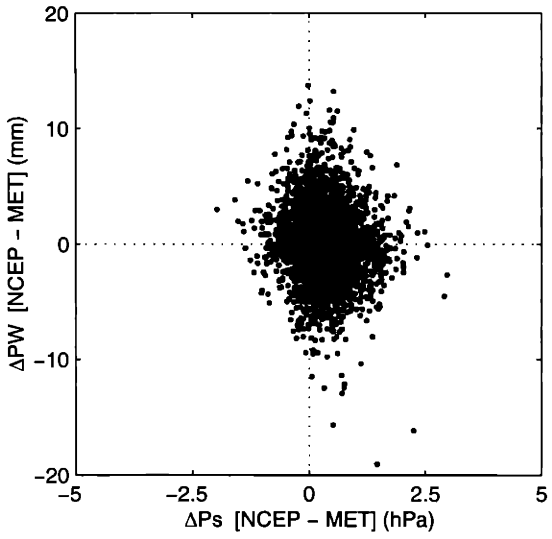

Figure 4.20. Scatter plot of surface pressure errors to precipitable water vapor errors. The NCEP surface pressure is the integrated value, the MET surface pressure is the in-situ measurement. The NCEP PW is the integrated value, the MET PW is that value calculated using GPS delay and in-situ surface pressure.

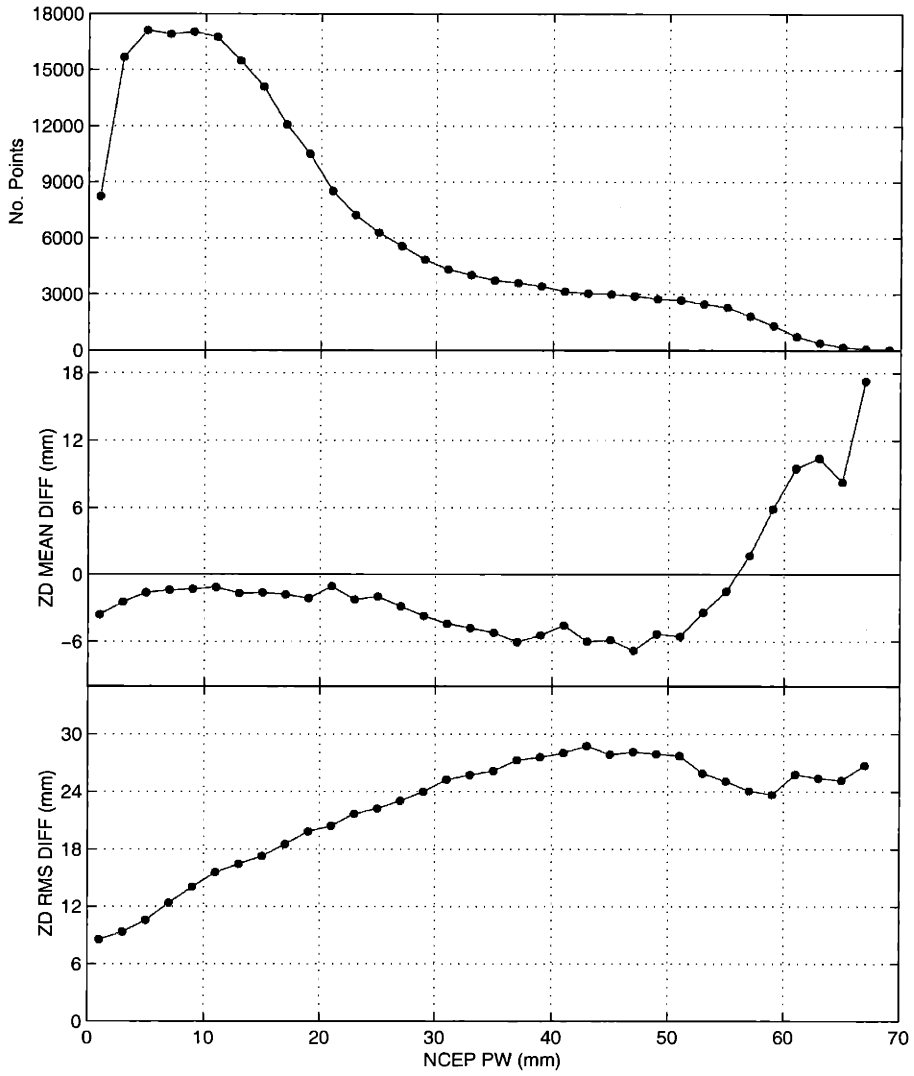

Figure 4.21. Comparison between the NCEP and GPS zenith delay estimates, averaged over 5 mm PW bins of absolute precipitable water vapor. The top panel shows the number of data points used in each bin (minimum of 50), the middle panel shows the mean zenith delay differences (NCEP - GPS), and the bottom panel shows the rms differences.

Chapter 5

Conclusions

We have successfully formulated algorithms for calculating atmospheric delay values at optical wavelengths. The major difference in these algorithms to previous radar based delay algorithms is the more precise integrated surface pressure calculation. We have also updated the optical refractivity formulas to better model satellite based delays, current formulas are optimised for ground based applications.

Our atmospheric delay model has been validated using Automatic Weather Stations (AWS) in the polar regions and GPS data over the globe. The GPS data validation was also augmented by in-situ meteorology measurements at some of the stations. The GPS validation process allowed us to investigate the estimation of precipitable water vapor using GPS data. Based on the accuracy estimates of our surface pressure model, we were able to greatly expand the amount of precipitable water vapor data we could estimate. The error in our precipitable water vapor estimates is less than 1.6 mmPW.

A summary of the delay errors is given in Table 5.1. Overall, we are within the ICESat error budget. The magnitudes of the total error components clearly show that errors in surface pressure estimates are the biggest source of error. Validation studies should therefore focus on surface pressure. Based on the validation studies performed thus far, there does not appear to be any spatial or temporal biases in the atmospheric delay error estimates. Seasonal and interannual variations in the errors have been characterized, they tend to be directly related to the amount of synoptic scale pressure activity for hydrostatic delay, and directly related to absolute precipitable water vapor values for the non-hydrostatic component of delay. The validation studies described in this dissertation will be continued over the lifetime of the ICESat mission, enabling us to separate out delay error variations from real surface elevation change signals.

Table 5.1: Summary of atmospheric delay errors

Error Source	Contribution
Refractivity model	0.2 mm
Mapping function (for pointing angles < 10^o)	0.5 mm
NCEP direct PW field (vs. integrated value)	0.1 mm
Spatial interpolation	2 mm
Temporal interpolation	0.3 mm
Surface Pressure: Polar regions (from AWS)	< 12 mm
Surface Pressure: Global (from in-situ met units at GPS stations)	5 mm
Precipitable water vapor: Polar (from GPS Met)	0.24 mm
Precipitable water vapor: Global (from GPS Met)	0.4 mm
RSS total (polar)	**12.2 mm**
RSS total (global)	**5.4 mm**
Total ICESat atmospheric delay error budget	**20 mm**